

STAVEBNÍ OBZOR

číslo 1/2020



Obsah:

1	EFFECT OF KAOLIN ADDITION INTO METAKAOLIN GEOPOLYMER COMPOSITE <i>Alexey Manaenkov, Michaela Steinerová, Ekaterina Kukleva and Jiří Litoš</i>
2	FLEXURAL PERFORMANCE OF COLD-FORMED THIN-WALLED STEEL-PAPER STRAW BOARD COMPOSITE SLAB <i>Xiuhua Zhang, Zilin Zhao, Xiang Li</i>
3	METHODOLOGY FOR CITY LEVEL URBAN ROAD NETWORK CONNECTIVITY ANALYSIS USING GEOGRAPHICAL INFORMATION SYSTEMS (GIS) <i>Kurre Sai Sahitya*, CSRK Prasad</i>
4	FIELD TEST ON THE COOPERATION OF NSM STRENGTHENING AND EXTERNAL TENDON RETROFITTING TECHNIQUE <i>Jianxi Yang, Jiaping Yu, Quansheng Sun, Hongshuai Gao and Jiawei Wang</i>
5	SELF FIBER COMPACTING CONCRETE (SFCC) PROPERTIES INCORPORATED WITH SILICA FUME AND FIBER <i>Hakas Prayuda, Fanny Monika, Martyana Dwi Cahyati and Fadillawaty Saleh</i>
6	ANALYTICAL SOLUTION AND FIELD TEST OF CRITICAL BEARING CAPACITY AND SETTLEMENT OF PILE TIP <i>Suchun Yang*, Junwei Liu, Mingyi Zhang, Yonghong Wang</i>
7	A NEW BLAST-RESISTANT DESIGN METHOD OF RC MEMBERS AND ITS APPLICATION IN PERFORMANCE BASED BLAST-RESISTANT DESIGN PROCEDURE <i>Runqing Yu, Diandian Zhang, Yujun Cang, Sen Li</i>
8	REMEDICATION TECHNOLOGY OF CLOCHE REPLACEMENT FOR WW2 FORTIFICATION IN THE CZECH REPUBLIC <i>Jiří Pazderka, Michal Ženišek, Tereza Pavlů, Pavel Reiterman, Ondřej Holpaček</i>
9	STUDY ON THE PERFORMANCE OF HIGH-MODULUS ASPHALT CONCRETE PAVEMENT IN EXTREME CURVES OR STEEP SLOPES OF TRUNK HIGHWAY <i>Honglei Zhang, Mingrui Yang, Youcheng Ma</i>
10	ANALYSIS ON CONSTRUCTION DEFORMATION AND SUPPORTING STRUCTURE OF TWO-STEP AND THREE-SECTION EXCAVATION METHOD FOR SUPER LARGER SPAN HIGHWAY TUNNEL <i>Fujin Hou, Yanbin Luo, Qing Jiang, Jianxun Chen, Tao Li, Fangfang Dong</i>
11	CHARACTERISATION OF THERMAL-LOADED CEMENT-BASED COMPOSITES BY COMBINED TIME-LAPSE TOMOGRAPHY AND THE FOUR-POINT BENDING TEST <i>Ivana Kumpová, Tomáš Fíla, Petr Koudelka, Iva Rozsypalová, Zbyněk Keršner, Daniel Kytýř, Michal Vopálenský, Daniel Vavřík</i>

EFFECT OF KAOLIN ADDITION INTO METAKAOLIN GEOPOLYMER COMPOSITE

Alexey Manaenkov¹, Michaela Steinerová², Ekaterina Kukleva³ and Jiří Litoš¹

1. *Czech Technical University, Faculty of Civil Engineering, Experimental Centre, Thákurova 2636/7a, Prague, Czech Republic; alexey.manaenkov@fsv.cvut.cz; litos@fsv.cvut.cz*
2. *Czech Academy of Sciences, Laboratory of Rock Structure and Mechanics, V Holešovičkách 94/41, Prague, Czech Republic; steinerova1@gmail.com*
3. *Czech Technical University, Faculty of Nuclear Sciences and Physical Engineering, Department of Nuclear Chemistry, Břehová 7, Prague, Czech Republic; ekaterina.kukleva@fjfi.cvut.cz*

ABSTRACT

Industrially produced metakaolin may contain raw kaolin residues. Therefore, the aim of this work was to determine the impact of kaolin remains on the metakaolin and the final geopolymer quality. A series of mixtures based on metakaolin (Mefisto L05 by CLUZ Nove Straseci, Czech Republic) was prepared with the 0-60 wt% gradual addition of raw kaolin, and the mechanical strength of the final geopolymer products was tested. It was found that up to a 20 wt. % amount of kaolin in metakaolin does not weaken the geopolymer's performance. Moreover, a geopolymer made of metakaolin with 2-4 wt% of kaolin showed slightly better mechanical properties than the geopolymers made from metakaolin itself.

KEYWORDS

Geopolymer, Metakaolin, Kaolin, Mechanical properties, Frost resistance

INTRODUCTION

The number of geopolymer applications increases every day [1-7]. However, there is still a significant number of its properties and details that have to be studied. The influence of basic constituents' composition on geopolymer strength, such as a variety slag-metakaolin ratio [8] or Si/Al metakaolin (MK) ratio [9,10], is being studied. Even so, raw kaolin burning in industrial quantities can lead to the imperfect dehydration of kaolinite. So, the influence of kaolin remains in metakaolin (Mefisto L05, CLUZ Nove Straseci, Czech Republic) was studied in this paper.

Earlier as a main aluminosilicate source metakaolin and fly ash were taken [11], but nowadays the list of geopolymer precursors is significantly increased especially with by-product materials like slag and silica fume [12]. Metakaolin is produced from kaolin, kaolinitic clay or claystone by continual burning. The quality of the burned product depends on the burned amount, particle size, thickness of the layer, and temperature. Therefore, the conversion of kaolinite to metakaolin could not be absolute, which affects further geopolymerization, such as other impurities [13, 14].

In this article the influence of raw kaolin residua (0-60 wt%) in thermally activated kaolin was studied. A test series of compressive and flexural strength was conducted on samples with a variety

of raw kaolin additions. Also, the mechanical properties of the geopolymers with and without the raw kaolin addition were further characterized by frost resistance.

METHODS

Materials

Mefisto L05, made by the Czech company CLUZ Nove Straseci (Czech Republic) was used with a declared metakaolin content of 95 wt% and impurities such as quartz and muscovite. To remove the residual kaolin in Mefisto L05, the powder was burned at 750 °C for 6 hours. The raw kaolin used was produced by Sedlec Ia (Czech Republic). The alkaline activator was prepared by dissolving NaOH (Lachner, Czech Republic) in sodium water glass from Vodni Sklo, a.s. (Czech Republic) in a volume mass ratio of 1 to 0.15, respectively. As an aggregate, silica sand Strelec ST 92 with 99 wt% of SiO₂ and a particle size of D₅₀ = 0.6 mm was used.

Sample preparation

Metakaolin and an alkaline activator were mixed (Si/Al = 1.8; Na/Al = 1.0; Na/H₂O = 0.7) first for 5 minutes, and a basic geopolymer matrix was obtained. Final mass of alkaline activator depended on the metakaolin or metakaolin+kaolin amount. Then, kaolin and sand were added and stirred for 10 minutes. Sand formed 60 % of the total mixture weight.

To ensure the homogenous distribution of a small amount of kaolin in the samples (5 wt% and lower) the appropriate amount of kaolin was dispersed in approximately 30 g of water, which was required for proper dilution of the alkaline activator. Then, the suspension was added into the already mixed geopolymer matrix. For samples with a kaolin content above 5 wt%, kaolin in the form of a fine, dry powder was added with sand into a geopolymer matrix that helped activate the precursor mixture mechanically.

The weight percentage of kaolin and metakaolin in the samples was 0 to 50 and 100 to 50, respectively. This form of writing was chosen to imitate the impurities percentage in the initial powder.

The mixture was then poured into 40 mm x 40 mm x 160 mm plastic molds under vibration until air bubbles disappeared. The samples were stored indoors in covered molds for 7 days until completely hardened. Then, the samples wrapped in polyethylene foil were cured at laboratory temperature for 28 days to comply with the solidification conditions. All samples were prepared under the same conditions at 20 °C and humidity 45 % and stored for two months after curing before testing.

For XRD and FTIR analyses dry mixtures of metakaolin (MK) and kaolin (K) were prepared in ratio MK:K = 95:5, 85:15 and 65:35.

Sample characterization

Compressive strength and three-point flexural strength tests were performed on a semi-automated press EU 40 Werkstoffprufmaschinen, Leipzig according to Standard No. ČSN EN 1015-11(1999) [15] using the standard sample size, i.e., 40 mm x 40 mm x 160 mm.

Frost resistance tests were carried out according to the frost resistance standard CSN 731322 (1969) [16] by alternating freezing and defrosting of water-saturated samples within 50 cycles. Each cycle consisted of 4 hours of freezing at -20 °C and 2 hours of defrosting in water at 20 °C. Before the strength measurements were conducted, all samples were dried at laboratory temperature for 28 days.

X-ray diffractograms were recorded using Rigaku MiniFlex 600 (Ni-filtered, Cu-K α 1,2 radiation) equipped with a NaI(:TI) scintillation detector and were compared to the relevant records in the ICDD PDF-2 database [17].

Fourier-transformed infrared spectra (FTIR) were recorded by a Nicolet iS50 FTIR spectrometer [18] in the middle infrared region at 400 – 4000 cm⁻¹, with a resolution of 2 cm⁻¹ on an ATR diamond crystal, which data were also compared to the relevant records in the HR Inorganics – Minerals database.

Study of the measured samples was carried out on a Quanta 450 (FEI) Scanning Electron Microscope (SEM). The observations of the polished cross-sections were performed in backscattered electron (BSE) mode under a high vacuum. The analytical conditions were the energy of the electron beam at 30 kV and a spot size of 2 mm at a 10 mm working distance. The samples were vacuum-coated with gold to prevent localized charging in the specimen. The semi-quantitative chemical composition of the matrix was analyzed using an energy-dispersive X-ray microanalyzer (EDAX, Apollo X).

A detailed SEM was performed on a Phenom XL Desktop SEM under high-vacuum on the natural sample surface of the polished sections mentioned above with a voltage of 10 kV (SEM) and 15 kV (SEM/EDS).

The elasticity modulus measurement was carried out with a nanoindentation tester by an NHTX S/N: 10-00039 (Anton Paar GmbH, Austria) according to Oliver-Pharr method [19]. The settings were the maximum load of 2 mN, the loading rate of 30 nm/min, and the Poisson's ratio of 0.2.

RESULTS

Influence of kaolin on mechanical properties of geopolymer

The compressive strength of the tested samples with changing kaolin content ranged from 20 to 55 MPa (Table 1). Samples with kaolin content in metakaolin up to 20 wt% showed slightly better compressive mechanical properties in comparison with samples made from pure metakaolin. Changes in flexural strength due to varying kaolin content were negligible and within statistical error, while kaolin content was lower than 20 wt% (Table1). The addition of kaolin above 20 wt% led to a dramatic decrease in both the compressive and flexural mechanical strengths. Hardening process time slowed down with the increasing addition of kaolin.

The addition of kaolin increased mixture viscosity and made mixing difficult, so the porosity of some samples could increase. This could influence the microstructure and thus decreased strength at higher kaolin concentrations.

Tab. 1 - The compressive and flexural strength values [MPa] of the samples with variable kaolin content.

Amount of added kaolin [wt%]	Compressive strength [MPa]	Flexural strength [MPa]
0	47.2 ± 2.2	8.0 ± 0.4
2	52.5 ± 2.5	7.9 ± 0.4
3	52.6 ± 2.5	8.1 ± 0.4
4	52.4 ± 2.5	8.1 ± 0.5
5	55.2 ± 2.6	8.2 ± 0.3
7	53.6 ± 2.5	8.4 ± 0.6
10	53.3 ± 2.5	8.2 ± 0.4
15	52.6 ± 2.5	8.5 ± 0.4
20	52.1 ± 2.4	8.1 ± 0.4
30	40.0 ± 1.9	7.5 ± 0.5
35	32.7 ± 1.5	4.5 ± 0.2
50	21.5 ± 1.0	4.0 ± 0.3

Frost resistance

The compressive and flexural strength after the freezing-defrosting cycles in water was compared with the values of the no-frost sample strength. Samples with 1 wt% of kaolin displayed cracks already after 25 freezing cycles. The cracks were probably caused by unsatisfactorily homogenized kaolin input and, therefore, were not measured. Figure 1 shows flexural and compressive strength after 50 cycles with the highest value reached by samples containing 2-3 wt% of kaolin. The compressive strength even surpassed the highest values before freezing. The reason could be in the prolonged dwell in the proper conditions which aided the polycondensation. Higher addition of kaolin deteriorated the frost resistance probably because of retaining water leading to expansion inside the kaolin particles.

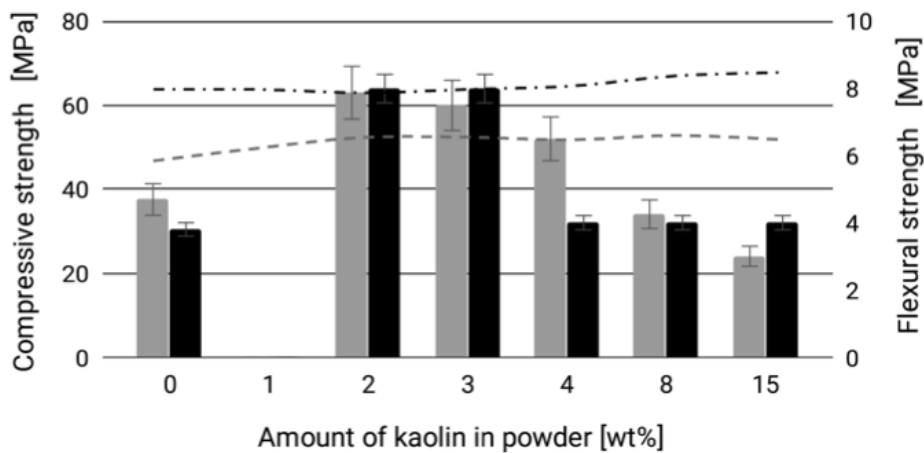


Fig. 1 - The compressive (gray slopes) and flexural (black slopes) strength values of samples affected by kaolin after 50 frost cycles. The gray dashed line shows the values of the no-frost samples' compressive strength, the black dash-dot line shows the flexural strength values of the no-frost samples.

XRD analysis

The amount of raw kaolinite in the industrial metakaolin Mefisto L05 was determined based on peak areas of kaolinite at 12.3° and 24.8° . According to five-point calibrations based on metakaolin, mixed metakaolin with kaolin and kaolin the amount of unburned kaolin in Mefisto L05 was determined to be $3.5 \pm 0.5 \%$. Kaolinite in Mefisto L05 is easily visible, and its diffractogram looks similar to the record of the sample with 5 % kaolin addition (MK:K=95:5) (Figure 2). Kaolinite was not found in the metakaolin sample burned in the laboratory kiln, or its amount was under the detection limit. As far as XRPD is a very sensitive method for crystal materials detection, it is possible to say that no kaolinite was presented in burned metakaolin. Quartz was found in all samples.

The presence of kaolinite after geopolymer hardening was observed in the samples with added kaolin (Figure 2, GP [MK:K=95:5]). It means that kaolinite does not participate in polycondensation. Based on the kaolinite calibrations, its amount in geopolymer was calculated to $5.1 \pm 1.0 \%$, which corresponds with the added amount of kaolin.

Besides quartz, muscovite was detected in the metakaolin Mefisto L05. The amorphous hump of metakaolin is shifted to higher angles and becomes narrower after polycondensation in the matrix, which can mean higher structural organization.

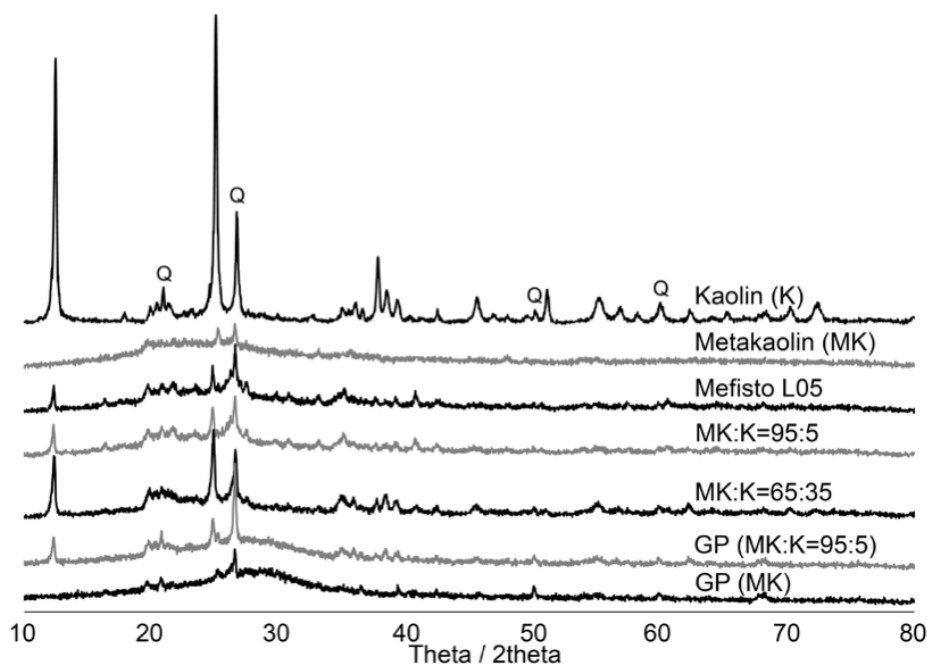


Fig. 2 - A comparison of XRD diffractograms of the metakaolin (MK), raw kaolin (K), and their mixtures (MK:K=95:5 and 65:35); industrial metakaolin Mefisto; the resulting geopolymer made of metakaolin (GP (MK)) and metakaolin with added kaolin (GP (MK:K=95:5)). Q = quartz.

FTIR analysis

The content of kaolinite in the industrial metakaolin Mefisto L05 was very low, and thus, a quantitative analysis based on FTIR spectra was not performed (Figure 3). However, the addition of raw kaolin to the reference-scale samples (MK:K=95:5 and 65:35) is demonstrated by the bands of proportionally graduating height and by the shape with shoulders' referring to the proper kaolin ratio.

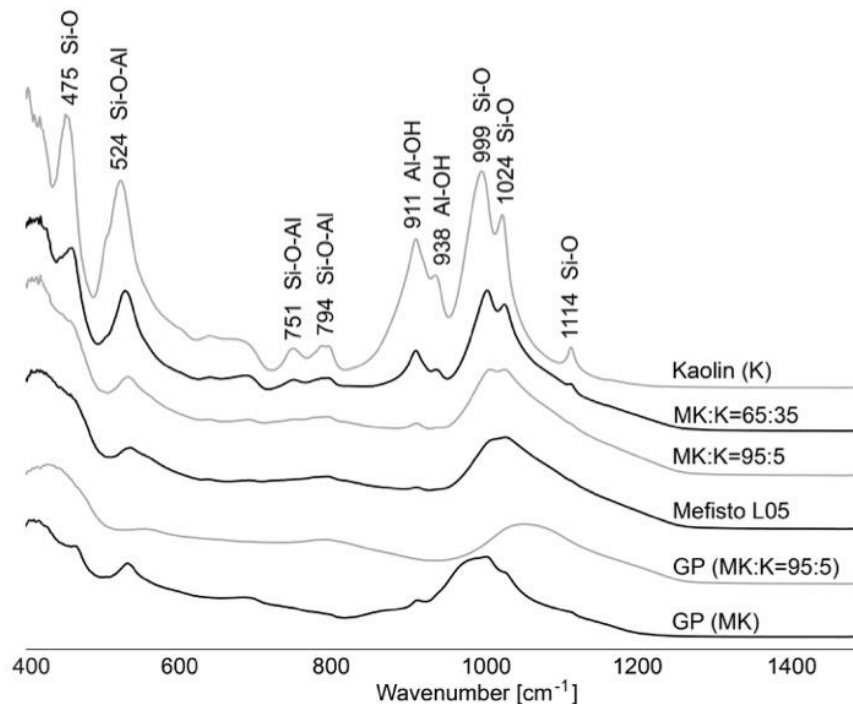


Fig. 3 - FTIR spectra of the industrial metakaolin (Mefisto L05), this one burned in laboratory (Metakaolin (MK)), kaolin (K), their mixtures (MK:K=95:5 and 65:35); and the resulting geopolymer made of metakaolin (GP (MK)) and metakaolin with added kaolin (GP (MK:K=95:5)).

The presence of kaolin in the matrix sample is well seen due to the OH deformation band linked to 2Al^{3+} at 911 cm^{-1} and the Si-O-Al stretching band at 524 cm^{-1} [20]. Furthermore, kaolin and the reference-scale samples were compared to the database HR Inorganics I. record of kaolinite in order to confirm the composition. The geopolymer matrix (GP (MK)) band at $930\text{--}1070\text{ cm}^{-1}$ with a maximum at 985 cm^{-1} is not so wide, but it shifted to a lower wavenumber in comparison to the metakaolin (MK) main band at $960\text{--}1250\text{ cm}^{-1}$ with a maximum at 1035 cm^{-1} . Kaolinite presence is visible in the main band of geopolymer made of metakaolin with a kaolin addition (GP (MK:K=95:5)) as a shoulder at 1032 cm^{-1} and a maximum at 1008 cm^{-1} .

Al-OH stretching bands at $3500\text{--}3650\text{ cm}^{-1}$ were also observed in kaolin samples. OH stretching bands of the physically bonded water at $3300\text{--}3500\text{ cm}^{-1}$ were observed only in both of the geopolymer samples (GP (MK:K=95:5) and GP (MK)), where the slightly higher absorbance intensity was induced by water in geopolymer matrix.

SEM Analysis

Figure 4 displays the differences between the two microstructures of the matrix with and without kaolin among quartz sand aggregates. The structures differ in their microcracks network. Whereas the matrix without added raw kaolin is more fragmented by numerous fine cracks, the matrix with added kaolin shows fewer but wider cracks. They demarcated the matrix in the areas of relaxed structural strain, unlike the crumbled matrix without raw kaolin. In this matrix, widespread light-grey crumbs were detected and identified by EDAX analyses as residual metakaolin particles (Table 2). The residues of undissolved metakaolin soaked the geopolymer and created harder parts of the matrix. The liquid precursor alone hardened into a softer background matrix that surrounded

all the objects. This is evidenced by the micromechanical properties measured by means of nanoindentation.

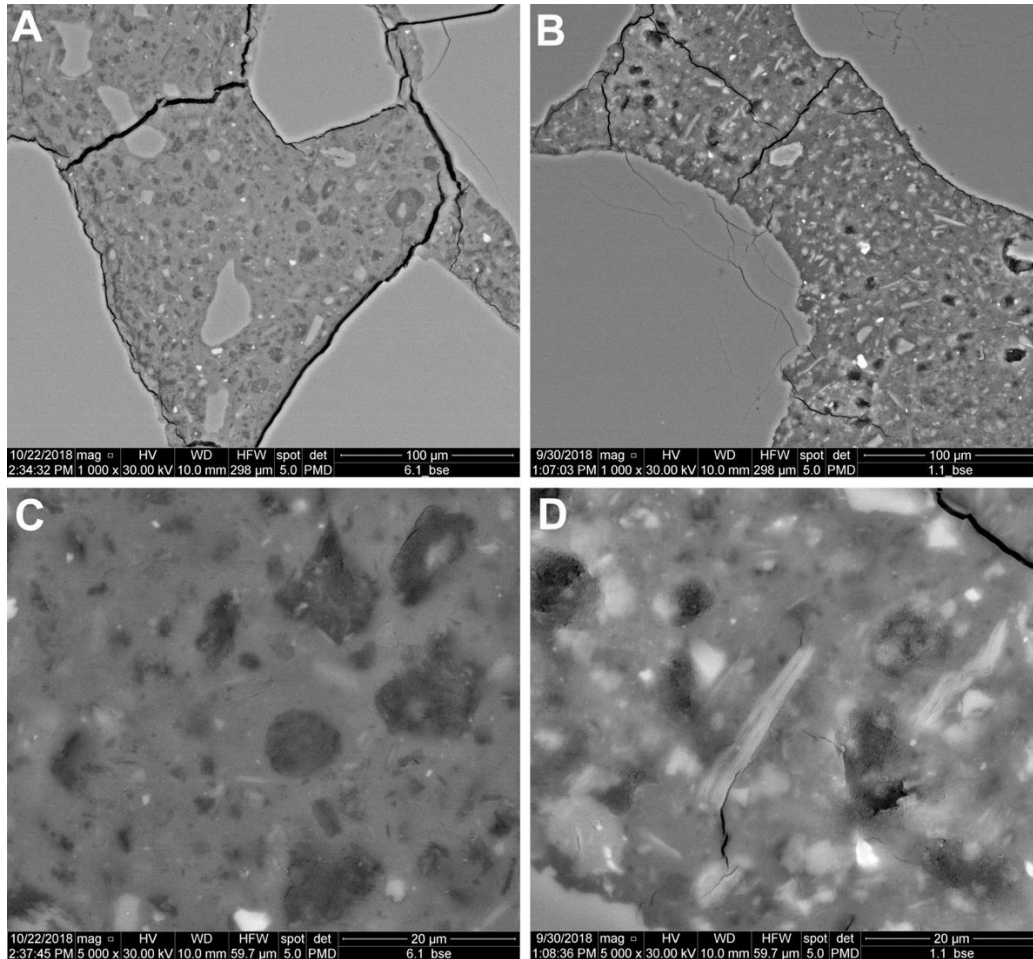


Fig. 4 - SEM micrographs of geopolimer made of metakaolin with kaolin (MK:K=95:5) (A; C) and metakaolin (B; D) carried out on a Quanta 450 SEM.

Tab. 2 - EDAX spot analysis [wt%] of the geopolimer matrix-microstructure parts and objects (averaged results). MK = metakaolin, K = kaolin.

Spots in structure	Weight percentage (average results) [wt%]						
	Al ₂ O ₃	SiO ₂	Na ₂ O	K ₂ O	CaO	FeO	TiO ₂
Background	24	61	10	<1	2	<1	<1
MK residues	27	60	7	<1	3	<1	<1
K floccules	36	58	2	<1	<1	<1	<1

The elasticity modulus (E) of the background matrix containing finely dispersed kaolin reached up to 15.2 GPa, unlike the pure matrix, where the results were split into the values of the background matrix (10 GPa) and the metakaolin residues (12 GPa). Both were of lower E than the matrix with kaolin. The differences among micromechanical properties are in accordance with the

results of the mechanical properties. In the homogeneous microstructure, with a 5 wt% of kaolin, metakaolin was probably better dissolved. This could have been caused by the significantly delayed hardening of the samples with kaolin. During the prolonged dwell in the liquid alkaline medium, the metakaolin had more time to dissolve without “freezing” its whole particles. This could increase monomer-precursor superiority. Thus, the metakaolin can participate in polycondensation towards the structure’s densifying and strengthening.

In Figure 5, the most common components of the microstructure are shown in detail: quartz aggregates, mesopores of the size of about 10-20 μm , under 10 μm and smaller particles such as metakaolin residues, quartz, mica, and other impurities.

The added kaolin particles were difficult to detect because of their addition in the form of a colloid suspension. Some bigger kaolin floccules were detected by EDAX and are indicated in Figure 5 by white asterisks. The higher concentration of kaolin slowed down the matrix chaining and setting, which was the reason for the delay in the products’ hardening. The floccules reduced the internal strain and partly acted as a structural buffer hindering the spread of microcracks, which contributed to mechanical strength (at least up to the 20 wt% addition of kaolin in metakaolin). For the frost resistance, however, the higher concentration was less effective, probably because of the water retention.

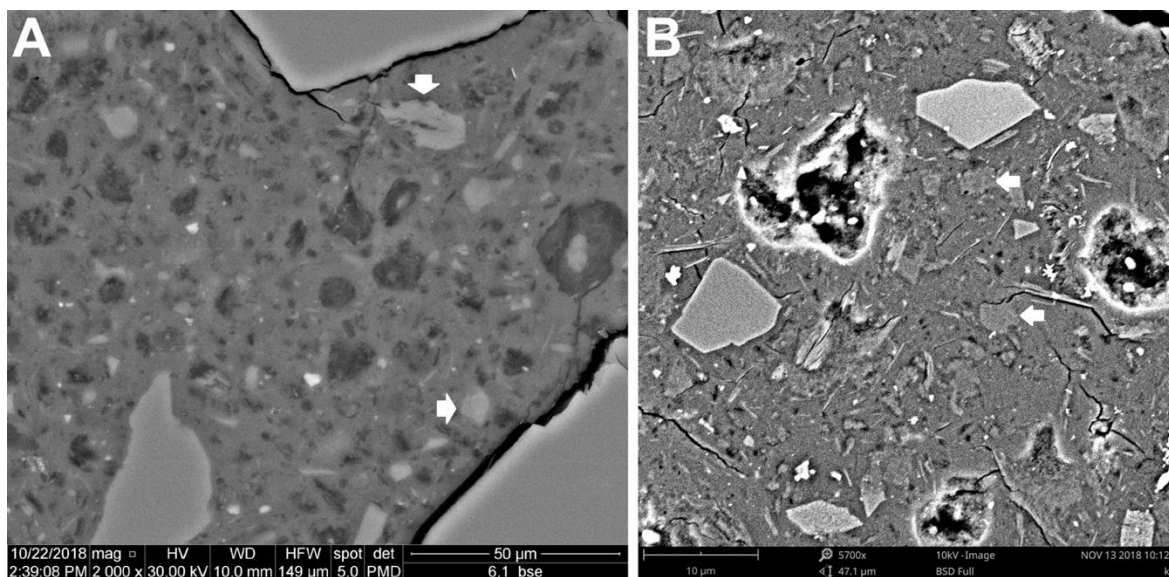


Fig. 5 - Micrographs of geopolymer made of metakaolin with kaolin (MK:K=95:5) with visible particles of kaolin highlighted by white asterisks; (A) carried out on a Quanta 450 SEM, (B) more detailed using a Phenom XL Desktop SEM.

CONCLUSION

This work aimed to study kaolin residues after the industrial metakaolin burning by comparing the influence of the raw kaolin addition to metakaolin on the mechanical properties of the resulting geopolymer products.

Despite the weakness of kaolin and although the raw kaolin is known to be non-convertible into geopolymer chains, it was found that kaolin spoiled neither the polycondensation nor the product solidification. Moreover, it was found out that the solid did not crumble in water in a wide range of kaolin content (2-50 wt%) during testing. A further benefit of the measurement was the finding that

a small amount of kaolin in metakaolin (up to 3 wt%) improved the geopolymer performance in compressive and flexural strength tests after frost-resistance tests in comparison with no-frost samples. Also, the presence of up to 20 wt% of kaolin did not affect the flexural strength of the geopolymer but slightly improved compressive strength. Based on the obtained results, monetary savings in large volume production can be achieved by either admixing raw kaolin into metakaolin or proper regulation of the burning process.

REFERENCES

- [1] Davidovits J., 2017. Geopolymers: Ceramic-Like Inorganic Polymers. *Journal of Ceramic Science and Technology*, vol. 8(3): 335-350. DOI: 10.4416/JCST2017-00038
- [2] Khale D., Chaudhary R., 2007. Mechanism of Geopolymerization and Factors Influencing Its Development: A Review. *Journal of Materials Science*, vol. 42: 729-746. DOI: 10.1007/s10853-006-0401-4
- [3] Škvára F., 2007. Alkali Activated Materials or Geopolymers? *Ceramics Silikáty*, vol. 51(3): 173–177
- [4] Škvára F., 2008. Geopolymer Concrete: An Ancient Material Too? *Ceramics Silikáty*, vol. 52(4): 296-298
- [5] Komnitsas K.A., 2011. Potential of Geopolymer Technology Towards Green Buildings and Sustainable Cities. *Procedia Engineer*, vol. 21: 1023-1032. DOI: 10.1016/j.proeng.2011.11.2108
- [6] Van Deventer J.S.J., Provis J.L., Duxson P., 2012. Technical and Commercial Progress in the Adoption of Geopolymer Cement. *Minerals Engineering*, vol. 29: 89–104. DOI: 10.1016/j.mineng.2011.09.009
- [7] Zhang Z.H., Zhu H.J., Zhou C.H., Wang H., 2016. Geopolymer From Kaolin in China: an Overview. *Applied Clay Science*, vol. 119: 31–41. DOI: 10.1016/j.clay.2015.04.023
- [8] Parthiban K., Vaithianathan S., 2015. Effect of Kaolin Content and Alkaline Concentration on the Strength Development of Geopolymer Concrete. *International Journal of Chemtech Research*, vol. 8: 0974-4290. ISSN: 0974-4290
- [9] Duxson P., Lukey G.C., Van Deventer J. S. J., 2006. Evolution of Gel Structure During Thermal Processing of Na-Geopolymer Gels. *Langmuir*, vol. 22(21): 8750-8757. DOI: 10.1021/la0604026
- [10] Duxson P., Lukey G. C., Van Deventer J. S.J., 2007. Thermal Evolution of Metakaolin Geopolymers: Part 2 – Phase Stability and Structural Development. *Journal of Non-Crystalline Solids*, vol. 353: 2186–2200. DOI: 10.1016/j.jnoncrysol.2007.02.050
- [11] Davidovits J., 1994. High-Alkali Cements For 21st Century Concretes. In *Symposium: Concrete Technology, Past, Present and Future*, 383–397
- [12] Van Deventer J.S.J., 2017. *Handbook of Low Carbon Concrete*, Chapter 10. ISBN: 978-0-12-804524-4
- [13] Autef A., Joussein E., Gasgnier G., Pronier S., Sobrados I., Sanz J., Rossignol S., 2013. Role of metakaolin dehydroxylation in geopolymer synthesis. *Powder Technology*, vol. 250: 33-39. DOI: 10.1016/j.powtec.2013.09.022
- [14] Wang H., Li H., Yan F., 2005. Synthesis and Mechanical Properties of Metakaolinite-Based Geopolymer. *Colloids and Surfaces A-Physicochemical and Engineering Aspects*, vol. 268: 1–6. DOI: 10.1016/j.colsurfa.2005.01.016
- [15] ČSN EN 1015-11 (722400), 1999. Zkušební metody malt pro zdivo – Část 11: Stanovení pevnosti zatvrdělých malt v tahu za ohybu a v tlaku.
- [16] ČSN 73 1322, 1969. Stanovení Mrazuvzdornosti Betonu. Praha: Český Normalizační Institut
- [17] ICDD PDF-2 Database, Version 2013, ISDD, USA
- [18] HR Inorganics I. – Minerals Database – FTIR, 2016. Thermo Scientific™ Omnic™, USA
- [19] Oliver W.C., Pharr G.M., 2004. Measurement of hardness and elastic modulus by instrumented indentation: Advances in understanding and refinements to methodology. *Journal of Materials Research*, vol. 19(1). DOI: <https://doi.org/10.1557/jmr.2004.19.1.3>
- [20] Bhaskar J.S., Gopalakrishnarao P., 2010. Fourier Transform Infrared Spectroscopic Characterization of Kaolinite from Assam and Meghalaya, Northeastern India. *Journal of Modern Physics*, vol. 1: 206-210. DOI: 10.4236/jmp.2010.14031

FLEXURAL PERFORMANCE OF COLD-FORMED THIN-WALLED STEEL-PAPER STRAW BOARD COMPOSITE SLAB

Xiuhua Zhang, Zilin Zhao, Xiang Li

*School of Civil Engineering, Northeast Forestry University, No. 26 Hexing Road,
150040 Harbin, China; 839714364@qq.com*

ABSTRACT

A new type of composite slab was proposed by connecting paper straw board and cold-formed thin-walled steel with self-tapping screws. In order to investigate the failure process and failure mode of the composite slab, the tests on the flexural capacity of three composite slabs with different factors such as steel beam section size, beam spacing and the number of screws were carried out. The strain of the cold-formed thin-walled C-shaped steel and the paper straw board, and the deflection of the composite slab were observed, respectively. Moreover, the flexural behaviour and the composite action of the composite slab were investigated and the flexural capacity of the composite slab was obtained. It was found that the final failure mode of composite slab was the local buckling mode of cold-formed thin-walled C-shaped steel beam due to the adequate restraint of the straw board, and the reducing of the screw spacing had beneficial influence on the flexural yield capacity. The calculation method of midspan deflection and flexural capacity of composite slab were proposed, and the calculated values of deflection and flexural capacity agreed well with the test results. Therefore, the new composite slabs were of good working performance and high flexural capacity.

KEYWORDS

Composite slab, Paper straw board, Cold-formed thin-walled steel, Failure process, flexural behaviour

INTRODUCTION

Straw is a natural product of crops. At present, there is an oversupply of straw, which makes it cheap and easy to access in most countries. Because people are not aware of the cost and economic value of straw in many industries, it has not been widely used. The world's largest rice cultivators, such as India and China, suffer tremendously from the straw problems, because most of the current treatment methods are incineration on the spot. It not only wastes resources but pollutes the environment, and has a great impact on people's physical and mental health. Therefore, it is an urgent problem to make full use of the abundant straw resources for waste utilization. The employment of the renewable energy resource in buildings is greatly consistent with the concept of sustainable development, so paper straw board as a new environmentally protection building material emerges at the right moment [1-2].

Paper straw board (hereinafter called straw board) is a new environmentally friendly building material made from rice straw, which is directly heated and extruded in the molding machine to form a compact board, and glued on the surface with a layer of "protecting paper" of various materials. Straw board has many advantages as building materials. Firstly, straw board is more low-carbon and environmentally friendly than traditional building materials in terms of production and use. Secondly, it has good physical properties, including high strength, good seismic performance, excellent thermal insulation, good fire resistance and other characteristics.

Finally, it is cheap, which helps to reduce construction costs [3]. Studying lightweight composite members such as composite slabs and composite walls sheathed with straw boards can give full play to the respective advantages of different composite materials. It can not only use agricultural straw resources, reduce environmental pollution, but also conform to the new urbanization concept.

At present, compared with traditional reinforced concrete members, the lightweight composite member has the advantages of lightweight, economy and environmental protection for low-rise buildings constructed during urbanization. Slabs also play an important role as horizontal load bearing members in buildings. Up to now, many scholars had studied and applied various lightweight composite slabs [4-14] and achieved great results in stages. However, there were only a few reports on the composite action of straw board covering slab. In order to develop the type of lightweight composite slab, a new design of cold-formed thin-walled C-shaped steel-straw board composite slab was proposed. The failure process, failure mode and flexural capacity of composite slab were analyzed respectively through the experimental research on the flexural behaviour of specimens, and the deflection-load curves and load-strain curves of specimens were obtained, which provided basis for the theoretical analysis and engineering application of composite slab.

EXPERIMENT

Specimen details

According to reference [15] and *Technical Regulations for Low-rise Cold-formed Thin-walled Steel Buildings* (JGJ227-2011) [16], three composite slab specimens were tested for flexural capacity. The nominal short lip length and the nominal long lip length of specimens were 1200 and 2400mm, the span of support was 2200mm, and the straw board used for the specimen had a size of 2400mm×1200mm×58mm, respectively. The composite slabs were composed by the Q235B galvanized cold-formed thin-walled C-shaped steel and U-shaped track. The C-shaped steel beam and the U-shaped track were connected by ST3.5 self-tapping screw with a length of 16 mm, while the composite slab was connected by steel frame and straw board through ST4.8 self-propelled screws with a length of 75 mm, respectively. The self-tapping screw spacing was 150 and 300 mm in the periphery of the composite slab, and the screw spacing was 300 and 600 mm in the middle respectively. The four corners of the steel frame were respectively provided with shear connectors to ensure that possible local failures could not occur near the frame section of the support. The definitions of geometric parameters of specimen were illustrated in Figure 1 and specific parameters were listed in Table 1.

Tab. 1- Design parameters of specimens

Specimen no.	Slab size L×H/m	Beam type	Beam number	side beam type	Beam spacing /mm	Screw spacing /mm	
FL-1	2.4×1.2	C150×50×20×1.5	3	U153×50×1.5	600	150	300
FL-2	2.4×1.2	C150×50×20×1.5	3	U153×50×1.5	600	300	600
FL-3	2.4×1.2	C120×40×15×1.5	4	U123×40×1.5	400	150	300

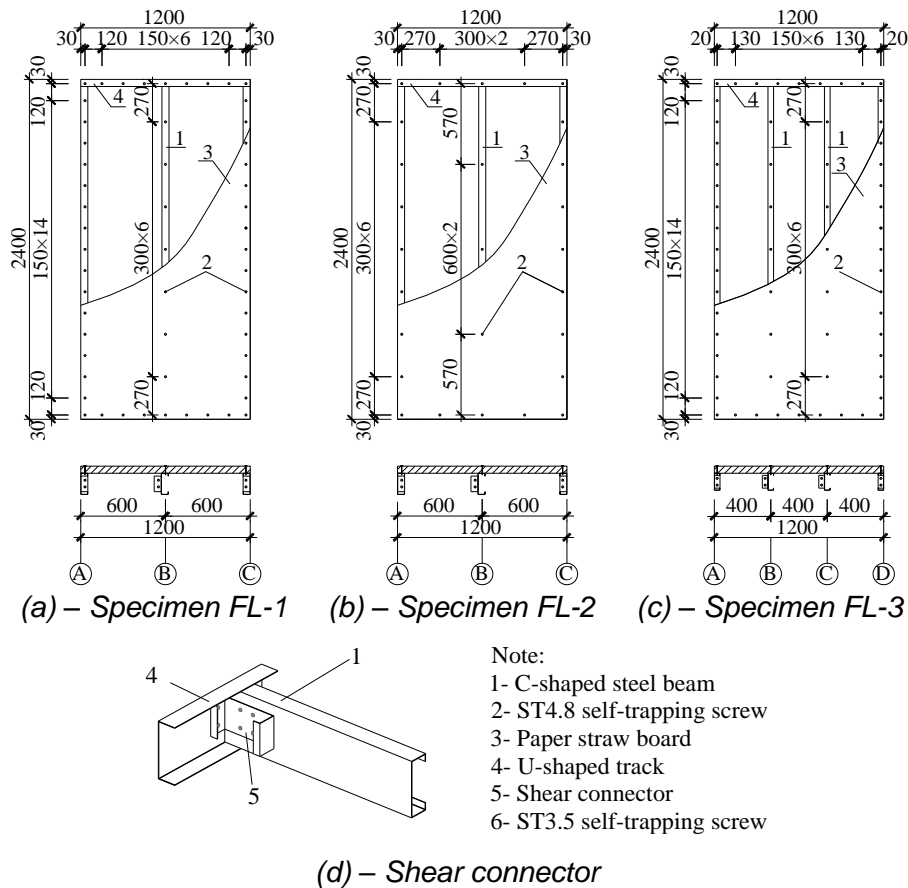


Fig. 1 – Construction and cross section of specimens

Material properties

The straw board material used in this test was provided by Harbin Tiancheng Shunjie Industrial Co., Ltd. The surface of rice straw board is flat, the thickness is 58mm, and the density is about 230-310kg/m³. 75kg sand bag is used to impact the straw board at a height of 2m, the board is not damaged, and the impact resistance is good. The fire endurance is more than 1h, and the sound insulation of single side is up to 30dB. The steel frame was the Q235B galvanized cold-formed thin-walled steel produced by Angang with a thickness of 1.5mm. According to the *Tensile Test of Metal Material Part I: Room Temperature Test Method* (GB/T228.1-2010) [17], the steel was tested for metallic material properties as shown in Table 2.

Tab. 2- Mechanical properties of steel

Thickness /mm	Yield strength/MPa	Tensile strength/MPa	Elastic modulus/GPa	Elongation /%
1.5	274.3	372.7	198.3	31.97

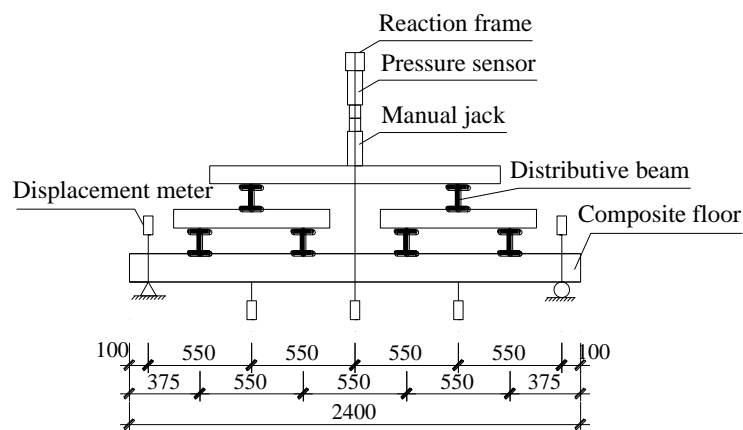
The straw in the straw board was arranged in a herringbone shape and a kind of anisotropic materials. In accordance with the *Test Methods for Mechanical Properties of Wood-based Panels for Structures* (GB/T31264-2014) [18], the mechanical properties of paper straw board were listed in Table 3.

Tab. 3- Mechanical properties of paper straw board

Type	Rice straw direction	Flexural strength/MPa	Elastic modulus/MPa
Compression resistance	Parallel	0.67	358.5
	vertical	1.42	285.8
Flexural resistance	Parallel	1.87	400.6
	vertical	0.63	233.7

Test set-up and procedures

To simulate the uniform gravity loading of specimens, the test device applied for four-point bending test was shown in Figure 2. The specimen was simply supported with roller support on one side and pin support on the other side, and the fulcrum was 100mm away from the end of specimen, respectively. The specimen should be placed on the support along the length direction for adjustment and positioning. A 16t manual jack was used to apply the load through four spreader beams.



(a) – Test loading device



(b) – Test photo

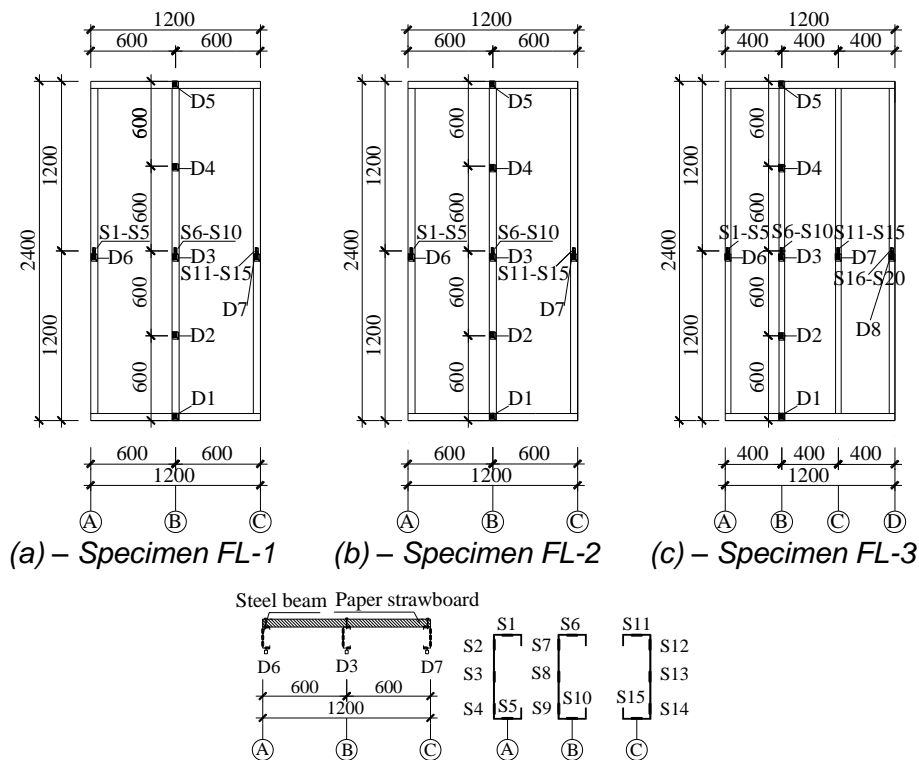
Fig. 2 – Test set-up

The test loading system adopted the grading loading mode, which was carried out by the load control, and the load per stage did not exceed 10% of the estimated maximum load of each specimen. The preload was performed first before the official test, which preload was 5%~ 10% ultimate loads. After preloading, then unloaded, and then officially loaded. The load was kept for 1min after applying 4kN to each stage, and then data was collected. After the buckling of cold-

formed thin-walled C-shaped steel beam, the deformation of the specimen was observed and the relevant data and phenomena were recorded until the load reached the maximum value. When the load decreased to 80% of the peak load, it stopped loading.

Measuring-points arrangement

The test specimens were all symmetrical structures. In order to measure the variation of deflection and strain of specimens under flexural, the layout of the test points was shown in Figure 3. The displacement gauges labelled as D1-D8 were arranged to measure the deflection of specimen, and the strain gauges labelled as S1-S20 were arranged to measure the strain of specimen. In addition, five strain gauges were arranged on the upper and lower flanges and webs of each steel beam in the middle-spans, while three strain gauges were arranged on the upper and lower surfaces of straw board midspan section.



(d) – 1-1 Layout of measuring points

Fig. 3 – Measuring-point arrangement

THE TEST PHENOMENON

Test process and failure characteristics

(1) For specimens FL-1 and FL-2:

The stress process and failure phenomena of the test showed the basically same as that of specimen FL-1. Taking FL-1 as an example, the test process and failure characteristics were as follows. Firstly, the straw board and the steel frame were tightly connected and of good elasticity in the initial stage of the loading process, so deformations of the two were consistent. Both specimen FL-1 and FL-2 were in the elastic range, the wrinkles had appeared on the surface of the straw

board at the lower end of the spreader beam, and the steel and straw board were well coordinated. In addition, the specimen continued to emit a slight sound during the loading process. Then as the load increased, the wrinkles of the straw board gradually expanded outward, and the lower end of the spreader beam presented shallow concave wrinkles on the surface. The midspan deflection reached 12mm when the load reached about 40kN. Meanwhile, the straw board was deformed at the lower end of the spreader beam and the self-tapping screws near the middle of the specimen sank into the straw board (Figure 4(b)). There was severe torsion outside the plane to appear in the steel beams of specimen, which the outer steel beam-A was observed the largest rotation and obviously local buckling (Figure 4(c)), the middle steel beam-B was slightly torsional and local buckling (Figure 4(d)), the steel beam-C deformed slightly (Figure 4(e)), and the steel beams and straw board began to be separated. When the loading continued to 57.6kN, the pressure sensor reading decreased, there was a loud noise from the specimen suddenly, the steel beam-A was in lateral torsion and severe buckling failure occurred, and the failure degree of three beams decreased gradually from outside to inside, respectively. It was considered that the ultimate flexural capacity had been reached at this time. Lastly, the midspan deflection reached 20 mm at the end of the loading. Wrinkles on the straw board could be found, the bend of specimen could be observed obviously, and the steel frame was clearly separated from the straw board (Figure 4(f)). After unloading, removed the straw board and observed the failure of the steel frame (Figure 4(g)). The rest of the steel frame was basically intact except for the buckling failure of the side steel beam-A and the middle steel beam-B (Figure 4(h)), and the slight deformation of the steel beam-C, the upper and lower tracks and the supports.



(a) – Structural failure of specimen FL-1 (b) – Sinking of self-tapping screw



(c) – Local buckling of steel beam-A (d) – Tendency of lateral torsion buckling of steel beam-B

Fig.4 – Failure modes of specimen FL-1



(e) – Deformation of steel beam-C



(f) – Separation of straw board and steel beam



(g) – Destruction of steel frame



(h) – Buckling failure details of steel beam-A and beam-B

Fig.4 – Failure modes of specimen FL-1

For the specimen FL-2, the increment was stable when the load is small, and there was no obvious deformation. Slight torsion occurred to the steel beams when loading to 38kN, both sinking of the self-tapping screw and separation of straw board and steel frame took place, and severe local buckling was observed on the outer steel beam-A and the middle steel beam-B webs at the same time. When the loading was continued to 55kN, the pressure sensor reading began to decrease and then was regarded as the specimen's ultimate bearing capacity of the load, buckling failure occurred to the outer steel beam-A (Fig. 5(b)), and the midspan deflection reached 26 mm.



(a) – Destruction of steel frame



(b) – Local buckling of steel beam-A web

Fig.5 – Failure modes of specimen FL-2

(2) Specimen FL-3:

When the loading started, the load-deflection curve increased linearly and the deformation of the straw board and steel frame were consistent. The deformation continued to increase as the load increased to about 39kN, the specimen emitted a "squeak" sound in the loading process, and the straw board and the steel frame were slightly separated. Meanwhile, the midspan deflection reached 15mm. The load could not increase anymore when the load reached 56kN, that was to say, it reached its peak. Flexural buckling occurred to the outer steel beam-A (Figure 6(b)) and wrinkles on the straw board were observed respectively, while the midspan deflection reached 30mm.



(a) – Destruction of steel frame



(b) – Buckling failure of steel beam-A

Fig.6 – Failure modes of specimen FL-3

ANALYSIS OF TEST RESULTS

Load-strain curve and analysis

The relationship curve between the load of test piece FL-3 and the strain of midspan section is shown in Figure7.

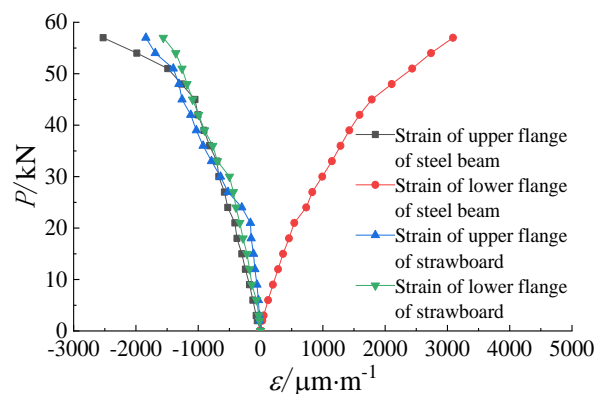


Fig.7 – Load-strain curves of midspan section

The upper flange of the C-shaped steel bears compressive stress while the lower flange bears tensile stress. Since the neutral axis of specimen is located above the symmetrical axis of the C-shaped steel due to composite action, the strain value of the tensioned side is larger than that of the compressed side.

In the initial stage of loading, the specimen is in the elastic stage and the load-strain curve grows linearly. The load-strain curve grows nonlinearly with the increase of load, and the specimen enters the elastoplastic stage. When the specimen approaches to the ultimate flexural capacity, the strain of the upper and lower flanges of the steel beam exceeds $2000\mu\epsilon$ indicating the steel beam exceeds the yield strength and the material properties of the steel beam are well applied. When the load is exerted, the strain values of upper and lower surface of the straw board are close to those of upper flange of the steel beam showing that the steel beam agrees well with the straw board and the overall working performance of the specimen formed by steel frame and the straw board is excellent. In addition, the strain values of the upper and lower surfaces of the straw board are negative indicating that the whole section of the straw board bears compressive stress during the whole loading process, which makes full use of the compressive performance of the straw board and avoids the shortcomings of poor tensile capacity of it. The load-strain curve of other specimens is similar to that of FL-3.

Figure 8 shows the distribution of the longitudinal strain along the height of the midspan section of the steel beam of the specimen. The abscissa represents the longitudinal strain of the section, the ordinate represents the height along the section, $y=0\text{mm}$ expresses the edge of the lower flange of the steel beam, and $y=150\text{mm}$ expresses the edge of the upper flange of the steel beam. It can be seen from Figure 7 and Figure 8 that the strain values of the upper and lower surface of the straw board are close to those of the upper flange of the steel beam. Therefore, the longitudinal strain distribution of the steel beams and the straw board basically conforms to the plane section assumption.

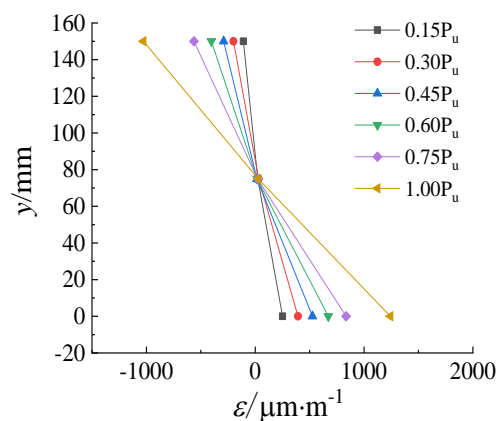


Fig.8 – Distribution of strain along the web of the midspan section of steel beam of specimen

Load-deflection curve and analysis

The load-deflection curves of three specimens are shown in Figure 9. The specimen is in the elastic stage at the initial stage of loading, the deflection of the specimen presents a linear growth, and the straw board and C-shaped steel show a good composite action. With the increase of load, the specimen enters the elastoplastic stage, the buckling of steel girder flange is caused by compression, the deflection of the midspan increases rapidly, and the flexural stiffness decreases. Continue loading, the buckling deformation of the specimen increased faster and the specimen is destroyed after reaching the ultimate flexural capacity. Continue loading after the load on the specimen reaches its ultimate flexural capacity, the load still decreases. Not stop loading until the load decreases to 80% of the ultimate flexural capacity.

Comparing the load-deflection curve of FL-1 and that of FL-2: the load-deflection curves of the two specimens almost coincide in the initial stage of loading and the screw spacing has no effect on the flexural capacity and flexural rigidity of the specimen. As the load increases, the specimen enters elastoplastic stage, the screws start to function, and the straw board restrains the steel frame to enter plastic stage. Increasing the screw spacing makes the lateral brace length of the specimen larger and the beam prone to local buckling. Therefore, the flexural rigidity of the specimen FL-2 with larger screw spacing decreases faster after buckling and the ultimate flexural capacity is smaller. Comparing the load-deflection curve of FL-1 to that of FL-3: the two load-deflection curves begin to separate after the initial loading stage, the flexural rigidity of FL-3 is smaller than that of FL-1, the ultimate flexural capacity of the two specimens are similar, but the flexural capacity of FL-3 decreases significantly faster after reaching the maximum load. The results indicate that the section size makes less influence on the stiffness of the member.

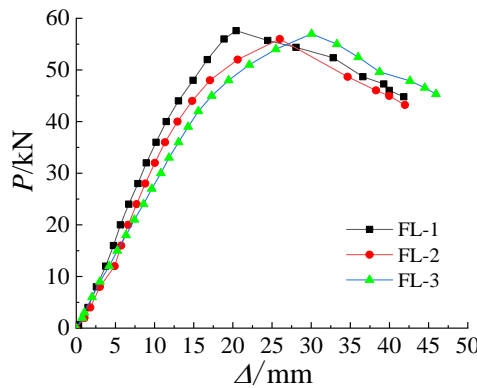


Fig.9 – Deflection-load curves

Flexural capacity characteristic value

The highest point on the load-deflection curve is the maximum load that the specimen can bear. After exceeding the load, the load-deflection curve enters the decreasing stage, the buckling failure appears to the steel beam, and then the load is continuously applied to cause the overall failure of the specimen. Because the flexural capacity of the specimen is mainly provided by the steel beam, so the corresponding load is defined as the yield load of the specimen when the steel beams of the specimen midspan begins to yield, that is, the load where the slope of the load-deflection curve suddenly changes is taken as the yield load of the specimen. The ultimate load and the ultimate displacement are the corresponding points when the load in the descending section is equal to 85% of the maximum load. According to the test results, yield load, ultimate load, midspan flexural displacement and the maximum displacements corresponding to ultimate load of three steel-straw board composite slabs are obtained as shown in Table 4.

Tab. 4 - Results of the test

Specimen No.	Yield load		Maximum load		Ultimate load	
	P_y /kN	Δ_y /mm	P_{max} /kN	Δ_{max} /mm	P_u /kN	Δ_u /mm
FL-1	39.92	11.39	57.60	20.42	48.96	37.29
FL-2	35.75	11.19	56.00	25.99	47.60	36.11
FL-3	36.92	13.45	57.00	30.04	48.45	40.63

According to the deflection limit requirements of flexural members in *Technical Specification for Low-rise Cold-formed Thin-walled Steel Buildings* (JGJ227-2011), the deflection limit of specimens is 11mm ($L/200$). When the specimens FL-1, FL-2, and FL-3 reach the serviceability limit state, the corresponding loads are 17.65kN/m², 16.05kN/m², and 14.02kN/m², respectively about 66.86%, 62.55% and 53.67% of their maximum loads. Therefore, it is important to improve the stiffness for member to meet the serviceability limit state. The test results show that the yield load of specimen FL-1 with smaller screw spacing is 11.66% higher than that of specimen FL-2 with larger screw spacing, indicating that the screw spacing effects the yield load of the specimen significantly.

Comparison results of tests

In order to make comparison of the test results more accurate, the composite slabs with the same section height are selected, and the flexural capacity of the composite slabs in other papers is converted into the unit width of flexural capacity. The test results of two specimens in this paper are compared with those of lightweight composite slab specimens in other papers as shown in Table 5.

Compared with different cover panels, the flexural capacity of cold-formed thin-walled C-shaped steel-straw board composite slab is about 41% higher than that of cold-formed thin-walled C-shaped steel-bamboo rubber composite slab. Compared with different steel types, the flexural capacity of cold-formed thin-walled C-shaped steel-straw board composite slab is increased by about 7.2% than that of profiled steel sheet-straw board composite slabs. Compared with different cover panels and steel types, the flexural capacity of cold-formed thin-walled C-shaped steel -straw board composite slab is about 12.4% higher than that of profiled steel sheet-straw board composite slabs. It can be seen from the results that the maximum displacement of cold-formed thin-walled C-shaped steel-straw board composite slab is larger, but its flexural displacement is smaller, indicating that its deformation capacity is better in the elastic stage. Obviously, the cold-formed thin-walled C-shaped steel-straw board composite slab exhibits the high flexural capacity.

Tab. 5 - Comparison of test results

Paper	Specimen No.	Steel yield Strength /MPa	Covering slab type	Steel type	Steel thickness /mm	Connection type	M_t /kN·m	Δ_{max} /mm
This paper	FL-1 FL-3	274.3	58mm thick straw board	cold-formed thin-walled C-shaped steel	1.5	self-propelled screw	11.01 10.03	20.42 30.04
paper5	B-3 B-4	265.5	double 5.2-11mm bamboo plywood	profiled steel sheet	0.7 0.7	sticky	6.84 8.07	22.51 16.10
paper9	B-1 B-2	334.04	double 9mm bamboo plywood	cold-formed thin-walled C-shaped steel	1.0	self-propelled screw, sticky, stainless steel rivet	10.01 9.61	23.74 24.19
paper1 2	S-1 S-4	235.0	one-sided 58mm thick straw board	profiled steel sheet	0.8 0.8	self-propelled screw	9.05 9.67	13.00 17.54

THE THEORY ANALYSIS

Calculation of deflection

It can be seen from the test results that the straw board and the steel beam are in the elastic stage under the serviceability limit state, the strain values of the two materials are basically similar, and the composite action is better. Therefore, it can be regarded as an integral elastic member for calculation when calculating the stiffness of composite slab.

According to the equation of material mechanics, the flexural stiffness of the composite slab is calculated according to Equations. (1):

$$EI_x = E_d I_d + E_s I_s \quad (1)$$

Where E_d is the elastic modulus of the straw board, I_d is the moment of inertia of the straw board to the neutral axis, E_s is the elastic modulus of the steel beam, taking $1.983 \times 10^5 \text{MPa}$, and I_s is the moment of inertia of the steel beam to the neutral axis.

The equation for calculating the midspan deflection of a simple support plate under uniform load is as follows:

$$\Delta = \frac{5ql^4}{384EI_x} \quad (2)$$

This test is a four-point load and the known deflection is calculated as:

$$\Delta = \frac{6.04Pl^3}{384EI_x} \quad (3)$$

Combining Eqs. (3) and (4), the uniform load of the composite slab is calculated as:

$$q = \frac{1.21P}{lb} \quad (4)$$

Where Δ is the midspan deflection of the composite slab, P is the load value of the composite slab obtained by the test, l is the distance between the two supports, E is the elastic modulus of the steel beam and is taking as $1.983 \times 10^5 \text{MPa}$, I_x is the inertia moment of the composite slab and b is the width of the composite slab.

The loading mode used in the test is to simulate the uniform load at the four points. The experimental deflection value Δ_t and theoretical deflection value Δ_c are compared when the composite slabs achieve yield strength as shown in Table 6. The test deflection value is in good agreement with the theoretical deflection value in Table 6, and the error is controlled within 13%. Therefore, it is feasible to calculate the deflection using the Equations. (2) during the normal service stage of the composite slabs.

Tab. 6 - The deflection value of the composite slabs

Specimen No.	Δ_t/mm	Δ_c/mm	Δ_c/Δ_t
FL-1	11.39	11.04	0.97
FL-2	11.19	9.91	0.89
FL-3	13.45	13.47	1.01

Calculation of flexural capacity

The composite action associated with the straw board and steel frame demonstrates a better performance and the straw board and the steel beam can deform cooperatively according to the test results. Following the theory of sectional flexural capacity of composite structures, the failure section of composite slab is calculated as follows:

(1) When the flexural capacity of the specimen decreases to 85%, it is considered the failure of it while the upper and lower flanges of the steel beam yield currently.

(2) When the failure of specimen takes place, the strain of the straw board takes the yield strain of the steel beam, the whole section of the straw board bears pressed and it is always in the elastic stage.

According to the above conditions, the equations for calculating the flexural capacity of composite slabs are as follows, and the sectional form of the composite slab is shown in Figure 10.

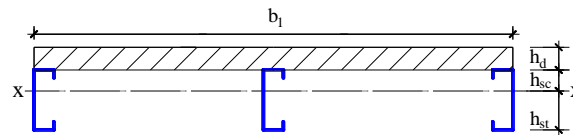


Fig.10 – Section form of composite slab

$$M = n\phi f_{ys} (A_{sc} h_{sc} + A_{st} h_{st}) / 2 + \sigma_d A_d (h_{sc} + h_d / 2) \quad (5)$$

Where n is the number of steel beams, f_{ys} is the buckling strength of the steel beam, ϕ is the integral stability coefficient of the steel beam and is taking as 0.9, h_{sc} is the distance from the resultant force center of the steel beam to the neutral axis, h_{st} is the distance from the resultant center of the steel beam compression zone to the neutral axis, A_{sc} is the sectional area of the steel beam compression zone, A_{st} is the sectional area of the steel beam tension zone, σ_d is the compressive strength of the straw board, A_d is the conversion area of the straw board, h_d is the thickness of the straw board. According to Eqs. (5), the flexural capacity of the normal section of the specimens FL-1~FL-3 are calculated as shown in Table 7.

Tab. 7 - Flexural capacities of composite slabs

Specimen No.	M_t /mm	M_c /mm	M_c / M_t
FL-1	11.09	11.39	1.03
FL-2	9.94	10.06	1.01
FL-3	10.23	10.01	0.98

M_c is the theoretical calculation value and M_t is the test value. It is found that the error between the theoretical deflection value and the test value is within 3% suggesting that Eqs. (5) can be used to calculate the flexural capacity of the composite slab.

CONCLUSIONS

(1) The tendency of lateral torsion buckling appeared, but the ultimate failure mode was local buckling of the steel beam, which indicated the straw board restrains the lateral torsion buckling of the lower steel beams.

(2) The composite action of the cold-formed thin-walled C-shaped steel-paper straw board composite slab is considerable, the straw board and the steel beam can deform coordinatively and fully exert the compressive performance of the straw board. Furthermore, the composite slab has high flexural capacity and meets the deflection limit of lightweight slab under the serviceability limit state, so it could be used in construction.

- (3) Reducing the screw spacing between straw board and steel beam can significantly increase the yield load of composite slab, so the screw spacing should be moderately reduced to improve the flexural capacity of composite slab.
- (4) Compared with other types of lightweight composite slabs, the cold-formed thin-walled C-shaped steel-paper straw board composite slab is of fine performance in deformation and flexural capacity, which can be able to meet the requirements of lightweight slab design.
- (5) In the normal service stage, the equation is used to calculate the midspan deflection and the experimental value error of the composite slab within a reasonable range. The steel beams yield when the failure of the composite slab occur, the strain values of the straw board and the steel beam are basically the same, and the test values of the flexural capacity of composite slab agree well with that of the theoretical value. The equation for calculating the deflection and flexural capacity of composite slabs proposed is feasible.

ACKNOWLEDGEMENTS

This research is financially supported by the National Natural Science Foundation of China (51878130) and the Harbin Science and Technology Innovation Talent Research Special Foundation of China (2015RQQXJ078).

REFERENCES

- [1] Garas G., Allam M., Dessuky El.R , 2009. Straw bale construction as an economic environmental building alternative - a case study. *ARPN Journal of Engineering and Applied Sciences*, Vol. 4, No. 9: 54-59.
- [2] Taha Ashour , 2011. Performance of straw bale wall: a case of study. *Energy and Buildings*, Vol. 43: 1960-1967.
- [3] Yin X.Z., Mike L., Daniel M., 2018. Construction and monitoring of experimental straw bale building in northeast China. *Construction and Building Materials*, Vol. 183: 46-57.
- [4] Wright H.D., Evans H.R., Burt C.A., 1989. Profiled steel sheeting dryBoard composite slabs. *The Structural Engineer*, Vol. 67, No. 7: 114-129.
- [5] Li Y.S., Shan W., Huang Z.B., 2008. Experimental study on mechanical behavior of profiled steel sheet-bamboo plywood composite slabs. *Journal of Building Structures*, Vol. 29, No.1: 96-102+111.
- [6] Rahmadi A.P., Badaruzzaman W.H.W., Arifin A.K., 2013. Prediction of deflection of the composite profiled steel sheet MDF-board (PSSMDFB) slab system. *Procedia Engineering*, Vol. 54: 457-464.
- [7] Zhou X.H., Li Z., Wang R.C., 2013. Study on load-carrying capacity of the cold-formed steel joists-OSB composite slab. *China Civil Engineering Journal*, Vol. 46, No. 9: 1-11.
- [8] Shi Y., Zhou X.H., Song K., 2015. Study on flexural stiffness of cold-formed thin-walled steel joists-OSB composite slabs. *Journal of Architecture and Civil Engineering*, Vol. 32, No. 6: 50-57.
- [9] Shan W., Li Y.S., Zhang X.H., 2016. Study on flexural behavior of cold-formed thin-walled C-shaped steel-bamboo rubber composite slab slab. *Industrial Construction*, Vol. 46, No. 1: 30-35.
- [10] Kyvelou P., Gardner L., Nethercot D.A., 2017. Design of cold-formed steel composite slabing systems with partial shear connection. *Ce/papers*, Vol. 1, No. 2-3: 1899-1908.
- [11] Jaeho R., Yong Yeal K., 2018. Experimental and numerical investigations of steel-polymer hybrid slab panels subjected to three-point flexural. *Engineering Structures*, Vol. 175: 467-482.
- [12] Zhang X.H., Zhang Y.Z., Jun P., 2018. Experimental study on mechanical behavior of profiled steel sheet-strawboard composite slabs. *Journal of Building Materials*, Vol. 21, No. 6: 943-949.
- [13] Kyvelou P., Gardner L., Nethercot D.A., 2018. Finite element modelling of composite cold-formed steel slabing systems. *Engineering Structures*, Vol. 158: 28-42.
- [14] Zhou X.H., Shi Y., 2019. A simplified method to evaluate the flexural capacity of lightweight cold-formed steel slab system with oriented strand board subslab. *Thin-Walled Structures*, Vol. 134: 40-51.

- [15] Kraus, Cynthia A., 1997. Slab vibration design criterion for cold-formed C-shaped supported residential slab systems. Blacksburg: Virginia Polytechnic Institute and State University.
- [16] JGJ 227-2011, 2011. Technical specifications for low-rise cold-formed thin-walled steel buildings. China Building Industry Press.
- [17] GB/T 228.1-2010, 2011. Metallic materials tensile testing part I: method of test at room temperature. China Standards Press.
- [18] GB/T 31264-2014, 2015. Test methods for mechanical properties of structural wood-based panels. China Standard Press.

METHODOLOGY FOR CITY LEVEL URBAN ROAD NETWORK CONNECTIVITY ANALYSIS USING GEOGRAPHICAL INFORMATION SYSTEMS (GIS)

Kurre Sai Sahitya, CSRK Prasad*

Transportation Division, Department of Civil Engineering, National Institute of Technology, Warangal, Telangana, India; ksspvpcivil@gmail.com, csrk_prasad@yahoo.com

ABSTRACT

In most of the urban cities in India, the existing road network structure is unable to meet the increasing travel demand. In this context, there is a need to utilize the existing road network in a more efficient manner. To effectively utilize the existing road network, the structural parameters like connectivity, accessibility, hierarchy and morphology should be analyzed and evaluated. This study aimed to analyze and evaluate the road network structure of Hyderabad city, Telangana state, India in terms of its connectivity. Different places in Hyderabad city were considered to quantify the connectivity measures such as alpha index, beta index, gamma index, eta index, Cyclomatic number and Aggregate transportation score. Five kilometers radius buffers were drawn from the center of each location to compute the connectivity measures. The results of the study may act as a guide to the transportation planning authorities to understand the level of connectivity at each location in the city and implement better planning practices to improve the level of connectivity in the city. Geographical Information Systems (GIS) is a platform used for better decision making in urban transportation planning. The present study also tried to prove the efficiency of GIS in analyzing the connectivity based performance of the transport network structure in the study area.

KEYWORDS

Connectivity, Road network, GIS, Planning

INTRODUCTION

In the urban framework, the transportation structure is very important and helpful in the economic development of a place. The performance of a transport structure represents the quality of engineer's adherence to that place. A well organized and well-connected transport network is very substantial for continuous progress of an area. To enhance the performance and quality of the transport structure, now-a-days, specifically integrated system like Geographical Information System (GIS) is being availed.

The essential ingredients for any road network are connectivity, accessibility, hierarchy and morphology. The ease of travel to desired destinations is facilitated in a well-connected street structure. Different modes of transport, different speeds and volumes of vehicles are facilitated in a well-organized hierarchical road structure [1].

A connectivity indicator is definitely needed to evaluate how well the street structure is organized and interconnected. This can be easily quantified by the ratio of vertices to the edges in a structure [2]. The higher values of connectivity indicators represent a satisfactory

interconnectedness of roads [1]. The connectivity indicators will act as a performance and efficiency base for many organizations which are helpful in the decision making process of transportation planning [3].

Network analysis is helpful for identifying ideal ways for accommodating emergency utilities in Varnasi [4]. Transport network indices were quantified using Arc GIS software which resulted a low level of interconnections between roads in Karsagod taluk, Kerala [5]. The application of network analyst tool of Arc GIS is explained as avail for finding solutions to many network problems relevant to transport structural performance with an example of south west Delhi [6]. Transport structural performance based on connectivity is done using some connectivity indices which proved that Aurangabad has satisfactory network facilities [7]. For Dehradun city, network analyst tool of Arc GIS was used to identify solutions to many problems in transport structure [8]. There are three important indicators measuring connectivity like Alpha, Beta and Gamma proposed by Kansky 1963. With the help of these indicators, the transport structure performance based on connectivity of roads can be explained easily [9]. The road network system of Trans-Amadi, Port Harcourt in Nigeria was assessed in terms of Beta index, road density, level of connectivity, the condition of road and road types [10]. The relationship between interconnectedness and land cover changes was investigated for Lop Buri province; Thailand using graph theory based network indices [11]. The performance of the transport network structure in terms of its connectivity was analyzed using structural measures in Cooch Behar District; West Bengal, India [12]. An attempt to develop GIS based rural road database was done so that planners, decision makers, researchers and other different level authorities in the rural road sector will be benefited from the final output. The database was developed based on the structural analysis of the network in terms of connectivity, average Pavement Condition Index values of the link, shortest path analysis [13].

AIM AND OBJECTIVES OF THE STUDY

This study is aimed to analyze the efficiency of the road network structure in Hyderabad city, capital of Telangana state, India in terms of its connectivity, while the specific objectives are:

- To compute different connectivity indices for each location at five kilometer radius.
- To evaluate the level of road network connectivity for each location based on Aggregate Transportation Score.
- To establish locations with the less connected, moderately connected and well-connected network.

METHODOLOGICAL FRAMEWORK

The flow chart in Figure 1 presents the methodology used in the study to achieve the above mentioned objectives:

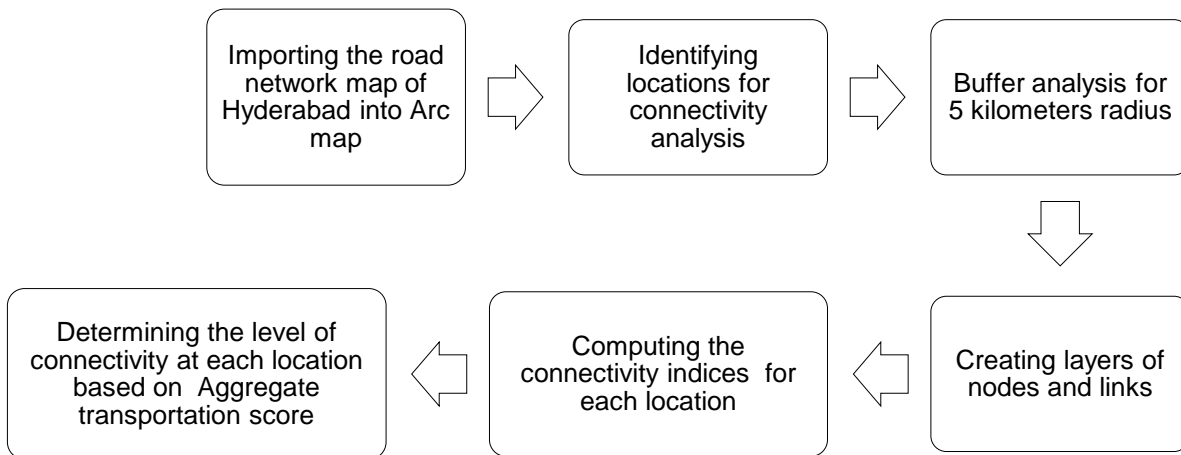


Fig. 1- Flow chart showing the methodology of the study

SITE SELECTION AND DATA PREPARATION

The digitized road network map of Hyderabad city was taken from the HUDA office and further analysis was done using it. The study area for this research is thirty locations of Hyderabad city; India selected randomly covering the entire city in all directions. The locations selected for this study are Abids (AB), Kukatpally (KP), Mehadipatnam (MP), Dilshuknagar(DN), Secundrabad (SC), Panjagutta (PG), Jeedimetla (JM), Sikenderguda (SG), Nadergul (NG), Kothapet (KT), Ameerpet (AT), Banjara Hills (BH), Gandhi nagar (GN), LB Nagar (LN), Malkajgiri (MJ), Hitech city (HC), Bhuvanagiri (BG), Ghatkesar (GS), Bhanur (BR), Moinabad (MB), Rama Chandra puram (RCP), Shivampet (SP), Sangareddy (SR), Wargal (WL), Domarapochampally (DPP), Sitharampuram (SM), Kothur (KR), GolkondaKhurd (GK), Thummaloor (TR) and Ibrahimpatnam (IBM). Buffers were drawn for each location at a radius of five kilometers. The locations selected for connectivity analysis are shown in Figure2.

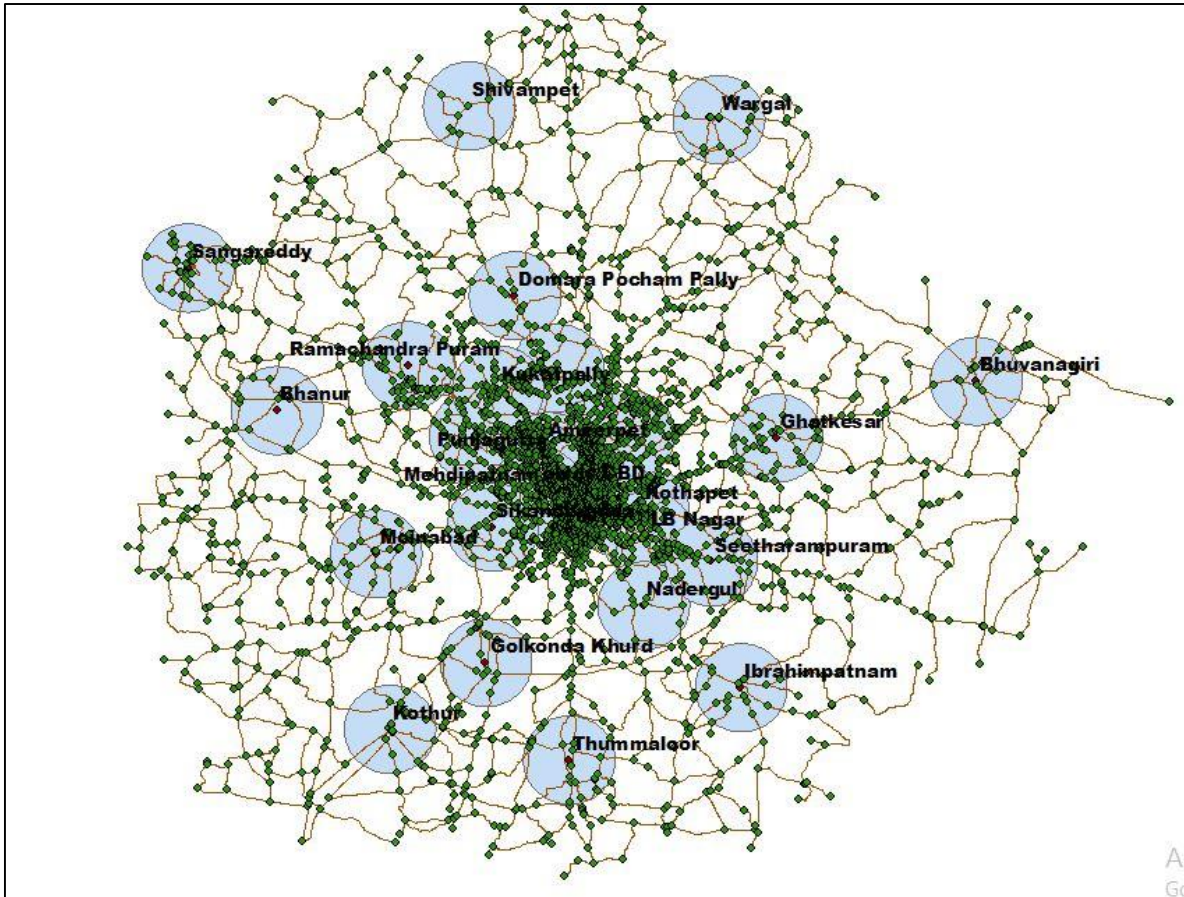


Fig. 2 - Map showing the locations along with buffers for connectivity analysis

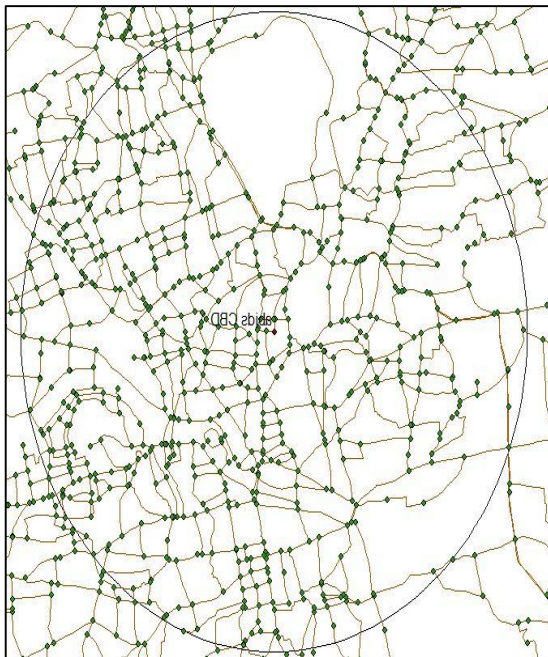


Fig. 3(a)- Nodes & Links of Abids

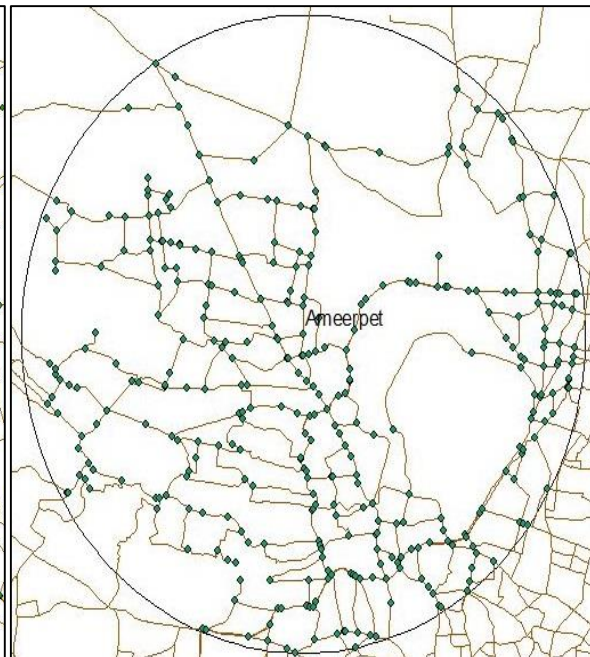


Fig. 3(b) - Nodes and Links of Ameerpet

The number of nodes and links for each location at five kilometers buffers were computed using Arc GIS 10.1 software. The nodes and links along with the 5 kilometer radius buffer for the locations Abids and Ameerpet are shown in Figures 3(a) and 3(b). Similarly, nodes and links of all the remaining locations were identified and computed using Arc GIS 10.1 software. The road network connectivity in the city is analyzed using measures of connectivity like the total number of nodes, the total number of links, alpha index, beta index (Link – Node ratio), gamma index, eta index, Cyclomatic number, Aggregate transportation score. The measures of connectivity applied in this study are described in Table 1.

Tab. 1- Description of different connectivity measures

S.NO	Name of the index	Notation & equation	Description	Relation with connectivity
1	Alpha index	$\alpha=(e-v+1)/2v-5$	e = number of edges/ links v= number of nodes/ vertices	Explains about circuitry of the network. Higher value indicates more connectivity.
2	Beta index	$\beta=e/v$	e = number of edges/ links v= number of nodes/ vertices	Explains the complexity of the network. A higher value indicates more connectivity.
3	Gamma index	$\gamma=e/3(v-2)$	e = number of edges/ links v= number of nodes/ vertices	Explains about the completeness of the network. Higher value indicates more connectivity.
4	Eta index	$\eta =L/e$	L= summation of all the edges e = number of edges/ links	Explains the utility of the given network. A higher value indicates more connectivity.
5	Cyclomatic number	$\mu = e-v+1$	e = number of edges/ links v= number of nodes/ vertices	Explains about the closeness of graphs in the network. Higher value indicates more connectivity.
6	Aggregate Transportation score	$ATS=\beta+\alpha+\gamma+\mu$	α = alpha index β = beta index γ = gamma index μ = Cyclomatic number	Higher value indicates more connectivity and efficiency.

RESULTS AND DISCUSSIONS

The measures of connectivity like alpha index, beta index, gamma index, eta index, Cyclomatic number (CN) and Aggregate Transportation Score (ATS) are computed for thirty locations at 5 kilometers buffer radius and the results are presented in Table 2.

Tab. 2- Descriptive Statistics of connectivity measures

Location	Nodes	Links	Alpha index	Beta index	Gamma index	Eta index	CN	ATS
Abids	687	1238	0.40	1.80	0.60	0.51	552	554.81
Kukatpally	117	222	0.46	1.90	0.64	0.95	106	109.00
Mehadipatnam	432	781	0.41	1.81	0.61	0.59	350	352.82
Dilshuknagar	467	829	0.39	1.78	0.59	0.59	363	365.76
Secundrabad	395	719	0.41	1.82	0.61	0.59	325	327.84
Panjagutta	447	783	0.38	1.75	0.59	0.58	337	339.72
Jeedimetla	92	173	0.46	1.88	0.64	0.98	82	84.98
Sikenderguda	86	165	0.48	1.92	0.65	0.94	80	83.05
Nadergul	32	50	0.32	1.56	0.56	1.58	19	21.44
Kothapet	286	507	0.39	1.77	0.60	0.67	222	224.76
Ameerpet	349	614	0.38	1.76	0.59	0.62	266	268.73
Banjara Hills	411	723	0.38	1.76	0.59	0.60	313	315.73
Gandhinagar	645	1147	0.39	1.78	0.59	0.50	503	505.76
LB Nagar	200	360	0.41	1.80	0.61	0.62	161	163.81
Malkajgiri	266	491	0.43	1.85	0.62	0.72	226	228.89
Hitech city	130	239	0.43	1.84	0.62	1.25	110	112.89
Bhuvanagiri	83	92	0.06	1.11	0.38	2.68	10	11.55
Ghatkesar	39	92	0.74	2.36	0.83	1.43	54	57.93
Bhanur	43	50	0.10	1.16	0.41	1.92	8	9.67
Moinabad	62	79	0.15	1.27	0.44	1.64	18	19.86
RamachandraPuram	56	112	0.53	2.00	0.69	1.20	57	60.22
Shivampet	35	39	0.08	1.11	0.39	1.95	5	6.59
Sangareddy	78	93	0.11	1.19	0.41	2.77	16	17.71
Wargal	68	117	0.38	1.72	0.59	1.84	50	52.69
DomaraPocham Pally	58	117	0.54	2.02	0.70	0.66	60	63.25
Sitharampuram	50	110	0.64	2.20	0.76	1.18	61	64.61
Kothur	44	58	0.18	1.32	0.46	2.60	15	16.96
GolkondaKhurd	45	60	0.19	1.33	0.47	1.76	16	17.99
Thummaloor	37	50	0.20	1.35	0.48	2.38	14	16.03
Ibbrahimpatnam	38	55	0.25	1.45	0.51	1.51	18	20.21
Mean values	192.6	338.83	0.36	1.68	0.57	1.26	147.23	149.84

Alpha index gives the percentage of maximum desirable circuits in the network and its value ranges from 0 to 1. Zero indicates minimum connectivity and one indicates maximum connectivity. The alpha index value for thirty locations ranges from 0.08 to 0.74. The mean value of alpha index which is 0.36 indicates a very low level of circuitry in the city network.

Beta index value also ranges from 0 to 1. Zero indicates minimum connectivity and one indicates maximum connectivity. Beta index value greater than 1 indicates a greater complexity of the network connectivity. The value of beta index in all the locations is greater than 1; this shows the complex nature of the road network in the city. Ewing (1996) suggests that the beta index value of 1.68 (mean value of beta index) is a good target for planning purposes.

Gamma index is normally expressed as a percentage of connectivity, so the mean value of gamma index which is 0.57 indicates that the network in the study area is 57% connected.

Higher Cyclomatic number and higher aggregate transportation score values result in higher degree of connectivity and efficiency.

Evaluation of locations based on the Aggregate Transportation Score (ATS)

Aggregate Transportation Score (ATS) is the addition of alpha index, beta index, gamma index and Cyclomatic number. So, ATS can be able to interpret the overall connectivity of a region or location. Higher aggregate transportation score value results in higher degree of connectivity and efficiency. Based on the ATS values obtained, this study tried to categorize and evaluate the thirty locations selected for connectivity analysis. The road network in different locations is categorized as less connected network, moderately connected network and well-connected network. The level of connectivity according to the ATS values is categorized in Table 3.

Tab. 3 - Level of connectivity based on Aggregate transportation score

Aggregate Transportation Score value	Level of connectivity
0-100	Less connected network
100-200	Moderately connected network
>200	Well-connected network

The locations selected for road network connectivity analysis are evaluated based on their ATS values and level of connectivity in each location is presented in Table 4.

Tab. 4 - Evaluation of different locations based on ATS

S.NO	Location	Notation	ATS value	Level of connectivity
1	Abids	AB	554.81	Well-connected network
2	Kukatpally	KP	109.00	Moderately connected network
3	Mehadipatnam	MP	352.82	Well-connected network
4	Dilshuknagar	DN	365.76	Well-connected network
5	Secundrabad	SC	327.84	Well-connected network
6	Panjagutta	PG	339.72	Well-connected network
7	Jeedimetla	JM	84.98	Less connected network
8	Sikenderguda	SG	83.05	Less connected network
9	Nadergul	NG	21.44	Less connected network
10	Kothapet	KT	224.76	Well-connected network
11	Ameerpet	AT	268.73	Well-connected network
12	Banjara Hills	BH	315.73	Well-connected network
13	Gandhinagar	GN	505.76	Well-connected network
14	LB Nagar	LN	163.81	Moderately connected network
15	Malkajgiri	MJ	228.89	Well-connected network
16	Hitech city	HC	112.89	Moderately connected network
17	Bhuvanagiri	BG	11.55	Less connected network
18	Ghatkesar	GS	57.93	Less connected network
19	Bhanur	BR	9.67	Less connected network
20	Moinabad	MB	19.86	Less connected network
21	RamachandraPuram	RCP	60.22	Less connected network
22	Shivampet	SP	6.59	Less connected network
23	Sangareddy	SR	17.71	Less connected network
24	Wargal	WL	52.69	Less connected network
25	DomaraPocham Pally	DPP	63.25	Less connected network
26	Sithampuram	SM	64.61	Less connected network
27	Kothur	KR	16.96	Less connected network
28	GolkondaKhurd	GK	17.99	Less connected network
29	Thummaloor	TR	16.03	Less connected network
30	Ibbrahimpatnam	IBM	20.21	Less connected network

Based on the results presented in Table 4, the locations Jeedimetla, Nadergul, Sikenderguda, Bhuvanagiri, Ghatkesar, Bhanur, Moinabad, Ramachandrapuram, Shivampet, Sangareddy, Wargal, Domarapochampally, Sithampuram, Kothur, Golkonda khurd, Thummaloor, Ibbrahimpatnam have a less connected network. The transportation planning authorities may

concentrate more on these locations to improve the connectivity of these places which increases the overall connectivity of the Hyderabad city.

CONCLUSION

Connectivity is one of the most important structural parameters to be analyzed and evaluated for an urban road network. This study shows some conclusions based on a partial analysis of the transportation problem in Hyderabad and shows a possibility of using GIS. This study majorly focused on evaluating the structural connectivity of the road network. This study attempted to analyze the connectivity at a micro scale using buffers of 5 kilometers radius at each location. This is helpful in understanding the network connectivity in each location of the city. This study described the road network connectivity with the avail of graph theory based network indices with respect to nodes and links. The study also tried to propose a methodology for the evaluation of different locations in terms of road network connectivity based on the Aggregate Transportation Score. The level of connectivity for each location is categorized as less connected, moderately connected and well-connected network. The study revealed that many locations of Hyderabad city have a less connected network. Therefore, the performance of the road network in terms of its connectivity should be improved by the transportation planning authorities. The results of the study are also useful for the urban transportation planners to understand the situation of connectivity at different locations in the city. The enhancement or improvement of road network has to be done for the locations where there is less-connected and moderately-connected network. There is a need to implement better transportation planning practices in Hyderabad city to increase the connectivity of the road network which increases the accessibility and reduces the travel time. But connectivity is certainly not just about a simple network of streets and intersections. So, the future studies may also include assessing the width of the streets, the number of people living in the locality, etc., to look into accessibility as a wider problem. The integration of GIS with urban road network connectivity analysis gave better results and is helpful in better decision making. This kind of study may be done for all the urban cities so that the planners or decision makers may estimate the level of connectivity and take necessary steps.

REFERENCES

- [1] Litman, T., 2005. Roadway connectivity: Creating more connected roadway and pathway networks. Retrieved October 25, 2005.
- [2] Ewing R., 1996. Best Development Practices: Doing the right thing and making money at the same time, Planners Press.
- [3] Handy, S, Paterson, R. & Butler, K., 2002. Can't get there from here: Planning for street connectivity. Prepared for the Planning Advisory Service of the APA.
- [4] Kumar, P., & Kumar, D., 2016. Network analysis using GIS techniques: A case study of Chandigarh city, International Journal of Science and Research, Volume 5 Issue 2, February 2016.
- [5] Vinod, R. V., Sukumar, B., & Sukumar, A., 2003. Transport Network Analysis of Kasaragod Taluk, Kerala Using GIS, Indian Cartographer
- [6] Arora, A. & Pandey, M. K, 2011. Transportation network model and network analysis of road networks, 12th Esri India User Conference 2011.
- [7] Nagne, A. D., Vibhute, A. D., & Gawali, B. W., 2013. Spatial Analysis of Transportation Network for Town Planning of Aurangabad City by using Geographic Information System, International Journal of Scientific & Engineering Research, Volume 4, Issue 7.
- [8] Nijagunappa, R., Shekhar, S., Gurugnanam, B., Raju, P.L.N. and De, P., 2007. Road Network Analysis of Dehradun City Using High Resolution Satellite Data and GIS, Journal of the Indian Society Of Remote Sensing, Vol. 35, No. 3.
- [9] Kansky, K., 1963. Structure of Transportation Networks: Relationships between Network Geometry and Regional Characteristics, Ph. D. thesis, University of Chicago, Research Paper No. 84.

- [10] Obafemi, A.A., Eludoyin, O.S., Opara, D.R., 2011. Road network assessment in Trans-Amadi, Port Harcourt in Nigeria using GIS, *International Journal of Traffic and Transportation Engineering*, 1(4): 257-264.
- [11] Patarasuk, R., 2012. Road Network Connectivity and Land-Cover Dynamics in Lop Buri Province, Thailand. *Journal of Transport Geography* 28, 111–123
- [12] Sarkar, D., 2013. Structural Analysis of Existing Road Networks of Cooch Behar District, West Bengal, India: A Transport Geographical Appraisal, *Ethiopian Journal of Environmental Studies and Management* Vol. 6 No.1
- [13] Manyazewal A.L, M.Anil & Prasad CSRK, 2014. Advanced Information System for Planning and maintenance of rural roads using GIS, *ISPRS TC VIII International Symposium on Operational Remote Sensing Applications: Opportunities, Progress and Challenges*, Hyderabad, India.

FIELD TEST ON THE COOPERATION OF NSM STRENGTHENING AND EXTERNAL TENDON RETROFITTING TECHNIQUE

Jianxi Yang, Jiaping Yu, Quansheng Sun, Hongshuai Gao and Jiawei Wang

Department of Civil Engineering, Northeast Forestry University, Harbin, 150040, China; yangjianxi@nefu.edu.cn, yujaping@hotmail.com, hrbsqs@126.com, ghsphd@126.com, wjw526@126.com

ABSTRACT

In this paper, post-tension and steel plate near-surface mounted (NSM) strengthening systems are proposed to strengthen deteriorated and cracked large box girder rigid frame bridge without altering appearance and dimension of the bridge. The reinforcement method mainly improves the bearing capacity through external prestressed tendons, and bonding steel plate can enhance the shear resistance of the bridge. The main purpose is to study the structural mechanical properties before and after the reinforcement of rigid frame bridges. Take a 540m rigid frame box girder bridge as an example. The static load test of the bridge before and after reinforcement is carried out. The deflection and strain of the middle cross section of the span are measured in the static test. A finite element analysis model was also developed and verified static loading test data. The results show that structural bearing capacity and performance of the bridge were enhanced with the post-tension and NSM strengthening systems cooperatively.

KEYWORDS

Static loading test, Finite element method, NSM strengthening, Prestressed concrete rigid frame bridge, External tendon retrofitting technique

INTRODUCTION

With the development of China's economy, growing traffic volumes pose a threat on the bearing capacity of existed traffic system, especially those in-service highway bridges designed according to the old code no longer meet the requirements of use. In the course of bridge operation, it is also found that the prestressed concrete continuous box girder bridge has the problems of beam cracking and excessive mid-span deflection [1-2].

Many researchers have studied proper repair and strengthening methods to solve the problems that occur in concrete bridges. Heeyoung et al [3] studied the structural behavior of an old 12.5m reinforced concrete T type bridge before and after using post-tension NSM strengthening systems, and verified it by finite element model calculation. The results show that the post-tensioned NSM reinforcement system can improve the bridge bearing capacity and performance of the bridge. Osman et al [4] applied fiber-reinforced polymer (FRP) composite laminates to strengthen an aging reinforced concrete T-beam bridge, the results of static load test and finite element analysis before and after reinforcement revealed that main rebar stresses were moderately reduced, concrete stresses (flexural and shear) moderately increased, and transverse live-load distribution to the beams slightly improved under service load after strengthening. Zhang [5] presents the experimental response of reinforced concrete T-beams strengthened with a

composite of prestressed steel wire ropes embedded in polyurethane cement. The experimental study on reinforcement shows that the reinforcement technique has potential as an external strengthening technique for concrete structures. Morris [6] investigated the durability of bonded and unbonded prestress tendons. Xu [7] used analytic hierarchy process (AHP) to establish the quality evaluation system of prestressed reinforcement system, and verified the evaluation system rationally in combination with practical engineering. Shen [8] presented the design and reasonable arrangement of external prestressed tendons for multi-span curved box girder bridges. Ibrahim [9] studied the bending mechanical properties of prestressed continuous concrete beams through experiments and verified them by finite element method (FEM). The ultimate bearing capacity can be improved by increasing the effective depth. In recent years, the application of bonded steel reinforced polymer (SRP) [10], carbon fiber reinforced polymer (CFRP) sheets [11-13], ultra high performance fiber reinforced concrete (UHPFRC) [14], post-tension near-surface-mounted strengthening systems and external post-tensioning reinforcement techniques has become more and more extensive and achieved good reinforcement effect in concrete beam bridge and box girder Bridge [15-20].

However, ignoring the prominent defects of bridges or lacking real judgment on the existing disease assessment will not only affect the normal use of the structure, but also pose a potential threat to the social environment and safety. In view of this, it is very important to analyze the disease of prestressed concrete continuous rigid frame bridge and select effective reinforcement measures according to the concrete conditions. Bridge reinforcement not only serve to improve the bearing capacity and stiffness of the bridge, but also need to consider factors such as aesthetic, material saving, construction difficulty.

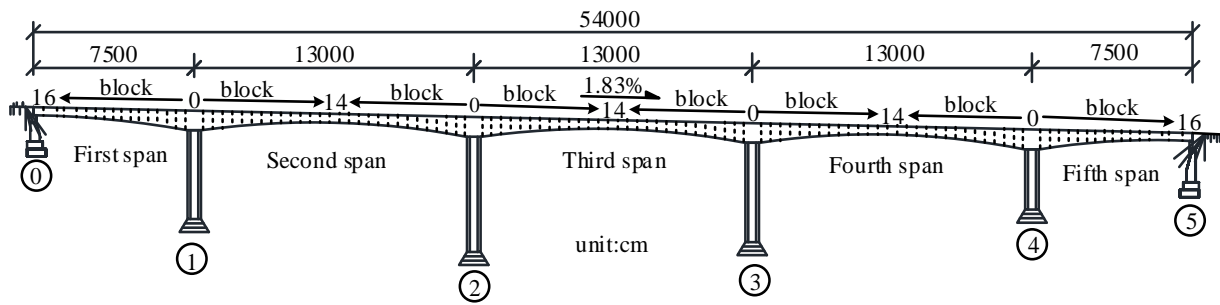
In order to study the performance of the strengthening technique, structural behaviors were compared before and after external tendon and steel plate strengthening of prestressed concrete rigid frame bridge. Furthermore, the experimental results were investigated with those of a proposed finite element analysis model. Finally, the strengthening performance was analyzed using finite element analysis.

BACKGROUND

Description of the bridge structure

The prestressed concrete bridge is a continuous segmental box girder T-shape rigid frame bridge that is located in Hegang-Dalian Highway within the Heilongjiang Province of north-east China. The bridge is 540-m long and 12-m wide. The transverse arrangement of bridge deck is 0.5m (anti-collision railing) +11.0m (lane)+0.5m (anti-collision railing). Span arrangement is 75m+3×130m+75m. The longitudinal slope and unidirectional transverse slope of bridge deck is 1.83% and 2.0%, respectively. The superstructure consists of 5-span continuous prestressed concrete rigid frame large box girder. The box girder is of single box single chamber structure, the height of segment No.0, which is on the top of the pier, is 7.0m, whereas the height of box girder is 2.5m at mid-span of the bridge. The height of longitudinal bridge box girder varies according to the equation $y=0.0026724x^{1.8}$. Bottom plate of the box girder is 5.6m in width, and the flange of the bridge is 3.2m in width. The longitudinal and transverse prestressed tendons adopts $\phi^{15.24}$ low relaxation high strength steel strand of 270 grade in accordance with the standard ASTM.A416-90a, each longitudinal prestressed tendon is composed of 15 prestressed steel strands, and the tension control force is 2932.9kN. Each transverse prestressed tendon is composed of 3 prestressed steel strands, and the tension control force is 782.1kN. The arrangement spacing of the transverse prestressed tendon is 80 cm. The substructure is composed of double-thin-walled piers, ribbed plate type abutment, and solid expanding foundation. Piers are 5.6m wide in transverse direction, and 1.2m wide in longitudinal direction with spacing of 3.6m. The heights of

the piers are 35m, 45m and 24m, respectively. The design load of bridge reinforcement is highway grade I [21] (the original design load is vehicle super-20, trailer-120). The bridge was opened to traffic in 2006 and strengthened in 2016. Figure 1(a) shows the elevation drawing of the bridge structure, Figure 1(b) shows the overall perspective of the strengthening bridge.



(a)



(b)

Fig.1 – Details of the strengthening bridge: (a) elevation drawing; (b) overall perspective

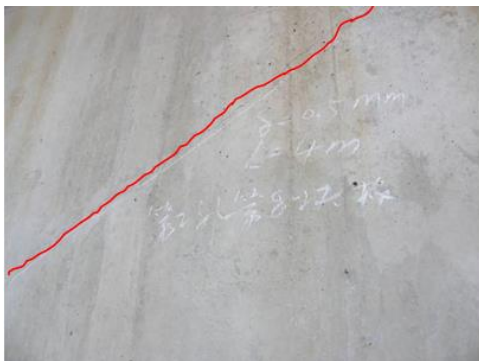
Bridge diseases

The rigid frame continuous box girder bridge in this study was first open to traffic in 2006. However, after as little as 6 years of operation, the degradation of material properties and load bearing capacity of bridge appeared. During routine inspection in 2012, 2013 and 2015, cracks were observed on the top slab, web and bottom slab, more severe on the exterior surfaces than the interior of box girder. Length, width and number of cracks were growing as time goes on. Most of the cracks were between 0.15mm ~ 0.4mm in width and 0.3m ~ 7m in length. According to the codes and specifications that prestressed concrete beams are not allowed to have cross-sectional cracks, and the allowable width of longitudinal cracks is 0.2mm. The width of some longitudinal cracks on the box girder exceeds the specified value.

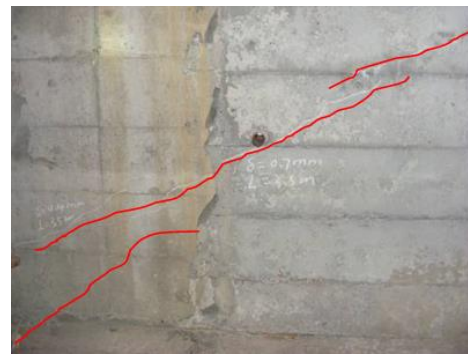
In the routine inspection of the bridge in 2012, bridge detection results show that there was a large number of oblique cracks in the outside of the web of box girder near the fulcrum of the second span and closure segment (block 6-14) of the third span. The crack width is generally between 0.2~0.5mm and roughly distributed in the direction of $20^{\circ} \sim 45^{\circ}$, and the maximum crack width is 0.5 mm. These cracks show the characteristics of obvious stress cracking of the principal tensile stress. There are about 21 oblique cracks in the outside of the web of box girder, the total length of the oblique cracks is about 70.7m, the total length of the left oblique cracks is 29.5m, and

the total length of the right oblique cracks is 41.2m. The cracks are roughly distributed in the 130m main span.

Routine inspection of the bridge was conducted again in 2013 and 2015, respectively. Cracks distribution of box girder was similar compared to 2012 inspection. However, cracks on the web gradually developed into transverse cracks at the chamfering angle of the top slab of box girder. As a result, there were 156 oblique cracks detected on the web of the box girder, the crack total length was 38.6m, among which 72 cracks on the right side with a total length of 19.3m and 84 cracks on the left side with a total length of 19.3m. There were about 38 cracks on the exterior surface of the web with a total length of about 11.95m, among which 11 cracks on the left side with a total length of 32.9m, and 27 cracks on the right side with a total length of 86.6m. Crack distribution on the web of the box girder is shown in Figure 2. In the following figures, L represents the length of the crack, δ represents the width of the crack, and α indicates the angle between the crack and the longitudinal bridge direction.



(a) No. 8 block exterior surface oblique crack ($L=4\text{m}$ $\delta=0.5\text{mm}$ $\alpha=45^\circ$)



(b) No. 8 block interior surface oblique crack ($L=8\text{m}$ $\delta=0.7\text{mm}$ $\alpha=35^\circ$)



(c) No. 10 block right side interior surface oblique crack ($L=9\text{m}$ $\delta=0.5\text{mm}$ $\alpha=35^\circ$)



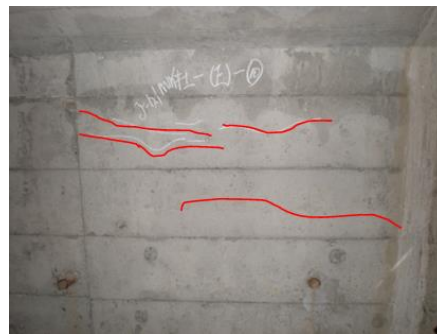
(d) No. 11 block left side interior surface crack ($L=3.4\text{m}$ $\delta=0.15\text{mm}$ $\alpha=30^\circ$)



(e) No. 13 block right side interior surface crack (L=6.7m $\delta=0.15\text{mm}$ $\alpha=45^\circ$)



(f) No. 10 block left side interior surface crack (L=2.9m $\delta=0.10\text{mm}$ $\alpha=45^\circ$)



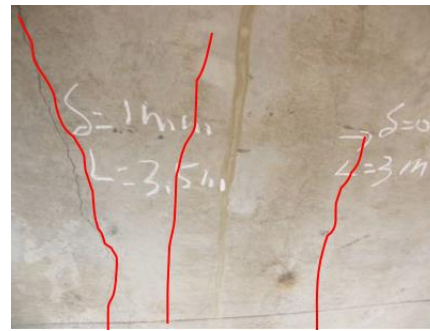
(g) No. 14 block right side interior surface crack (L=2.4m $\delta=0.10\text{mm}$ $\alpha=15^\circ$)

Fig.2 – Crack distribution on the web of box girder of the second span

In 2013 inspection, 5 longitudinal cracks were observed at the exterior surface of box girder bottom slab of closure segment of the second span, the length of cracks were ranging from 2m to 7m and the width of cracks were ranging from 0.6mm to 4mm. In 2015 inspection, it was found that there were 9 longitudinal cracks on the bottom slab of the closure segment. There were 3 longitudinal cracks on the bottom slab of closure segment of the third span and 7 longitudinal cracks in closure segment of the fourth span, whereas bottom slab of second span was the most severe, the maximum width of the longitudinal crack is up to 4 mm and crack bulge deformation is about 3 mm. After chipping away loose concrete around the crack, hollow section was found and corrugate pipe was slightly damaged. Cracks on the bottom slab of the box girder of closure segment of second span and third span are shown in Figure 3.



(a) bottom slab cracks of second span
(L=20.5m δ=0.6mm)



(b) bottom slab cracks of third span
(L=8.5m δ=0.7mm)



(c) longitudinal bottom crack of second span (L=0.7m δ=4mm)



(d) Longitudinal crack hollow section of second span



(e) Longitudinal crack hollow section of second span



(f) longitudinal crack corrugate pipe deterioration of second span

Fig. 3– Cracks on the bottom slab of the box girder of closure segment

Moreover, there is a vertical crack on interior diaphragm of box girder end of the first span. The width and length of the crack are 0.25mm and 200cm, respectively, as shown in Figure 4.



Fig. 4 – Crack on interior diaphragm of box girder end of the first span
($L=2m$ $\delta=0.25mm$)

The number, length and width of cracks increase with the number of years of operation as shown in Figure 5. From 2012 to 2013, the width of cracks on the web of box girder increased by 24.77%, the number of cracks increased by 103, and the length increased by 229.37m. From 2013 to 2015, the width of cracks increased by 11.26%, the number of cracks increased by 60, and the length increased by 163.03m. The main causes of the development of the bridge crack in the period from 2012 to 2015 is that the increase of the heavy-load vehicle exceeds the design load capacity of the bridge, leading to the main tensile stress generated by the live load exceeding the design value, and the box girder generates the oblique crack disease.

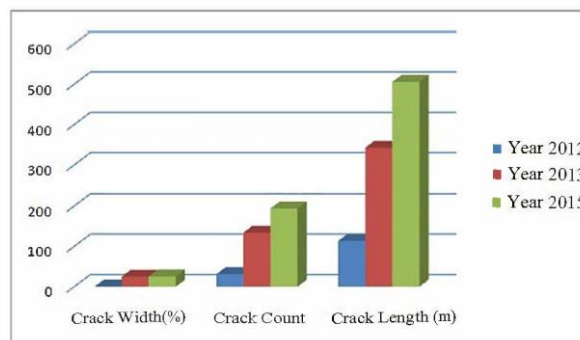


Fig. 5 – Comparative Diagram of cracks in Box girder in different Detection years

External Tendon and Steel Plate Strengthening

The external tendons were stretched at both ends. External prestressing tendons were cross-anchored at the top of the main pier, and the cast-in-place anchor block was used for anchoring at the box girder end. The number of external prestress tendons is determined by reducing the web shear force and making the main tensile stress of the web of the box girder meet the code, and increasing the bending capacity of the normal section of the span and the compressive stress reserve at the bottom of the beam. Eight bundles of 17 ϕ^s 15.24 prestressed steel strands are used in each span, and the tensile control stress is 930MPa, which is 50% of the standard strength. The detailed arrangement of external prestressed tendons is shown in Figure 6.

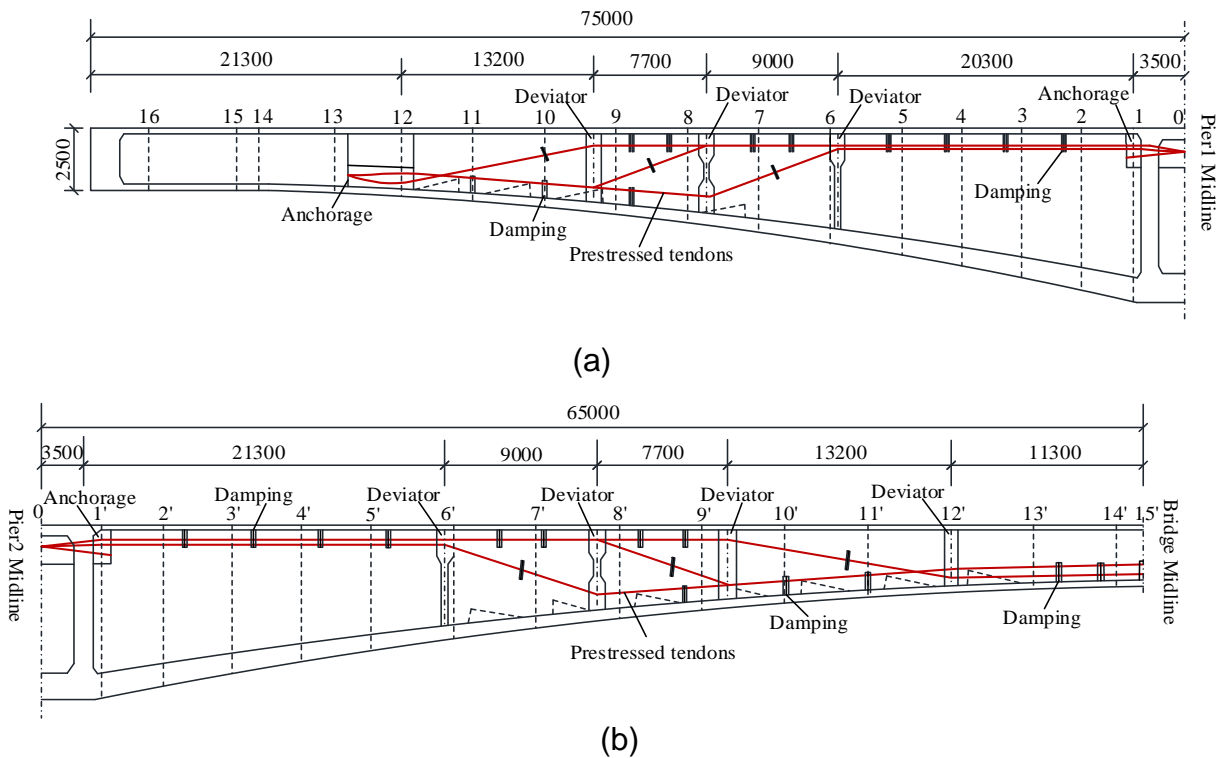
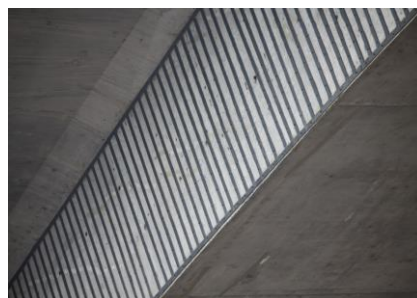


Fig. 6 – External prestressing strands arrangements for: (a) side span; (b) middle span (unit: mm)

The vertical steel strip is pasted on both sides of the web to strengthen the oblique section of the box girder. The reinforcement range of the inside of the web of the box girder is from 6 to 14 girder segments, and that of the outer side of the web is from NO.6 to NO.10 block of the middle span. The steel reinforcement of the top plate of box girder is the non-thickened area of the web. The bending capacity of the bottom plate is increased in the range of 15 m of the mid-span closure section by the use of an adhesive steel strip. The penetration anchoring is carried out by anchoring bolt in the range where is no bottom plate prestress in the center of web and bottom plate. The thickness and width of the steel plate are 6mm and 60mm, respectively. The length of the steel plate depends on the disease distribution area. The steel plate is made of Q235 steel. The thickness of zinc-rich primer is 70 μ m, and the epoxy asphalt paint consists of intermediate layer and topcoat, with a total thickness of 200 μ m. Steel plate reinforcement of box girder is shown in Figure 7.



(a)



(b)



(c)

(d)

Fig.7 – Steel plate reinforcement of box girder: (a) inner wall of web (b) outer wall of web (c) and (d) bottom plate

EXPERIMENTAL PROGRAM

The design load grade of deteriorated rigid frame continuous box girder bridge was vehicle-20, trailer-100 according to Chinese design code JTG 021-1985[22]. The lane load is composed of the uniform load of 10.5kN/m and the concentrated load of 360kN, which is similar to AASHTO HS15 loading in the American bridge design code[23]. Static loading tests were performed to obtain structural behaviour of the bridge before and after strengthening (Figure 8). The main objectives of the static loading test were to test the following:

1. Strain in the static load test in the vicinity of the supporting point;
2. Strain of the most unfavourable section of side span and middle span under static load test;
3. Deflection of the most unfavourable section of side span and middle span under static load test.



a)



b)

Fig.8 – Illustration of field static load test (a) eccentric loading test before or after strengthening; (b) centric loading test before or after strengthening

Loading test truck arrangement

A total of 16 triaxial trucks were used in static loading test. Trucks #1~#8 were used before strengthening and trucks #9~#16 were used after strengthening. The sum of axle load and axle load of truck is shown in Table 1.

Tab. 1 - Characteristics of the loading truck (kN)

Truck	Front axle	Middle axle	Rear axle	Total axle load
#1	73.1	148.1	144.1	365.3
#2	73.2	147.5	145.5	366.2
#3	73.9	148.8	146.8	369.4
#4	73.4	147.8	145.8	367.0
#5	73.5	145.0	149.0	367.5
#6	73.5	149.1	145.1	367.7
#7	74.1	148.2	148.2	370.5
#8	73.1	147.3	145.3	365.7
#9	74.1	147.1	149.1	370.3
#10	73.8	149.7	145.7	369.2
#11	74.4	149.7	147.7	371.8
#12	73.3	147.6	145.6	366.4
#13	73.7	148.3	146.3	368.3
#14	74.2	148.3	148.3	370.8
#15	73.9	147.9	147.9	369.7
#16	73.6	148.2	146.2	368.0

Centric and eccentric loading were performed on mid-span cross-sections and eccentric loading was performed on pier cross-section, maximum bending moments were measured for each load cases before and after strengthening. Static Loading Schemes are shown in Table 2. Eccentric and centric loading location drawing plans are shown in Figure 9.

Tab. 2 - Static Loading Scheme

Case No.	Location	Loading condition	Deflection	Strain Gauges
1	midspan of first span	centric	√	√
2	midspan of first span	eccentric	√	√
3	midspan of second span	centric	√	√
4	midspan of second span	eccentric	√	√
5	pier 2	eccentric	---	√
6	midspan of third span	centric	√	√
7	midspan of third span	eccentric	√	√

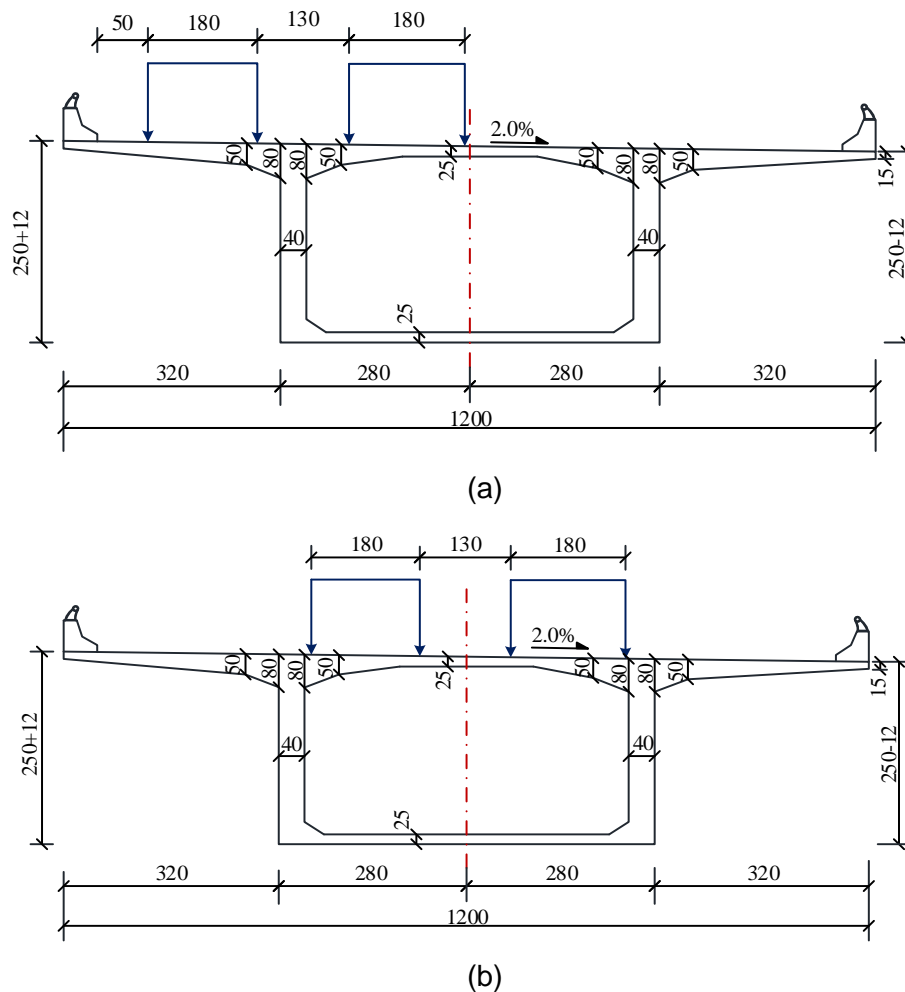


Fig. 9 –Lateral arrangement of static load test load (a) eccentric loading; (b) centric loading (unit: cm)

Deflection measuring point and strain sensor layout

The bridge detection system consists of deflection measuring point and strain sensors. Deflection measuring point and strain sensors were strictly controlled at the same locations before and after strengthening. Deflection measuring points were placed at the middle of the span, the measuring point number is d1, d2 and d3. The deflection is measured by precision level. Strain measuring points of midspan were placed on the interior surface of the top slab, web and bottom slab of the box girder, the measuring point number is s1~s11. Strain measuring points of pier cross-section were placed only on the inner wall of top slab and web of box girder, the measuring point number is ps1~ps7. The strain sensors are all vibrating wire strain meters. Deflection measuring point and strain sensor layout of box girder before and after the strengthening are shown in Figure10.

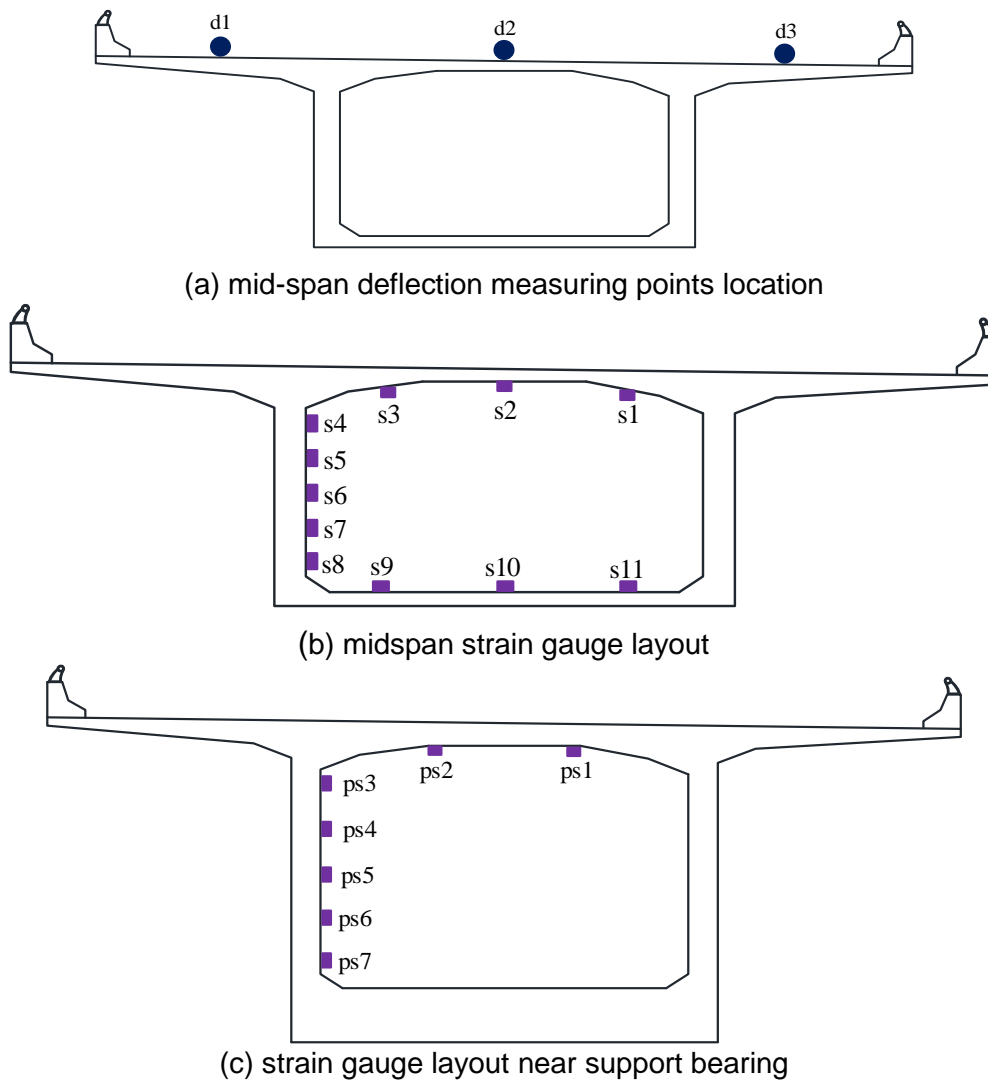


Fig. 10 – Deflection measuring point and strain sensor layout of box girder

ESTABLISHMENT OF FINITE ELEMENT MODEL

The Midas Civil software is used to establish the spatial finite element model of bridge before and after reinforcement, as shown in Figure 11. The box girder and pier are simulated by beam element. The prestressed steel wire strand bundle number of top plate, bottom plate and the web of box girder of the bridge is 229,100 and 64, respectively. Eight bundles of 17 $\varphi^{15.24}$ prestressed steel strands are used in each span of the bridge after reinforcement. The prestressed steel wire strand bundles are simulated by tension frame unit. There are 290 units in the bridge finite element model. The connection between the top of the pier and the box girder is rigid connection, and the bottom of the pier is consolidation connection. The end of the bridge constrains vertical displacement and lateral displacement. The load of the vehicle of static load test is simplified into a concentrated force calculation, the actual bearing capacity of the reinforced bridge is obtained by comparing the calculated value with the measured value.

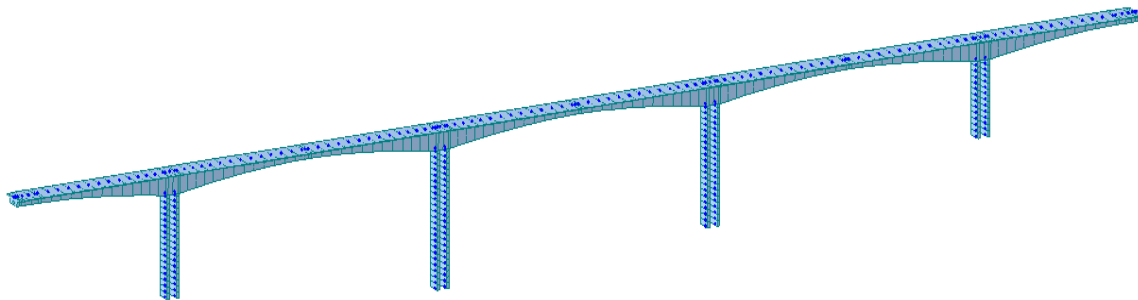
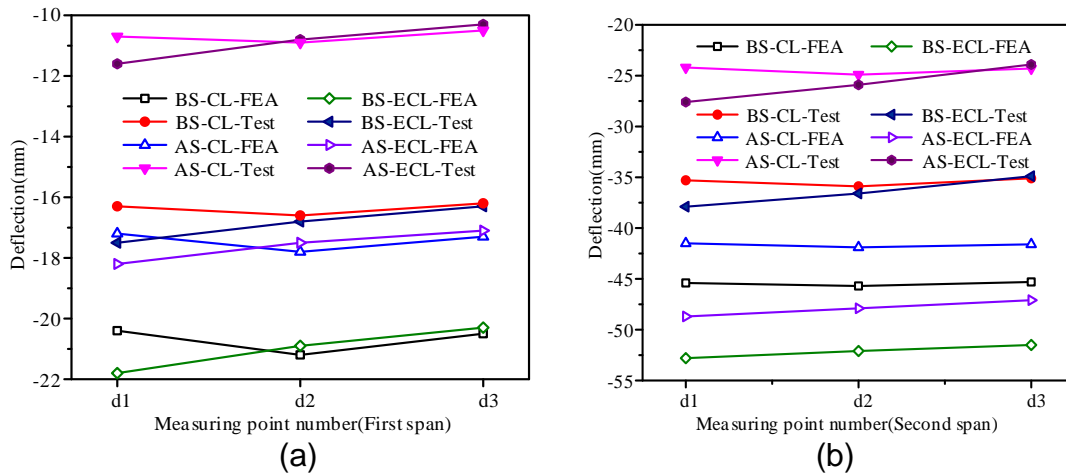


Fig. 11- Spatial finite element model of bridge

RESULTS & DISCUSSION

Deflection

The deflection value, as the key control parameter of the static load test of the bridge, reflects the overall stiffness of the bridge structure. The finite element model calculation value and test value for load test of deflection before and after strengthening are shown in Figure 12. In the following figures, BS and AS indicate before and after strengthening, CL and ECL indicate centric and eccentric load, FEA and Test indicates finite element analysis and static load test result, respectively.



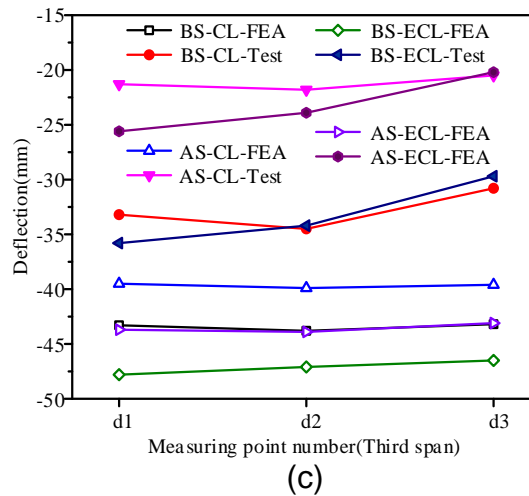


Fig.12– Calculated and Measured vertical displacement curve for (a) First span; (b) Second span; and (c) Third span

After bridge reinforcement, as shown in Figure 12, under the action of load test under each working condition, the measured deflection values of each measuring point are less than the theoretical values. For the first span, the deflection coefficient of correction is between 0.60 and 0.64, the coefficient of correction of the bridge is increased by 22.7% after reinforcement, the bearing capacity has increased by 18.2%. For the second span, the deflection coefficient of correction is between 0.51 and 0.59, the coefficient of correction of the bridge is increased by 23.8% after reinforcement, the bearing capacity has increased by 17.5%. For the third span, the deflection coefficient of correction is between 0.47 and 0.59, the coefficient of correction of the bridge is increased by 27.0% after reinforcement, the bearing capacity increased by 19.7%. The results show that external prestressing strengthening can significantly improve the performance of the structure. However, due to the loss of prestress caused by reinforcement construction, the actual deflection improvement value is less than the theoretical deflection improvement value.

Measured deflection values of the bridge after reinforcement are all smaller than the values of the bridge before reinforcement. The maximum displacement after the strengthening decreased to 27.6mm, compared to 37.9mm before strengthening. After strengthening, the displacement of all spans decreased. The strengthening effect of the maximum displacement of the static loading test was improved by 27%.

Strain

Strain is another key data that reflects the stress of bridge. Measured strain data under static loading before and after strengthening is shown in Figure13 and Figure14.

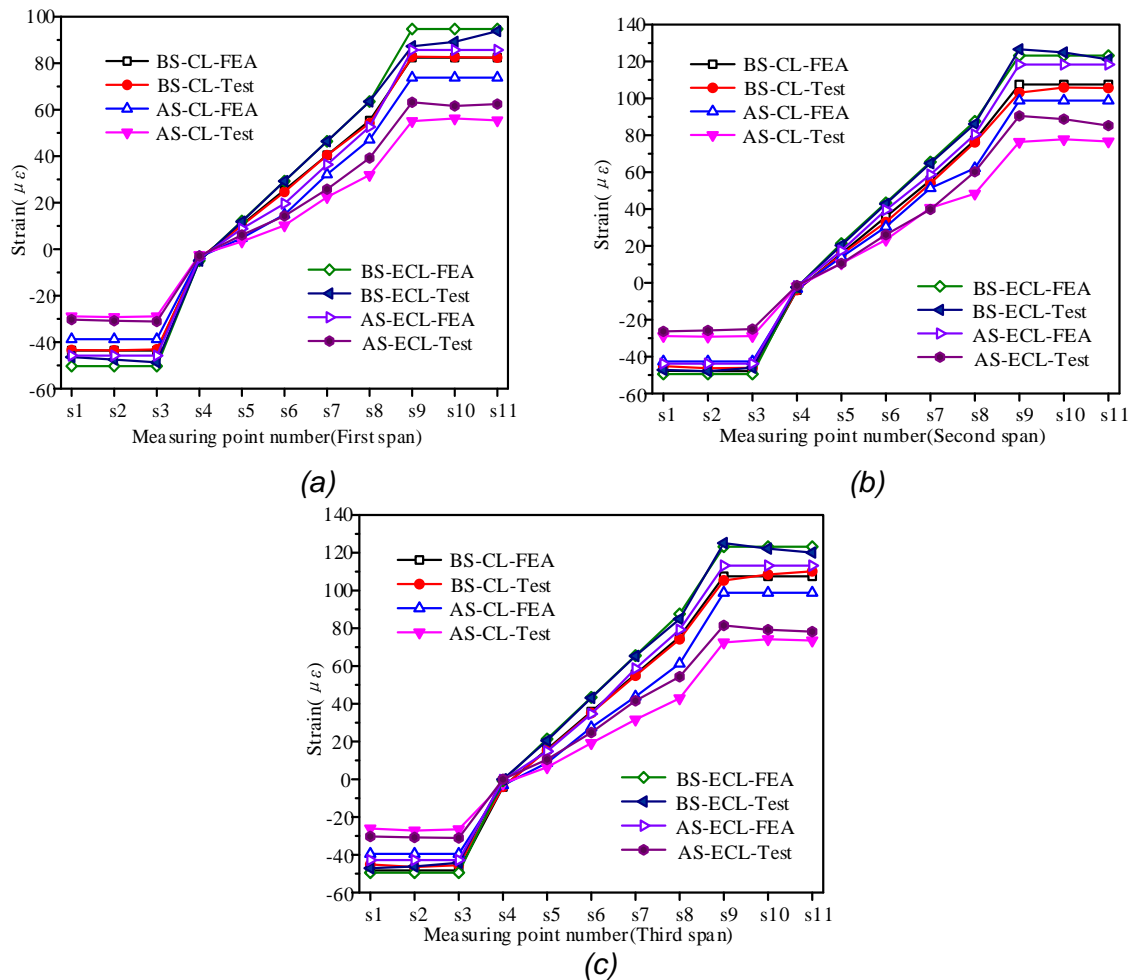


Fig. 13 – Measured strain data under static loading tests

After bridge reinforcement, as shown in Figure 13, the measured strain values of each measuring point are less than the theoretical values of finite element model. The measured strain values of each load cases of the first span all show improvement after external prestressing strengthening. For the first span, the strain coefficient of correction is between 0.66 and 0.75, which indicated stiffness improvement of the bridge structure. The average increment of load carrying capacity and coefficient of correction are 28% and 27%, respectively. For the second span, the strain coefficient of correction is between 0.57 and 0.79. The average increment of load carrying capacity and coefficient of correction are 26% and 27%, respectively. For the third span, the strain coefficient of correction is between 0.57 and 0.76. The average increment on strain and coefficient of correction of midspan centric loading are all 27%, and the average increment on strain and coefficient of correction of midspan eccentric loading are 23% and 24%, respectively.

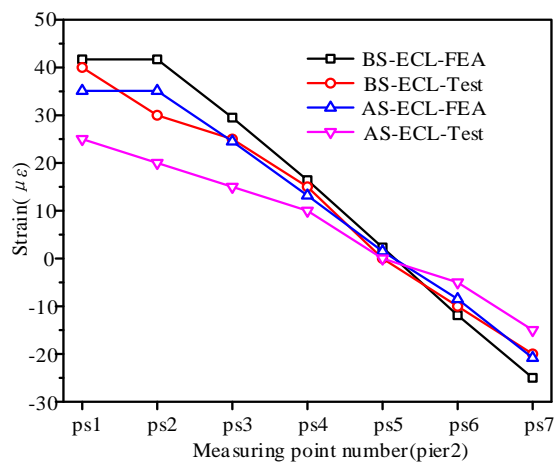


Fig. 14 – Measured strain data under static loading tests of pier 2

At pier 2, as shown in Figure 14, the measured strain values of each measuring point are less than the theoretical values of finite element model. The bearing capacity increased by 15%, and coefficient of correction increased by 18%. After the strengthening of the deteriorated bridge, the measured strain values under static loading tests at each span are all less than the values of the bridge before strengthening. The bridge structure showed significant improvement entirely on stiffness as well as bearing capacity. Therefore, the external prestressing reinforcement method not only can effectively improve the structural performance of the bridge, but also can improve the strength and the safety reserve of the bridge.

CONCLUSION

The deteriorated rigid frame bridge is reinforced by post-tension and steel plate NSM strengthening method, through the comparison and analysis of the measured data of static load test and the calculated data of finite element model, it can be seen that both deflection and strain values of control section decreased after bridge strengthening compared with the bridge before reinforcement. The bearing capacity, crack resistance and deflection of the rigid frame bridge after reinforcement meet the design requirements. And the bearing capacity, stiffness and safety reserve of the bridge can be improved after reinforcement. The proposed strengthening method has been proved to be effective. It is suggested that low relaxation prestressed steel wire bundles should be selected when strengthening continuous rigid frame bridges. The prestressed steel wire bundle adopts two-end stretching mode and the super-tension can effectively reduce the loss of the prestress. For the crack disease of box girder of continuous rigid frame bridge, it is effective to repair the crack of box girder strengthened with bonded steel plate.

REFERENCES

- [1] Jose A. Instrumentation system for post-tensioned segmental boxgirder bridges. Master dissertation, Austin: University of Texas, 1991
- [2] Vladimir K, Zdenek P, Milos Z, and Alena K. Box girder bridge deflections, (2006). ACI concrete international, Vol. 28 (1): 55–63
- [3] H. Lee, W. Jung, W. Chung, (2018). Field test of an old RC bridge before and after NSM strengthening. Composite Structures; Vol. 202:793-801
- [4] H. Osman, A. Sreenivas, K. Jonathan, (2001). Application of FRP laminates for strengthening of a reinforced-concrete T-beam bridge structure. Composite Structures 52:453-466.

- [5] Zhang, Kexin , and Q. Sun, (2017). "Experimental Study of Reinforced Concrete T-Beams Strengthened with a Composite of Prestressed Steel Wire Ropes Embedded in Polyurethane Cement (PSWR–PUC)." *International Journal of Civil Engineering*. 16:1109–1123.
- [6] Morris. S, (1978). Survey of the durability performance of posttensioning tendons. *ACI J*, vol. 75(10):501–510.
- [7] J. L. Xu, Z. L. Yi, J. L. Yang, (2013). A Study on the Quality Assessment System of External Prestressing Reinforcement Technology, *Applied Mechanics and Materials*, vol. (351-352): 1347-1353.
- [8] Y. Shen, T.Y. Song, G.P. Li, 2015. Advances of external prestressing tendons in multi-span curved box-girder bridges. *Multi-Span Large Bridges – Proceedings of the International Conference on Multi-Span Large Bridges*, 1255-1262.
- [9] A. M. Ibrahim, (2010). Parametric study of continuous concrete beam Prestressed with external tendon. *Jordan Journal of Civil Engineering*, vol. (4)3:211-221.
- [10] Lopez, A. , Galati, N. , Alkhrdaji, T. , & Nanni, A., 2007. Strengthening of a reinforced concrete bridge with externally bonded steel reinforced polymer (srp). *Composites Part B (Engineering)*, vol. 38(4), 429-436.
- [11] Oh, H. , Sim, J. , & Meyer, C., 2003. Experimental assessment of bridge deck panels strengthened with carbon fiber sheets. *Composites Part B Engineering*, vol. 34(6), 527-538.
- [12] Lee H Y , Jung W T , Chung W,(2017).Flexural strengthening of reinforced concrete beams with pre-stressed near surface mounted CFRP systems. *Composite Structures*, vol. 163:1-12
- [13] Fathelbab, F. A. , Ramadan, M. S. , & Al-Tantawy, A. . (2014). Strengthening of RC bridge slabs using CFRP sheets. *Alexandria Engineering Journal*, 53(4), 843-854.
- [14] Maléna Bastien-Masse, & Eugen Brühwiler, 2013. Concrete bridge deck slabs strengthened with uhpfrc. *labse Symposium Report*, vol. 99(22).
- [15] Lee H, Jung W T, Chung W, (2017). Post-tension near-surface-mounted strengthening systems of full-scale PSC girders. *Construction and Building Materials*, vol. 151: 71-82.
- [16] Khudeira, S. . (2010). Strengthening of deteriorated concrete bridge girders using an external posttensioning system. *Practice Periodical on Structural Design and Construction*, 15(4), 242-247.
- [17] Parke G A , Disney P , Ahmadikashani K, (2005).Strengthening box-girder bridges using external post-tensioning. *Thomas Telford*:97-104.
- [18] Dunker, K. F. . (1985). Strengthening of simple span composite bridges by post-tensioning.
- [19] Van Lier, J. , & Pronk, M. . (2013). Reinforcing concrete box girder bridges with external post-tensioning and steel. *IABSE Symposium Report*, 99(22), 670-677.
- [20] Taljsten, B. , & Nordin, H. . (2007). Concrete beams strengthened with external prestressing using external tendons and near-surface-mounted reinforcement (nsmr). *Journal of Quantitative Spectroscopy & Radiative Transfer*.
- [21] JTG D60-2004 General Code for Design OF Highway Bridges and Culverts. P.R. China, Ministry of Communications, 2004.
- [22] JTJ 021-1989. General Code for Design of Highway Bridges and Culverts, P.R. China, Ministry of Communications,1989.
- [23] AASHTO LRFD bridge design specifications, third edition. Washington, DC: American Association of State Highway and Transportation Officials; 2012.

SELF FIBER COMPACTING CONCRETE (SFCC) PROPERTIES INCORPORATED WITH SILICA FUME AND FIBER

Hakas Prayuda, Fanny Monika, Martyana Dwi Cahyati and Fadillawaty Saleh

*Universitas Muhammadiyah Yogyakarta, Faculty of Engineering, Department of Civil Engineering, Tamantirto Kasihan Bantul Yogyakarta, Indonesia;
hakasprayuda@umy.ac.id; fanny.monika.2007@ft.umy.ac.id;
martyana.dc@ft.umy.ac.id; dilla_vu@yahoo.com*

ABSTRACT

SFCC is one of the self-compacting concrete innovations. With the presence of fiber, this concrete is not only famous for its own compaction process but also has good tensile strength and good ductility when compared to normal Self Compacting Concrete (SCC). Taking into account the environmental and economic factors of the use of cement as a major component in the manufacture of SFCC, this research is innovating by reducing the use of cement and replacing it with the use of silica fume. The silica fume variations used in this study include 5%, 10%, and 15% with the use of 1% nylon fiber. Fresh properties testing including slump flow, T50, V - Funnel, and L - Box for silica fume variations were conducted in this study. Not only that, compressive strength, tensile strength and flexural strength testing are carried out to study the mechanical properties of the SHCC against silica fume variations. The results show that the use of silica fume variations will affect the fresh properties and mechanical properties of the SFCC concrete. The use of 5% silica fume in SFCC concrete is the optimum use to get the optimum compressive strength.

KEYWORDS

Self-fiber Compacting Concrete, Silica fume, Compressive strength, Tensile strength, Flexural strength, Fresh properties

INTRODUCTION

In the construction of concrete structures, the compaction process is generally carried out after the concrete is put into the formwork. However, when casting is carried out on a large scale, it will have an impact on the increasingly difficult process of vibrating work. Therefore, some researchers conducted studies to create concrete technology that is able to overcome this problem known as Self Compacting Concrete. In the mid-1980, Self-compacting Concrete (SCC) was first developed in Japan [1-2]. SCC is a well-known concrete with the ability to compact itself without the help of the vibrating process. SCC is able to flow under its own weight, allowing it to fill in the formwork and reach the highest density [3]. As for some of the other benefits of using SCC including reducing the cost of compaction work, labour time and labour costs, reducing permeability and increasing durability [4-6]. Therefore by considering its benefits, SCC is commonly applied in various infrastructures such as buildings [7], dams [8] and pre-stressed beam girders [9].

Previous researchers have developed SCC with creating the innovations that had reach at SCC's characteristics that are not only able to compacted itself but also have high tensile strength and ductility. For obtaining better tensile performance, commonly previous researchers have added a fiber called self fiber compacting concrete (SFCC). The several types of fiber that have been used by previous researchers such as polypropylene fibers, steel fibers [10], nylon fiber and

zeolite [11] and waste plastic fibers [12, 13]. According to the previous researchers, using fiber does not only effect on increasing the tensile performance but also the flexural performance that triggers for producing the high ductility.

Several studies have perfected the characteristics of SCC to become SFCC. It is very beneficial in the concrete tensile strength performance, but there are some things that need to be considered, namely by considering environmental factors and cost of materials. The use of cement as a main component of SFCC can increase global warming. This is due to the fact that the manufacture of cement produces CO₂ gas which can trigger global warming. By considering it, this research tries to innovate by reducing cement and replacing it by using silica fume variations. Based on previous research, it was revealed that the use of silica fume can improve mechanical properties in concrete. This is due to the presence of CSH. The silica fume reacts with the cement paste to the additional strong form Calcium Silicate Hydrate (CSH) providing higher strength. Silica fume reduces bleeding and enhances the cement paste bond to the aggregates. Thanks to its pozzolanic effect (reaction with Ca(OH)₂), and therefore to the strength improvement, silica fume can be used to reduce the cement content of the mix. In addition to the cost-saving benefits, this will reduce the total heat of hydration and can improve the performances of the concrete in terms of chemical resistance.

Some of the previous studies only examined the use of silica fume in SCC but for the use of silica fume in SFCC is something that needs to be developed. Therefore, this study examined the effect of using silica fume variations on the SFCC with variations of 5%, 10%, 15%. The purpose of this study was to determine the fresh properties and mechanical properties of the SFCC against superplasticizer variations. Not only that, to get the right optimum percentage used in SHCC concrete.

METHODS

Material properties

The material used in making SCC consists of sand, gravel, cement, fiber, water and silica fume. Type I cement was used in this study. As for some preliminary tests conducted to determine the characteristics of sand and gravel including testing water content, specific gravity, absorption, mass density, mud content and roughness content. Specific gravity results for sand and gravel are 2.76 and 2.58. The size of coarse aggregate granules in this study was used at 19 mm. The results of sand grain gradation analysis can be seen in Figure 1. The quality of sand and gravel aggregates can be seen in Table 1. While the type of fiber used in this study is nylon fiber which cut per 5 cm that can be seen in Figure 2. Nylon fiber is used as much as 1% of the weight of cement. Silica fume is a type of pozzolan or material containing silica and alumina compounds, this study uses silica fume from PT. Sika Indonesia. Superplasticizer is an added ingredient that works to reduce water usage. This research uses a superplasticizer in the form of Sikament LN from PT. Sika Indonesia.

Tab. 1 - Specification of fine aggregate and coarse aggregate

Test Item	Unit	Fines Aggregate	Coarse Aggregate
Water Content	%	1.97	0.71
Specific Gravity	-	2.76	2.58
Absorption	%	2.81	0.75
Mass Density	gr/cm ³	1.72	1.55
Mud Content	%	4.01	0.91
Roughness content	%	-	32.87



Fig. 1 - Gradation of fine aggregate



Fig. 2 - Nylon fiber

Mix design

The mix design used in this study uses a 30 MPa compressive strength plan with a f_{as} value of 0.23 and refers to research by Aggarwal et al. (2008) [14]. The percentage of silica fume used is 0%, 5%, 10%, and 15% with 1% nylon fiber percentage. Table 2 presents the concrete design mix of Self-Compacting Concrete (SCC) per m^3 . Material mixing method is carried out by the stages of mixing fine materials such as cement, silica fume, and fine aggregate into the mixer and followed by the addition of coarse aggregate then stirring evenly. Water and superplasticizer are added gradually until the mixture is homogeneous. Nylon fiber is added little by little, each addition of fiber to the mixture, the mixer is rotated 1 to 2 times to flatten the nylon fiber. Mixing that is the same when given fiber will cause clumping of the fiber to the mixture.

Tab. 2 - Mix design of SFCC per m^3

Materials (Kg)	0% SF	5% SF	10% SF	15% SF
Cement	485.00	460.75	436.5	412.25
Silica Fume	-	24.25	48.5	72.75
Fines Aggregate	600	600	600	600
Coarse Aggregate	561	561	561	561
Superplasticizer	7.275	7.275	7.275	7.275
Nylon Fiber	-	4.85	4.85	4.85
Water	135	135	135	135

Fresh properties test

To determine the concrete characteristics of Self-Compacting Concrete (SCC), fresh properties need to be examined to obtain the value of filling ability, passing ability, and flowability with the slump flow, T50, L-box, and V-funnel. T50 test was conducted to determine the flowability and flow rate at SCC without any obstructions. This test uses a cone and T50 cm. V-funnel testing is performed to determine the value of viscosity and filling ability in self-compacting concrete. The tool used in this test is a V-shaped funnel, at the bottom there is a door that can be opened and closed. The v-funnel test results from self fiber compacting concrete (SFCC) with the addition of silica fume variation of 0%, 5%, 10%, and 15% in a row that is 4.48 seconds, 9.06 seconds, 10.08 seconds, and 11.15 seconds. The V-funnel test results can be seen in Figure 3(a). The criterion in the concrete mixture that flows out of the funnel has duration of 6 -12 seconds [15]. L-box testing is carried out to determine the passing ability of self-compacting concrete in flowing through tight holes including the space between reinforcing steel reinforcement and other obstructions without segregation. L-box test results can be seen in Figure 3(b). The criterion used is the ratio h_2/h_1 which is between 0.8 - 1. Slump flow testing is carried out to determine the flowability which is the main examination that the consistency of fresh concrete meets the specifications. Slump flow testing requirements on self-fiber compacting concrete (SFCC), which is between 550 - 850 mm.

Hardened properties test

Concrete compressive strength testing is performed on concrete with ages 7, 14, and 28 days using a compressive machine test. Compressive strength testing is done by applying axial load pressure to the cylinder until a failure occurs [16]. How to calculate the compressive strength of concrete can be seen in Equation 1. P represents the maximum load (kN) and A represents the section area (mm²).

$$\text{Compressive strength} = \frac{P}{A} \tag{1}$$

Split tensile testing is carried out at ages 7, 14, and 28 days. Test object placement on a tensile testing machine using a steel plate that functions to distribute the compressive load to all parts of a concrete blanket. Concrete tensile strength testing is done by applying compressive force to the blanket or the diameter of the concrete cylinder which causes tensile collapse [17]. How to calculate the concrete tensile strength can be seen in Equation 2. P represents the maximum load (kN) and D represents the diameter of specimen (mm) and L is the length of specimen (mm).

$$\text{Tensile strength} = \frac{2P}{\pi LD} \tag{2}$$

Flexural strength testing is performed on concrete with ages 7, 14 and 28 days. In this test uses a point loading in the middle of the specimens [18]. The specimen dimension is 150x150x600 mm. The displacement was measured in the middle of specimens.

RESULTS

Fresh properties characteristic

Figure 3(a) shows the results of the SFCC v-funnel test with silica fume variation of 0%, 5%, 10%, and 15%. From the figure below it can be concluded that the higher the silica fume level, the higher the viscosity level of the mixture. Figure 3(b) shows the results of the L-box test with successive results namely 0.97; 0.93; 0.91, and 0.85. The figure shows that the less of using the silica fume level will effect on the better the ability of concrete for filling space.

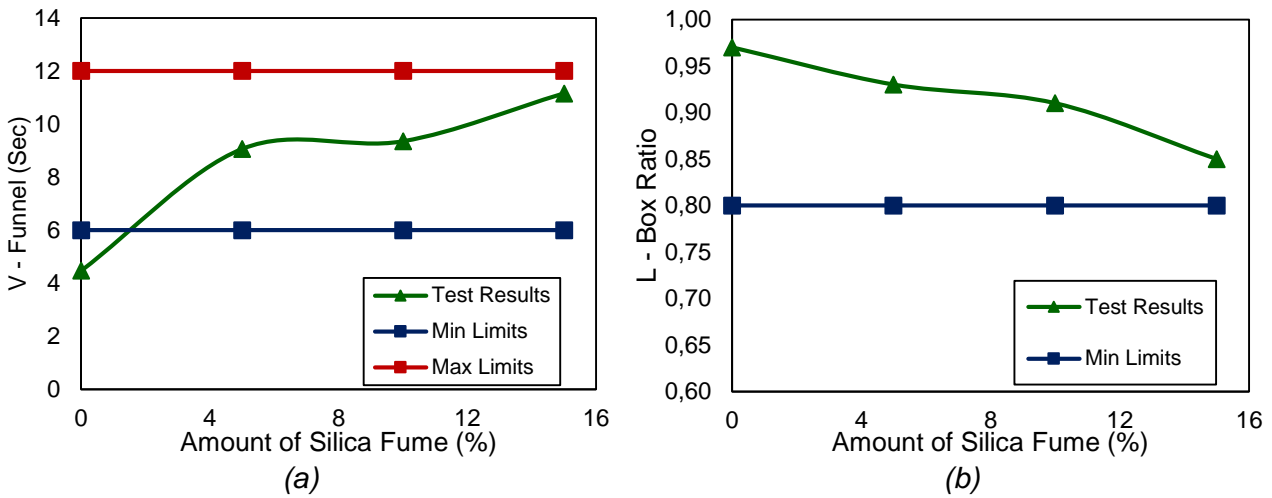


Fig. 3 – (a) V-funnel; (b) L - Box ratio on varying silica fume on SFCC

Figure 4(a) shows the results of slump flow testing with successive results namely 700 mm; 675 mm; 663 mm; and 658 mm. The test results show that the higher the silica fume content used effect on the lower the concrete's ability to spread. Figure 4(b) shows the results of T50 testing with successive results namely 2.53 seconds, 4.60 seconds, 4.65 seconds, 5.00 seconds. The figure shows that the higher the concentration of silica fume used, the longer the time needed for concrete to reach a diameter of 500 mm, this is because the higher the concentration of silica fume used, the concrete mixture will be thicker because silica fume will absorb more water .

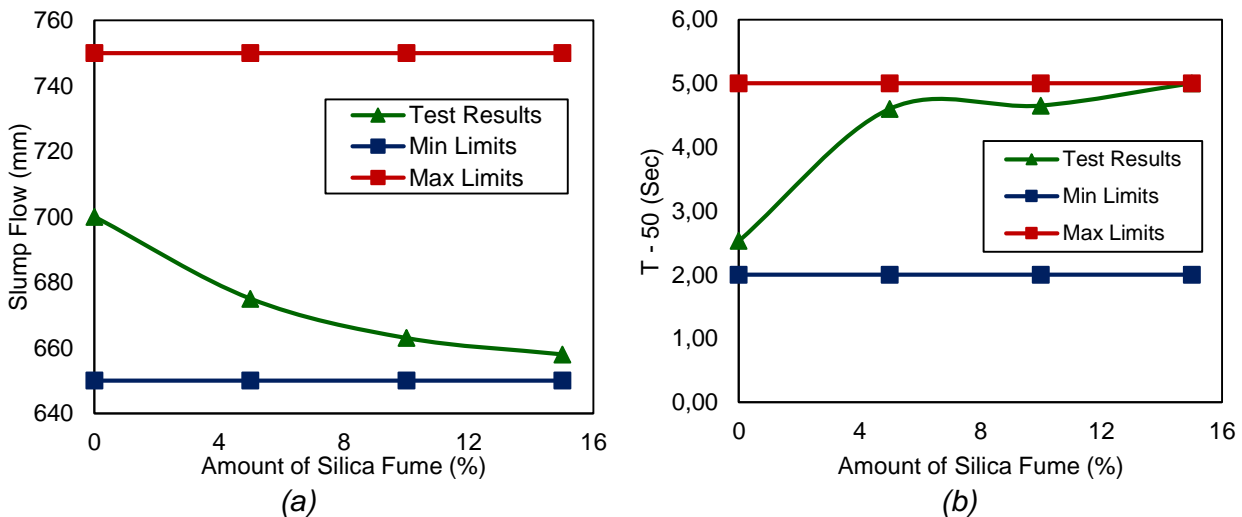


Fig. 4 – (a) Slump flow; (b) T50 result on varying silica fume on SFCC

Mechanic characteristic

Compressive strength testing is done at the age of 7 days, 14 days, 21 days and 28 days. Figure 5(a) shows that the relationship between the varying silica volume and curing age on compressive strength. The result shows that the application of using silica fume affects to the compressive strength. Compressive strength in specimens that do not contain silica fume reaches 32.90 MPa at 28 days. If the compressive strength value of the specimen is compared with the compressive strength of specimens containing silica fume of 5%, an increase of 0.03% occurs. Otherwise, the use of silica fume which exceeds 5% will reduce the compressive strength by

0,07% and 0,15%. This can show that cement replacement by 5% and replacing it with 5% silica fume can increase compressive strength and reduce cement costs. Figure 5(b) illustrates the regression analysis between the amount of silica fume and compressive strength on the specimen at 28 days. From the results of this analysis it is shown that the optimum value of the use of silica fume is limited to 5% to get a good compressive strength. The length of time in the treatment of concrete to be a major factor will affect the value of the compressive strength. This can be seen in Figure 3a that shows the compressive strength value of concrete will increase with increasing concrete curing time that occurs in each silica fume variation.

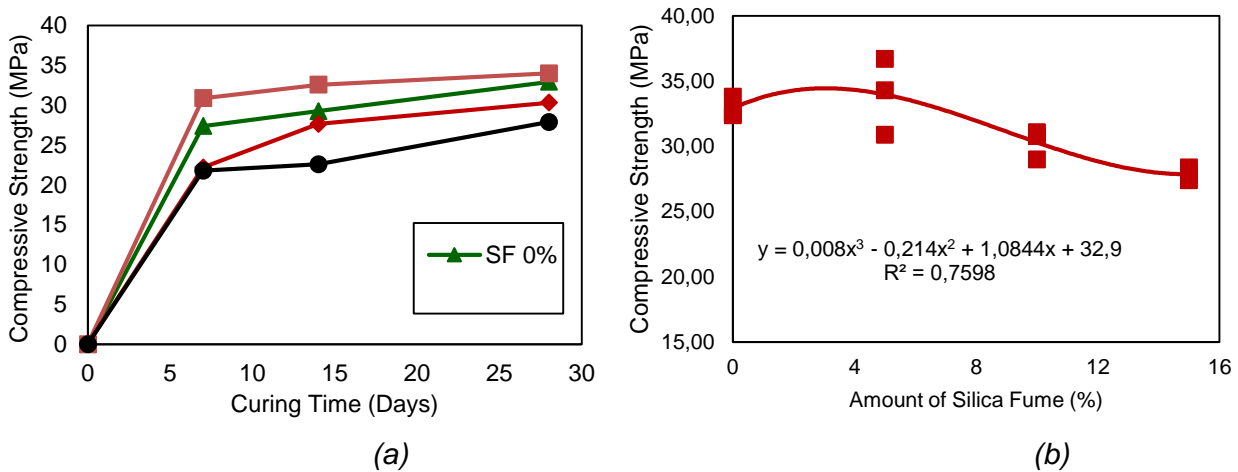


Fig. 5 – Effect of varying silica fume and curing age on Compressive strength SFCC in different curing time

Not only the compressive strength test was carried out in this study, but the split tensile test was also carried out to find out the tensile strength performance of silica fume variations. Figure 6 shows that the application of silica fume in the SFCC mixture effects on the splitting tensile strength. At the 28 curing days of the specimen, the tensile strength of normal SFCC without the silica fume reach 2.88 MPa. By using 5% of silica fume it will be able to increase of tensile strength until 0.2% of normal SFCC otherwise the application of 10% and 15% of silica fume effect on decreasing 0.02% and 0.19% of tensile strength. Therefore, the application of silica fume in the SFCC should limit to 5% that is also proofed in the Figure 6b.

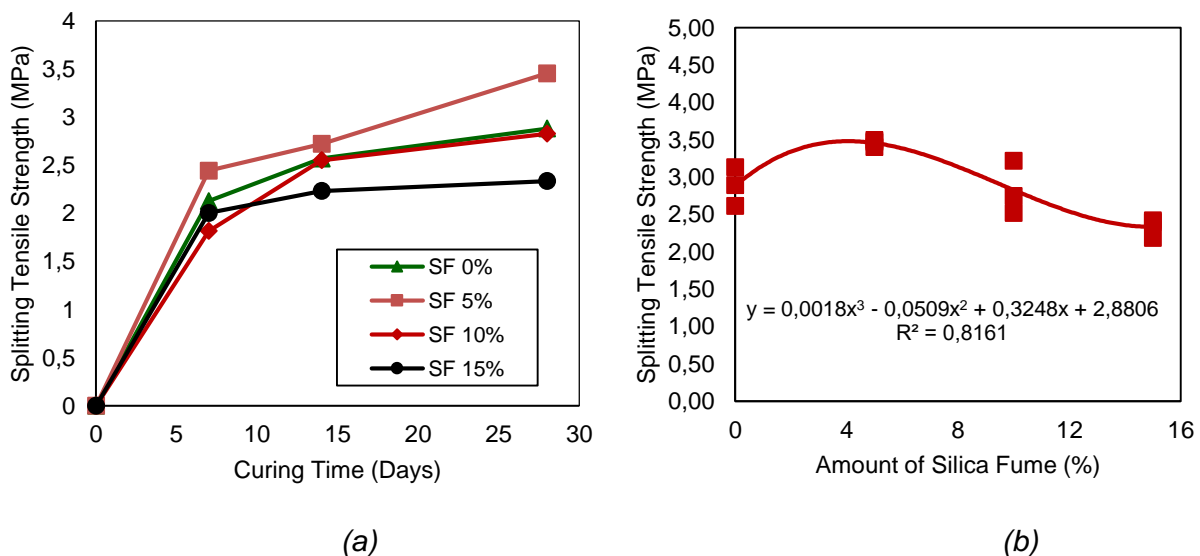


Fig. 6 – Effect of varying silica fume on tensile strength of SFCC in different curing time

Flexural test was conducted to determine the effect of using silica fume on the resulting flexural strength. Figures 7 and Figure 8 show that the application of silica fume on the SFCC effects on flexural strength. The application of 5%, 10% and 15% of silica fume in the SFCC produces the compressive strength 6.63 MPa; 5.44 MPa and 4.81 MPa. The maximum flexural strength is occurred in 5% of silica volume in the SFCC. Not only that, the application of silica fume also effects on the displacement. By using 5% of the silica fume effect on producing of a maximum displacement of around 2.60 mm. Therefore, the optimum level of silica volume that is suitable for mixing SHCC is around 5% according to the compressive strength, tensile strength and flexural strength result.

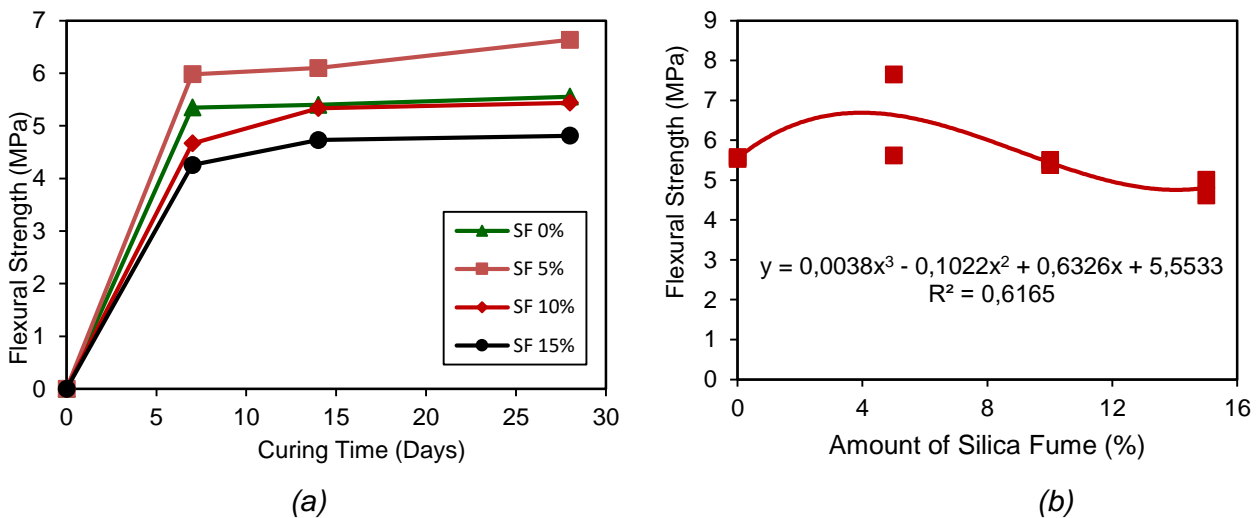


Fig. 7 – Effect of varying silica fume on flexural strength of SFCC in different curing time

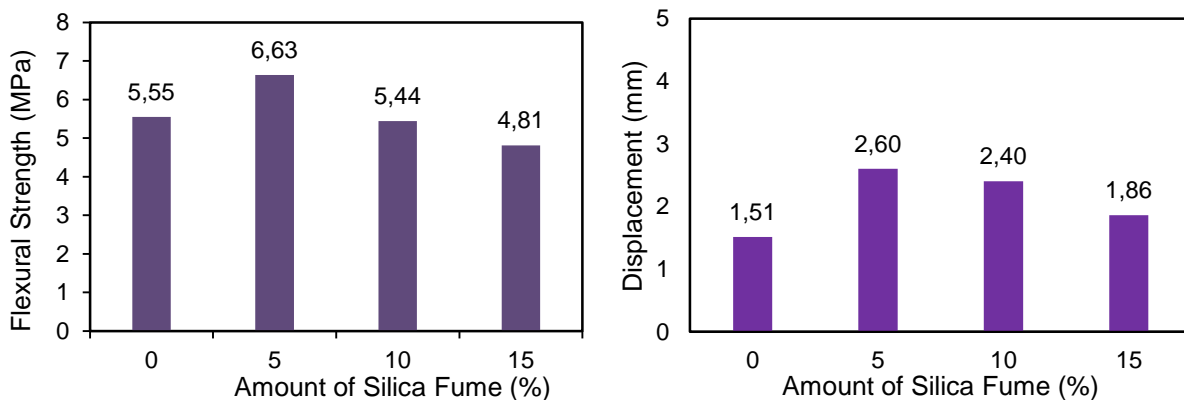


Fig. 8 – Effect of varying silica fume on flexural strength of SFCC in different curing time

CONCLUSION

From the results of the study it can be concluded that:

1. The use of silica fume greatly affects fresh properties. The results of fresh properties testing show that the results obtained from all tests included the terms and conditions of (EFNARC).
2. The use of silica fume which serves as a substitute for cement greatly affects the mechanical properties of concrete. This shows that there are changes in compressive strength, tensile strength and flexural strength when using silica fume.

3. The use of silica fume on SFCC concrete can increase compressive strength, tensile strength and flexural strength. However, its use is only limited to 5%. If the usage exceeds 5% it will reduce the compressive strength of concrete.

ACKNOWLEDGEMENTS

Thank you to the research team Muhammad Rizady Abbyu, Firdaus Riza Al-Latief, Anisha Anggraini, Shindo Sutopo, Hizrah Humairah and Hadi Surya Ramadhan as a laboratory team who helped carry out this research process. To laboratory staff in the structural and building materials engineering laboratory in Department of Civil Engineering, Faculty of Engineering, Universitas Muhammadiyah Yogyakarta.

REFERENCES

- [1] V. Anusuya, C. V. Saranya, and S. N. K. Pravin, "Comparison of the performance of self-compacting concrete", 6th National Conference on Innovative Practices in Construction and Waste Management, pp. 181-185, April 2017.
- [2] M. M. Kamal, M. A. Safan, A. A. Bashandy, and A. M. Khalil, "Experimental Investigation on the behavior of normal strength and high strength self-curing self-compacting concrete", *Journal of Building Engineering*, Vol. 16, pp. 79-93, 2018.
- [3] D. Raharjo, A. Subakti, Tavio, Mixed Concrete Optimization Using Fly Ash, Silica Fume and Iron Slag on the SCC's Compressive Strength. In: *Proceedings of the 2nd International Conference on Rehabilitation and Maintenance in Civil Engineering*, *Procedia Engineering*, 827-839.
- [4] C. Shi. Design and application of self-compacting lightweight concrete. In: *SCC'2005-China: 1st international symposium on design, performance and use of self-consolidating concrete*. RILEM Publications SARL; 2005.
- [5] C. Shi, and Y. Wu, Mixture proportioning and properties of self-consolidating lightweight concrete containing glass powder. *ACI Mater J* 2005;102(5).
- [6] H. Prayuda, F Saleh, T. I. Maulana, F. Monika, Fresh and mechanical properties of self-compacting concrete with coarse aggregate replacement using Waste of Oil Palm Shell, *IOP Conference Series: Materials Science and Engineering*, Vol. 352. 2018.
- [7] A. Khaloo, E. Molaie, R. P. Hosseini, and H. Tahsiri, "Mechanical performance of self-compacting concrete reinforced with steel fibers", *Construction and Building Materials*, Vol. 51, pp. 179-186, 2014.
- [8] M. H. Beigi, J. Berenjian, O. L. Omran, A. S. Nik, and I. M. Nikbin, "An experimental survey on combined effects of fibers and nanosilica on the mechanical, rheological, and durability properties of self-compacting concrete", *Materials and Design*, Vol. 50, pp. 1019-1029, 2013.
- [9] A. Pozolo, and B. Andrawes, Analytical prediction of transfer length in prestressed self-consolidating concrete girders using pull-out test result", *Construction and Building Materials*, Vol. 25, pp. 1026-1036, 2011.
- [10] O. Gencil, "Mechanical properties of self-compacting concrete reinforced with polypropylene fibres" *Materials Research Innovations*, Volume 15, No 3, 2011.
- [11] B. Afriandini, F. Monika, F. Saleh, H. Prayuda, M. D. Cahyati, and S. I. K. Djaha, "Fresh and Hardened Properties of Self Fiber Compacting Concrete (SFCC) Incorporated with Zeolite and Nylon", *IOP Conference Series: Materials Science and Engineering*, Vol 771, 2020.
- [12] G. S. Vijaya, V.G. Ghorpadeb, H.S. Raoc, The Behaviour of Self Compacting Concrete With Waste Plastic Fibers When Subjected To Chloride Attack, In: *Proceedings 5 of Materials Today*, pp. 1501–1508, 2018.
- [13] Kandaswamy and Murugesan, "Fibre reinforced self-compacting concrete using domestic waste plastic fibres", *Journal of Engineering and applied Sciences*, Volume 7, pg 405-410, 2012.
- [14] P. Aggarwal, R. Siddique, Y. Aggarwal, and S. M. Gupta, "Self-Compacting Concrete Procedure for Mix Design", *Leonardo Electronic Journal of Practices and Technologies*, Vol. 12, pp. 15-24, 2008.
- [15] European Federation of National Trade Associations Representing Producers and Applicator of Specialist Building Products (EFNARC), "Specification and Guidelines for Self-Compacting Concrete", Hampshire, U.K, 2002.
- [16] ASTM C39/ C39M-18, 'Standard Test Method for Compressive Strength of cylindrical Concrete



Specimens', ASTM International, West Conshohocken, PA, 2018.

[17] ASTM C496/ C496M -17, "Standard Test Method for Splitting Tensile Strength of Cylindrical Concrete Specimens", ASTM International, West Conshohocken, PA, 2017.

[18] ASTM C293/ C293M -16, 'Standard Test Method for Flexural Strength of Concrete (Using Simple Beam with Center Point Loading)', ASTM International, West Conshohocken, PA, 2016.

ANALYTICAL SOLUTION AND FIELD TEST OF CRITICAL BEARING CAPACITY AND SETTLEMENT OF PILE TIP

Suchun Yang^{}, Junwei Liu[#], Mingyi Zhang[#], Yonghong Wang*

*Qingdao University of Technology, School of Civil Engineering, Qingdao, China;
zjuljw@126.com; zmy58@163.com*

ABSTRACT

In order to explore the relationship between the critical bearing capacity and settlement of closed pile tip pierced into the soil, based on the Boussinesq solution and the Kelvin solution, the analytical solution between the critical bearing capacity and the critical settlement of the closed pile tip is derived by combining the stress distribution function. The analytical solution of critical bearing capacity and settlement of pile tip is verified by field test of static pressure pile penetrating into layered soil with a full-section pressure sensor installed at pile tip. The results show that during the penetration process, the bearing capacity increase stage of the pile tip is divided into linear steepening section and nonlinear slow increasing section. The soil in the linear steep increase section behaves as an elastic state. The bearing capacity of the pile tip before the punctured soil layer is linear with the settlement, and the final value of the linear steep increase section is the elastic limit value and the critical bearing capacity of the piercing pile tip. When the residual pile tip force is not considered, the critical settlement of the pile tip is between 0.095-0.119d; when considering the residual pile tip force, the critical settlement is between 0.091-0.105d. In particular, when the Poisson's ratio is 0.5, the analytical solution of the semi-infinite space is equivalent to the analytical solution of the infinite space.

KEYWORDS

Pile tip force, Piercing, Settlement, Critical bearing capacity, Field test

Introduction

The relationship between bearing capacity and settlement of pile has always been the focus of research in the field of pile foundation engineering. Especially for settlement-reducing pile, the bearing capacity within the reasonable settlement range is the basis of piles design [1]-[3]. Many scholars have carried out a lot of research on the relationship between bearing capacity and settlement of pile [4]-[6], but only a few experiments are concerned with the relationship between ultimate bearing capacity and settlement of pile tip in the critical state [7]-[10], the relationship between the critical bearing capacity and settlement of pile is not established. The analytical solution is only for numerical simulation analysis of sand [11]-[12]. The relationship between the critical bearing capacity and settlement of a pile tip is of great significance for different working conditions. For example, for the end-bearing pile, the pile tip bearing capacity within the

reasonable settlement can be calculated. For the rigid composite foundation, the thickness of the cushion layer can be reasonably designed according to the critical bearing capacity of the pile top when piercing the cushion layer to better exert the bearing capacity of the composite foundation.

The existing bearing capacity theory of pile tip mainly includes load transfer method [13], elastic theory method [14], ultimate bearing capacity theory [15]-[18], etc., but the problem of penetration is not well explained. The process of dynamic penetration of the pile foundation into the soil layer has a process of acceleration and deceleration. The difficulty of measuring the acceleration will result in difficulty in balancing the pile foundation during the force analysis, and the huge soil compaction effect caused by the dynamic penetration will lead to the change of soil properties. However, the pile is a quasi-static process before the soil layer is pierced. The Boussinesq problem and the Kelvin problem can well solve the ultimate bearing capacity and settlement relationship between shallow and deep soil layers, but the force is still the point load. This requires a point load to be converted into a surface load to find a reasonable stress distribution function. The author deducts the assumed stress distribution function by the inverse solution method to meet the settlement of pile tip, solves the transformation of the pile tip force from the point load to the surface load, and combines the closed pile with the full section pressure sensor installed on the pile tip. Through the layered soil test [19], the analytical solution of the bearing capacity and settlement of the pile tip was verified.

Analytical solution of bearing capacity and settlement of pile tip in shallow soil

The Boussinesq solution assumes that the concentrated load acts on the surface of the semi-infinite space homogeneous elastomer. When the pile tip is in initial contact with the soil, it can be considered that the surface load acts on the surface of the semi-infinite space homogeneous elastomer. At this time, the soil is an undisturbed soil and satisfies the assumptions of uniformity, continuousness, small deformation, and elasticity. As the penetration force increases, the pile tip is more closely in contact with the surface of the soil, and the soil is compressed in the elastic range. At this time, the relevant assumptions of the Boussinesq solution can still be satisfied; As the penetration force continues to increase, the soil at the pile tip will not be able to satisfy the small deformation hypothesis. At this time, the force at the pile tip is the critical bearing capacity of the pile tip, and the Boussinesq solution fails at the next moment.

Boussinesq solution of bearing capacity and settlement of pile tip

For the initial penetrating soil at the pile tip, the solution of the vertical concentrated force and settlement in the semi-infinite space can be solved, that is, the spatial vertical settlement of the Boussinesq problem is solved.

Formula:

$$u_z = \frac{1+\nu}{2\pi E} \left[\frac{2(1-\nu)}{r} + \frac{z^2}{r^3} \right] F_z \quad (1)$$

Among them, u_z is the vertical settlement, $r = \sqrt{x^2 + y^2 + z^2}$, E is the compressive modulus of the soil, ν is the Poisson's ratio of the soil, and F_z is the penetration force of the pile tip.

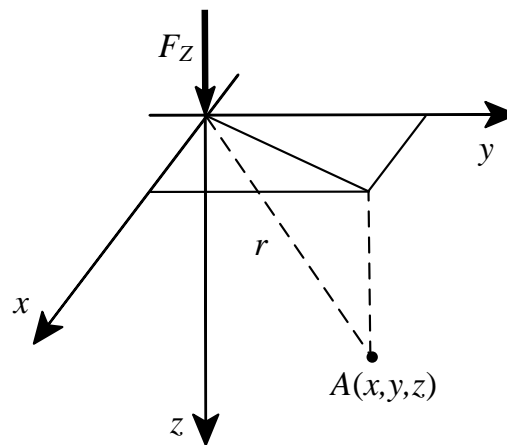


Fig.1 - Boussinesq problem schematic

Take the center of the coordinate axis as the center of the pile tip, and $z=0$ at the pile tip in the half-space infinite body. The coordinate system is shown in Figure1. The vertical settlement is simplified as:

$$u_z = \frac{(1-\nu^2)}{\pi E} \frac{F_z}{r} \quad (2)$$

$$\text{Where } r = \sqrt{x^2 + y^2}.$$

Analytical solution of bearing capacity and settlement of pile tip in semi-infinite space

The force of the Boussinesq problem is a vertical concentration force, and the vertical settlement caused by multiple vertical concentrated forces can be obtained by superposition. In order to study the pile tip penetration force, a finite number of vertical concentrated force superposition methods cannot be used. The stress distribution function is required, and the stress distribution function is assumed according to the dimension:

$$p = p_0 \left(1 - \frac{r^2}{a^2}\right)^{-\frac{1}{2}} \quad (3)$$

$$\iint p dx dy = F_z \quad (4)$$

Where p_0 is the compressive stress amplitude, a is the pile tip radius, r is the arbitrary point to the axial distance; the distribution curve of the stress function in the radius is shown in Figure 2.

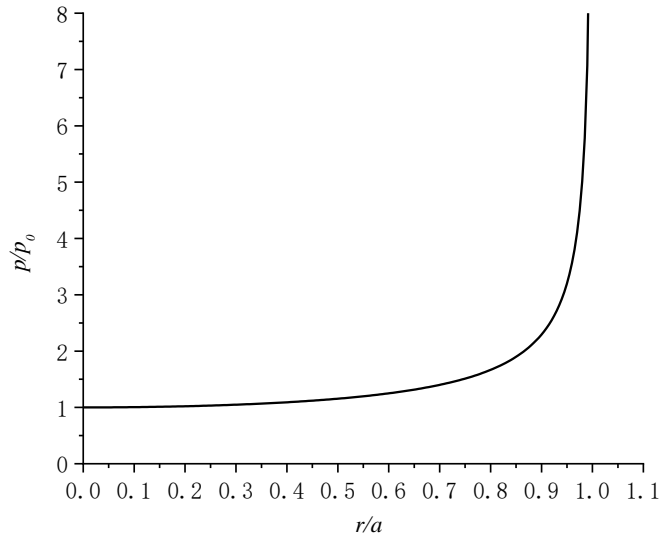


Fig.2 - Stress function curve

Combined with the stress distribution function formula (2) becomes:

$$u_z = \frac{1-\nu^2}{\pi E} \iint \frac{p(x,y)}{r} dx dy \quad (5)$$

Due to the rotational symmetry of the pile tip, the vertical settlement of a point is only related to its distance r from the center point, for which only the settlement of the point on the x -axis needs to be calculated. Take the point A coordinate (x,y) on the x -axis and any point B coordinate (x',y') on the pile tip. According to the positional relationship shown in Figure3, $t^2 = r^2 + s^2 + 2rscos\varphi$.

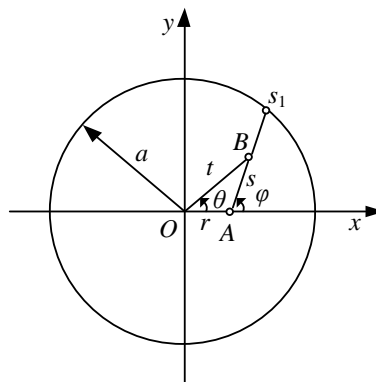


Fig.3 - Position relations of various points in the pile tip area

Stress at point B:

$$p(s, \varphi) = p_0 \left(1 - \frac{r^2 + s^2 + 2rs \cos \varphi}{a^2}\right)^{-\frac{1}{2}} = p_0 a (a^2 - r^2 - s^2 - 2rs \cos \varphi) \quad (6)$$

The settlement at point A is equal to the superposition of any point at pile tip, and is obtained according to formula (7):

$$u_z = \frac{1-\nu^2}{\pi E} p_0 a \int_0^{2\pi} \left(\int_0^{s_1} (a^2 - r^2 - 2rs \cos \varphi - s^2)^{-\frac{1}{2}} ds\right) d\varphi \quad (7)$$

Where s_1 is the positive root of the equation $a^2 - r^2 - 2rs \cos \varphi - s^2 = 0$,

$$\int_0^{s_1} (a^2 - r^2 - 2rs \cos \varphi - s^2)^{-\frac{1}{2}} ds = \frac{\pi}{2} - \arctan \left[\frac{r \cos \varphi}{(a^2 - r^2)^{\frac{1}{2}}} \right]$$

Equation (7) is calculated:

$$u_z = \frac{1-\nu^2}{\pi E} p_0 a \int_0^{2\pi} \frac{\pi}{2} d\varphi = \frac{\pi(1-\nu^2)p_0 a}{E} = \text{constant} \quad (8)$$

The vertical settlement of each point in the contact area of a closed pile tip is the same under the condition of displacement coordination.

Calculated by (4) conversion element integration:

$$F_z = \int_0^a p_0 \left(1 - \frac{r^2}{a^2}\right)^{-\frac{1}{2}} 2\pi r dr = 2\pi p_0 a^2 \quad (9)$$

The simultaneous equations (8) and (9) get:

$$u_z = \frac{(1-\nu^2) F_z}{2 E a} \quad (10)$$

Analytical solution of bearing capacity and settlement of pile tip in deep soil

Kelvin's solution is based on the assumption that the concentrated load acts on the surface of the infinite space homogeneous elastomer. The initial contact between the pile tip and the deep soil can also be considered as the surface load acting on the surface of the infinite space homogeneous elastomer. At this time, the deep soil is the original. The soil satisfies the assumptions of uniformity, continuousness, small deformation, and elasticity.

As the penetration force increases, the pile tip is more closely in contact with the surface of the soil, and the soil is compressed in the elastic range, and the relevant assumption of the Kelvin solution can still be satisfied at this time; As the penetration force continues to increase, the soil at the pile tip will produce a critical moment of compaction, and the soil will not be able to satisfy the small deformation hypothesis. At this time, the pile tip force is the critical bearing capacity of the pile tip. At the next moment, Kelvin's solution failed.

Kelvin solution of bearing capacity and settlement of pile tip

For the ultimate bearing capacity of the pile tip in the deep soil layer, the Kelvin problem in the infinite space can be solved, and the vertical settlement solution according to the Kelvin problem:

$$u_z = \frac{1}{2(1-\nu)} \frac{(1+\nu)}{4\pi E} \left[\frac{2(1-2\nu)}{r} + \frac{1}{r} + \frac{z^3}{r^3} \right] F_z \quad (11)$$

Taking the center of the coordinate axis as the center of the pile tip and taking $z=0$ in the infinite body, the vertical settlement is simplified as:

$$u_z = \frac{(1+\nu)}{2(1-\nu)} \frac{(3-2\nu)}{4\pi E} \frac{F_z}{r} \quad (12)$$

Analytical solution of bearing capacity and settlement of pile tip in infinite space

The stress distribution function formula (12) combined with (3) becomes:

$$u_z = \frac{(1+\nu)}{2(1-\nu)} \frac{(3-2\nu)}{4\pi E} \iint \frac{p(x,y)}{r} dx dy \quad (13)$$

Substituting (6) into (13) gives:

$$u_z = \frac{(1+\nu)}{2(1-\nu)} \frac{(3-2\nu)}{4\pi E} p_0 a \int_0^{2\pi} \left(\int_0^{s_1} (a^2 - r^2 - 2r s \cos\varphi - s^2)^{\frac{1}{2}} ds \right) d\varphi \quad (14)$$

The same reason:

$$\int_0^{s_1} (a^2 - r^2 - 2r s \cos\varphi - s^2)^{\frac{1}{2}} ds = \frac{\pi}{2} - \arctan \left[\frac{r \cos\varphi}{(a^2 - r^2)^{\frac{1}{2}}} \right]$$

(14) Simplification is obtained:

$$u_z = \frac{(1+\nu)}{(1-\nu)} \frac{(3-2\nu)}{8E} p_0 a \pi = \text{constant} \quad (15)$$

The settlement of each point at the pile tip is constant, and the vertical settlement of each point in the contact area of the closed pile tip is consistent, which is consistent with the displacement coordination condition of the pile tip.

Substituting (9) into (15) gives:

$$u_z = \frac{(1+\nu)}{(1-\nu)} \frac{(3-2\nu)}{16} \frac{F_z}{Ea} \quad (16)$$

Boussinesq solution is equivalent to Kelvin solution

When the semi-infinite space load-settlement analytical solution is equal to the infinite space load-settlement analytical solution, when equations (10) and (16) are equivalent:

$$u_z = \frac{(1 - \nu^2) F_z}{2 E a} = \frac{(1 + \nu) (3 - 2\nu) F_z}{(1 - \nu) 16 E a}$$

Solving $\nu = 0.5$ or $\nu = 1.25$, when Poisson's ratio is equal to 0.5 means that formula (10) is equivalent to formula (16) under the incompressible material or under the combined effects of shear dilatation and reduction;

The Poisson's ratio can be greater than 0.5 due to the shear dilatation of the soil, but the case of $\nu = 1.25$ has not yet appeared in the soil. Therefore, the analytical solution of the semi-infinite space load-settlement is equivalent to the infinite space load-settlement analytical solution with Poisson's ratio $\nu = 0.5$.

Verification and analysis of bearing capacity and settlement of pile tips in shallow and deep soil

Field test overview

In order to verify the relationship between the critical bearing capacity and the settlement of the pile tip, an on-site static pressure pile test was carried out. The test site is located in Dongying, Shandong Province, about 20 kilometers away from the Yellow River. It belongs to the Yellow River impact plain and has clear soil layers. It is mainly composed of silt and silty clay. The soil layer is shown in Table 1. The pile diameter is 400mm and the pile length is 12m. A 100t full-section pressure sensor is placed at the end of the closed pile. The test position and sensor^[19] are shown in Figure 4.

Tab. 1 - Stratigraphic parameters

Depth/m	Soil layer	Compression modulus E_{s1-2} / MPa	Void ratio e	Water content w / %	Cone penetration test Q_c / MPa	\bar{N}
0~3.08	① Plain fill(q4ml)	4.19	0.867	30.4	1.130	2.9
3.08~4.58	② Silt(q4al)	8.55	0.803	27.7	2.796	5.4
4.58~5.08	③ Silty clay(q4al)	4.90	0.876	30.5	0.928	3.4
5.08~6.98	④ Silt(q4al)	9.11	0.794	28.0	4.930	9.4
6.98~10.38	⑤ Silty clay(q4al)	4.67	0.895	31.5	0.799	2.7
10.38~13.88	⑥ Silt(q4al)	10.54	0.793	28.0	7.379	16.2

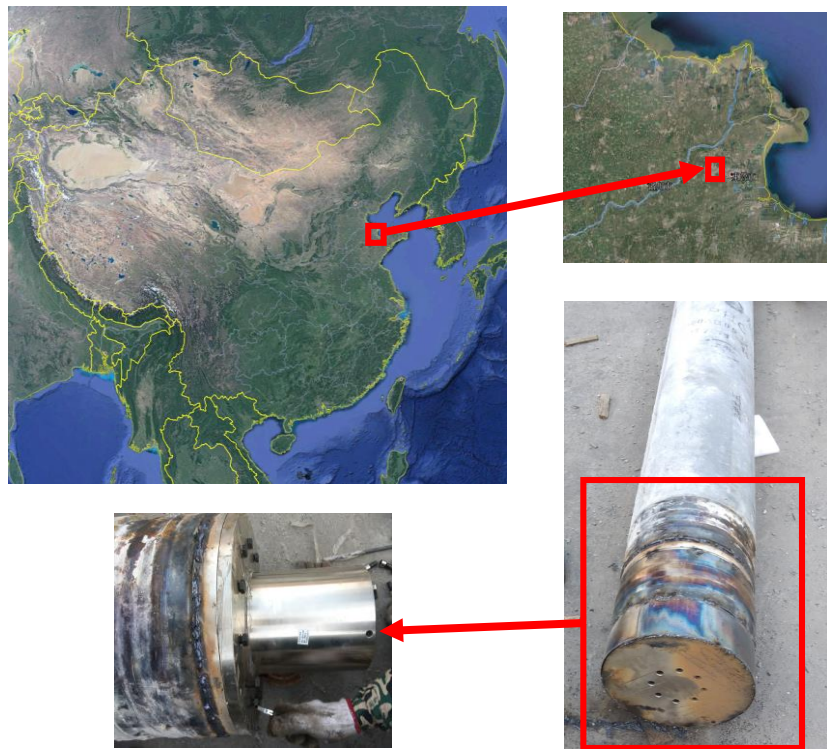


Fig.4 - Test position and sensor

Test analysis and verification

The static pressure pile penetration test was carried out in 9 strokes, and the penetration depth of each stroke was about 1.4 meters, the penetration rate of each stroke is 1.2 m / min, the penetration time of each stroke is about 70 seconds. The relationship between the pile tip resistance and the penetration depth is shown in Figure 5. After the static pressure penetration of each stroke is started, there is a stage of accumulating pressure for each stroke before the pile tip punctures the soil layer. During this period, the deformation of the soil is mainly compressed. When the pile tip force breaks through the penetration threshold, the pile will penetrate into the soil layer quickly.

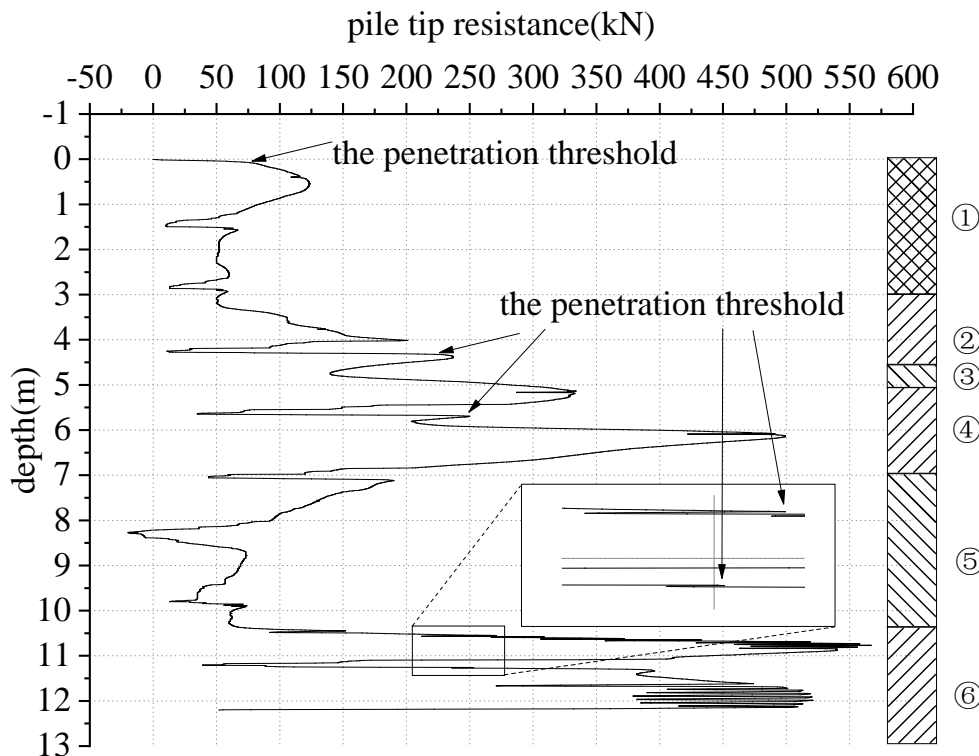


Fig.5 - Relationship between resistance and depth of pile tip

The process of pile penetration will produce severe soil squeezing effect. When the pile tip penetrates the hard layer, it has a large soil squeezing effect on the soft soil layer under the hard layer. The nature of the soft layer soil has changed and cannot be obtained by geological survey parameters[20]-[21]. The process of the pile tip penetrating from the soft layer to the hard layer. The soil squeezing effect from the soft layer to the hard layer under the pile tip is small, and the hard layer soil is less affected and can be obtained by geological survey parameters

In order to study the penetration threshold of the pile tip and eliminate extrusion effect on the soil layer, the stroke 1, the stroke 4, the stroke 5, the stroke 8 and the stroke 9 are selected for analysis. The relationship between the pile tip force and depth of each stroke is shown in Figures 6-8. It can be seen from Figures 6-8 that the pile tip force increases linearly before the pile penetrates, and the final value of linear growth is the critical bearing capacity of the piercing (or the penetration threshold). When the critical bearing capacity is reached, the vertical settlement of the pile is small, and the soil deformation is mainly compressed; after the pile penetrates into the soil layer, the bearing capacity reaches the peak with the development of soil squeezing, but the peak of bearing capacity requires large vertical settlement. The maximum bearing capacity of piles cannot be used in the design of structures, and the vertical settlement of the critical bearing capacity is small for design reference.

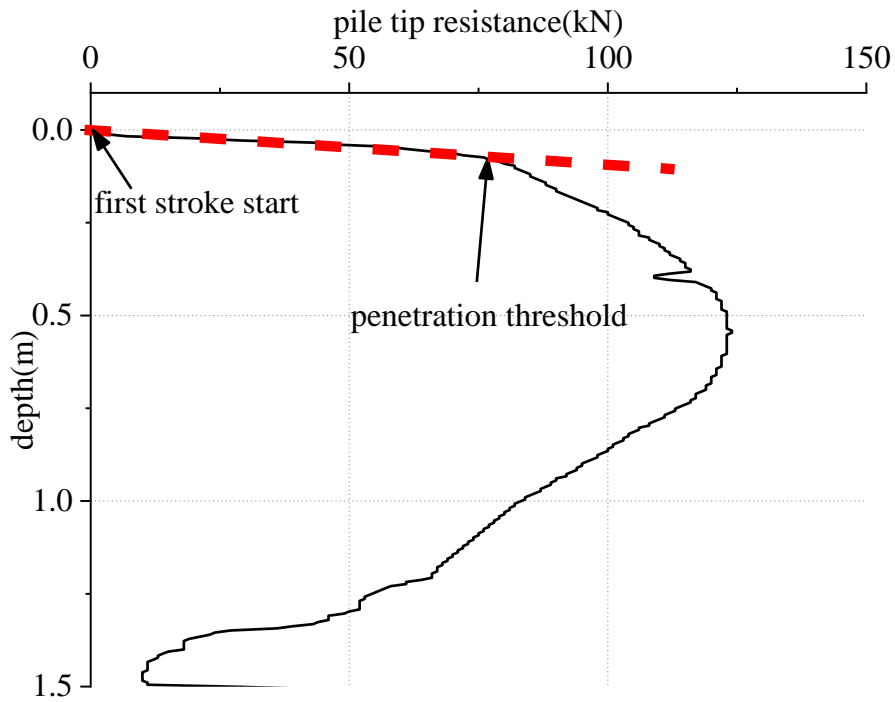


Fig.6 - The relationship between pile tip resistance and depth during the first stroke

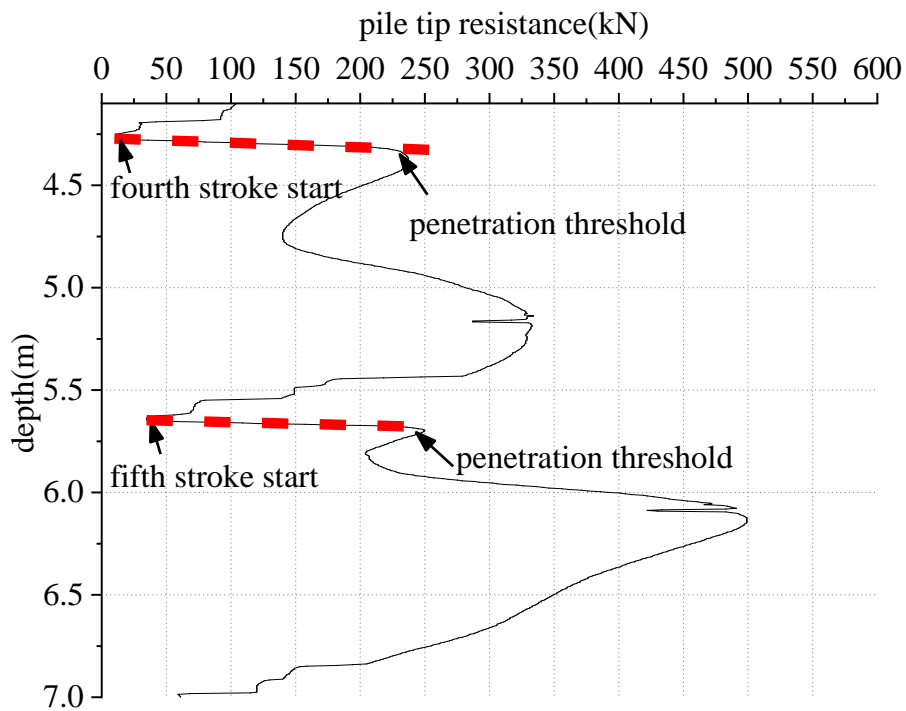


Fig.7 - The relationship between pile tip resistance and depth during the fourth and fifth stroke

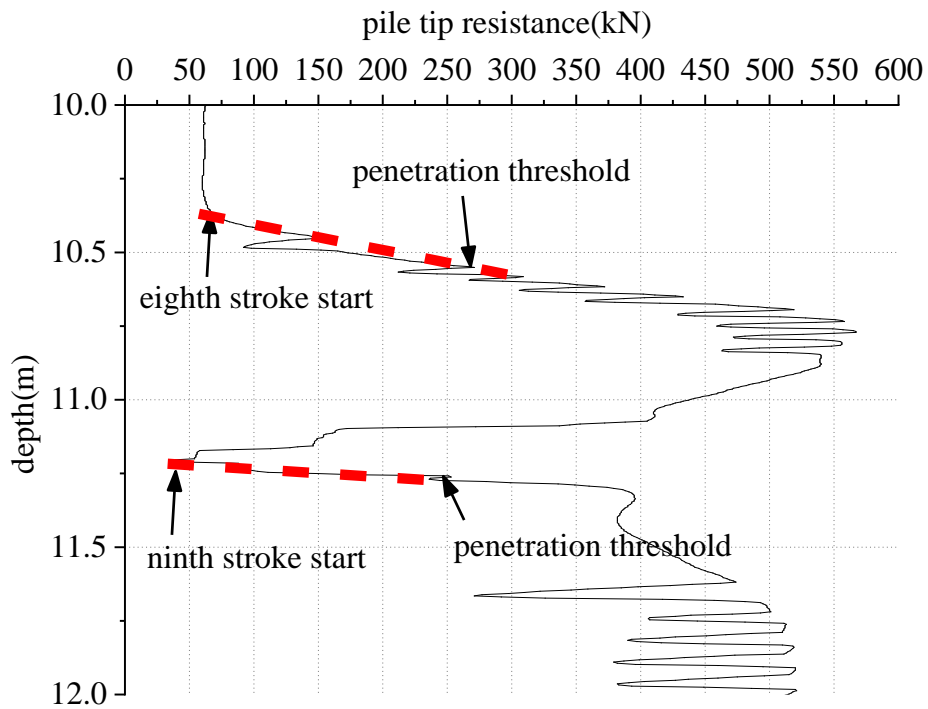


Fig.8 - The relationship between pile tip resistance and depth during the eighth and ninth stroke

According to the reference [22], the Poisson's ratio of the surface layer is stable at 0.42 and the deep layer is stable at 0.49. According to formula (10) and formula (16), the vertical settlement u_z and the pile diameter d is normalized, and the starting values of each research stroke and the penetration threshold are listed in Table 2.

Tab. 2 - The relationship between the critical bearing capacity and settlement of pile tip

Soil layer	Compression modulus E_{s1-2} / MPa	Residual pile tip force / kN	Critical bearing capacity (penetration on threshold) / kN	The value of $\frac{u_z}{d}$		
				Not considering residual force	Considering residual force	Field test value
① Plain fill (q4ml)	4.19	0	77	0.095	0.095	0.200 (Ground Hard Shell)
② Silt (q4al)	8.55	15	209	0.113	0.105	0.095
④ Silt (q4al)	9.11	36	217	0.110	0.092	0.097
⑥ Silt (q4al)	10.54	62	271	0.119	0.091	0.450 (Junction of soil layer)
⑥ Silt (q4al)	10.54	39	253	0.111	0.094	0.136

It can be seen from the data in Table 2 when the residual pile tip force is not considered, the theoretical value of the ultimate settlement and diameter ratio is between 0.095-0.119d, and the critical settlement to diameter ratio is between 0.091-0.105d when considering the residual pile tip force. When the field test value in a single soil layer and the indoor model test data in reference [12], the critical settlement is within 0.1d, which is basically consistent with the elastic phase test data. However, at the junction of the soil layer and the hard shell on the ground, the critical settlement to diameter ratio will have a large difference. This is due to the difference in the elastic modulus of the soft and hard layers. It is proved that formula (10) and formula (16) are suitable for calculating the relationship between the bearing capacity and settlement of the pile tip in the indoor and field test, but they are nearly suitable for pile tips acting on stable soil layers.

CONCLUSION

(1) Based on the Boussinesq solution and the Kelvin solution, the analytical solution between the critical bearing capacity and the critical settlement of the closed pile tip is derived by combining the stress distribution function. When the Poisson's ratio is 0.5, the analytical solution of the semi-infinite space is equivalent to the analytical solution of the infinite space.

(2) Through the field test of the static pressure pile with the full-section pressure sensor penetrating into the layered soil, it is found that the bearing capacity of the pile tip is linear with the settlement before the piercing, and the final value of linear growth is the critical bearing capacity of the pile tip.

(3) When the residual pile tip force is not considered, the critical settlement of the pile tip is between 0.095-0.119d; when considering the residual pile tip force, the critical settlement is between 0.091-0.105d. The analytical solution between the critical bearing capacity and the settlement of the pile tip can be used as the design basis of the pile foundation.

REFERENCES

- [1] LIU R, XU Y, YAN S W. Finite element analysis of action characteristics of anti-settlement pile foundation[J]. *Engineering Mechanics*, 2006 (02): 144-148.
- [2] ZAI J M. Concept of plastically bearing pile and its practical application[J]. *Chinese Journal of Geotechnical Engineering*, 2001, 23(3): 273-278. (in Chinese)
- [3] ZHENG G, LIU R. Engineering examples and finite element analysis of interaction mechanism between reducing pile and soil[J]. *Journal of Tianjin University*, 2001 (02): 209-213.
- [4] CHEN L Z, LIANG G Q, ZHU J Y, et al. An Analytical Method for the Axial Load-Settlement Curve of Piles [J]. *Journal of Geotechnical Engineering*, 1994 (06): 30-38.
- [5] CHI Y J, SONG E X, GAO W X, et al. Experimental Study on Bearing and Deformation Characteristics of Rigid Pile Composite Foundation [J]. *Journal of China University of Mining and Technology*, 2002 (03): 24-28.
- [6] Crispin, J. J., Leahy, C. P., & Mylonakis, G. (2018). Winkler model for axially loaded piles in inhomogeneous soil. *Géotechnique Letters*, 8(4), 290-297. doi:10.1680/jgele.18.00062
- [7] ZHOU Z J, ZHENG H. Working characteristics of cushion during the whole process of pile penetration [J]. *Journal of Civil and Environmental Engineering (Chinese and English)*, 2019 (03): 41-48.
- [8] ZHANG D G, ZHANG Z, YAN M L, et al. [J]. *Architectural Science*, 2014, 30 (05): 52-57.
- [9] ZHOU J, WANG Q Q, GUO J J. Centrifuge Test Study on pile tip penetration [J]. *Industrial Building*, 2012, 42 (08): 75-78.
- [10] WANG H, ZHOU J, DENG Z H. Mobilization of toe resistance of piles with local displacement in sand[J]. *Chinese Journal of Geotechnical Engineering*, 2006, 28(5): 587-593.(in Chinese)
- [11] ZHOU J, HUANG J, ZHANG J, et al. Numerical simulation of pile tip penetration in stratified media based on three-dimensional discrete-continuous coupling method [J]. *Journal of Rock Mechanics and Engineering*, 2012, 31 (12): 2564-2571.
- [12] ZHOU J, GAO B, GUO J J, et al. Model test and numerical simulation of pile tip force under different penetration depth [J]. *Journal of Tongji University (Natural Science Edition)*, 2012, 40 (03): 379-384.
- [13] YANG H, YANG M. A review of load-settlement relationship of single pile by load transfer method [J]. *Journal of Underground Space and Engineering*, 2006 (01): 155-159+165.
- [14] AI Z Y, YANG M. Application of generalized Mindlin solution in single pile analysis of multi-layer foundation [J]. *Journal of Civil Engineering*, 2001 (02): 89-95.
- [15] TERZAGHI K. *Theoretical soil mechanics*[M]. New York: Wiley & Sons Inc, 1943.
- [16] MEYERHOF G G. The ultimate bearing capacity of foundations [J]. *Geotechnique*, 1951, 2 (4): 301.
- [17] BEREZANTZEV V G, KHRISTOFOROV V, GOLUKOV V. Load bearing capacity and deformation of piled foundations [C] // *Proceedings of the 5th International Conference on Soil Mechanics and Foundation Engineering*. Paris:[s. n.], 1961:1-15.
- [18] VESIC A S. Ultimate loads and settlements of deep foundations in sand [C] // *Proc of a symposium bearing capacity and settlement of foundations*. Durham: Duke University, 1967: 53-68.
- [19] YANG S C, ZHANG M Y, WANG Y H, et al. [J]. *Geotechnical Mechanics*, 2018,39 (S2): 91-99.



- [20] PAN H, CHEN G X, SUN T. Experimental study on the Poisson's ratio of undisturbed marine soil [J]. *Geotechnical Mechanics*, 2011, 32 (S1): 346-350.
- [21] He W M, Li D Q, Yang J, et al. Research progress of dynamic shear modulus, damping ratio and Poisson's ratio of soil [J]. *Journal of Seismic Engineering*, 2016, 38 (02): 309-317.
- [22] GAO W P, CHEN Y K, LIU F. Preliminary analysis of Poisson's ratio characteristics of shallow strata in Tianjin [J]. *Journal of Seismic Engineering*, 2014, 36 (01): 47-53.

A NEW BLAST-RESISTANT DESIGN METHOD OF RC MEMBERS AND ITS APPLICATION IN PERFORMANCE BASED BLAST-RESISTANT DESIGN PROCEDURE

Runqing Yu¹, Diandian Zhang¹, Yujun Cang², Sen Li²

1. Air Force Second Service Group of Engineering and Technology, No. 616 South Baiyun Road, Baiyun District, Guangzhou 510403, China; jkgqklj@qq.com, zhangdiandian07@qq.com
2. Southern Air force design office, No. 243 Yuexiu Road, Yuexiu District, Guangzhou 510052, China; 13570346022@139.com, 928424264@qq.com

ABSTRACT

Design method is very essential and important for engineers. Present study proposes a new blast-resistant design method. First, two common used blast-resistant design methods are discussed. By analyzing the disadvantage of the common procedures, a new blast-resistant design method is proposed. The new design method has less design loops, as well as good control of the maximum displacement and ductility. Then, a dimensionless P-I diagram, which is convenient for design, is proposed based on the new design method. Finally, the new blast-resistant design method is applied in the performance-based blast-resistant design (PBBD) procedure described using a detailed design example. The design example shows that the proposed design method could be easily applied in the PBBD procedure.

KEYWORDS

Performance-based, Blast-resistant, Design procedure, P-I diagram

INTRODUCTION

Performance-Based Design (PBD) method is firstly proposed in earthquake engineering [1]. Recently, there is a trend in civil engineering community to use PBD method in other subfields of structural engineering [2-5]. Meanwhile, blast-resistant design is necessary with an increasing attention after September 11, 2001. Thus, the application of PBD method in the field of blast-resistant design will be very meaningful [6, 7].

Performance-Based Earthquake Design (PBED) is more mature and provides a certain reference for PBBD procedure. During the development process of PBED, two generations design procedures are proposed by engineers [8]. The first-generation procedure is a deterministic framework. It includes methods of defining performance, methodologies to calculate building dynamic response and structural response parameters to assess performance levels of structures [7, 9]. The second-generation procedure is a full probabilistic framework. It considers the inherent uncertainties and variability in structural response and provides risk management decisions for engineers [9]. Similar to PBED method, studies about the PBBD procedure are also categorized into two kinds. The first one does not consider the uncertainties while the second one does. Studies of the first kind include uncertainties about blast loads [10, 11], fragility curves of RC structures [12, 13], loss estimation of buildings after explosion [14], etc. Studies of the second kind include determination of explosion scenarios [7, 15], determination of damage criteria [16, 17], optimization design methods [18, 19], etc. However, few studies pay attention to the blast-resistant design procedure.

The design method is different from the dynamic response analysis method. The design method is to calculate the structural configuration based on the objective performance, while the dynamic response method is to calculate the structural performance based on the known configuration of structures. The dynamic response method could also be used as design method by the application of try-and-error method. For example, UFC 3-340-02 [20] directly uses the dynamic response analysis method single-degree-of-freedom (SDOF) to design the RC beam. The design procedure in UFC 3-340-02 for RC beams (named as Design procedure A) is shown in Figure 1. After the determination of blast load, geometric sizes, materials and objective performances, trial designs are conducted for many times until the objective performances are satisfied. The trial designs will add extra work to designers.

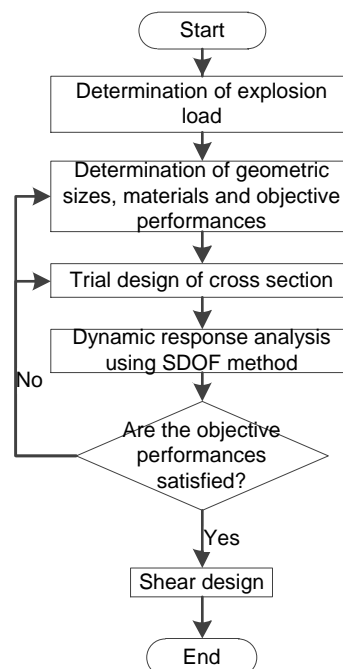


Fig. 1 – Design procedure A

In order to reduce the design loops, dynamic increase factors are calculated using SDOF method. Then, the blast load is transformed to an equivalent static load. RC members are designed using the static design method. This method is called as equivalent static load design method [21], which has less design loops, as shown in Figure 2 (named as Design procedure B). This method is more convenient to designers and widely accepted in China.

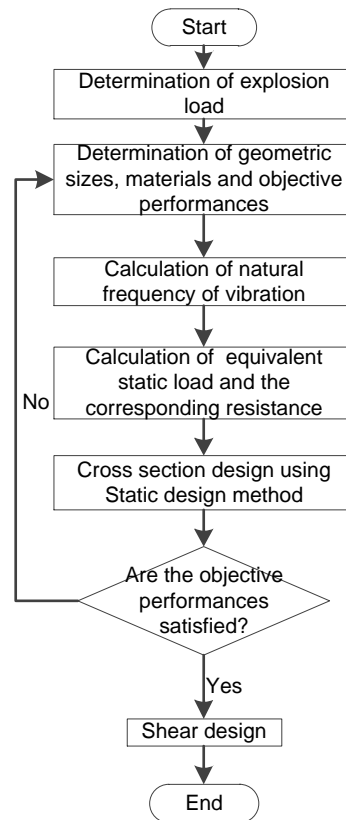


Fig. 2 – Design procedure B

An efficient design procedure is very important in the actual design practices. It should be time-saving and accurately control the objective performances. The common used performance indexes are maximum displacement and ductility ratio, which are used in Design procedure A and Design procedure B respectively. However, the both indexes represent the performances. Designing the RC members using two performance indexes will be helpful to control the objective performances.

In present study, a new blast-resistant design procedure was presented. The new procedure combines the advantages of Design procedures A and B. The maximum displacement and ductility ratio are simultaneously used as performance indexes in the new procedure. Then, a neat PBBD procedure is present based on the new design procedure.

THEORETICAL BASICS OF DESIGN PROCEDURE FOR RC MEMBERS

RC member subjected to blast load is simplified into a perfect elastic-plastic SDOF system shown in Figure 3.

Equation (1) is used to calculate the dynamic response

$$M_e \ddot{y} + R(y) = P(t)L \quad (1)$$

where L is the span length, $R(y)$ is the resistance function, and $P(t)$ is the linear blast load.

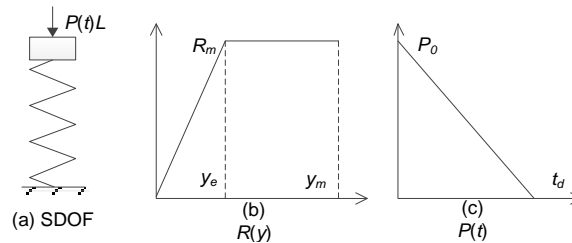


Fig. 3 – SDOF system

The resistance R_m is calculated by Equation (2) according to [22] (Bounds 2010)

$$R_m = P_0 \left[\frac{2}{\omega t_d} \sqrt{2\mu - 1} + \frac{2\mu - 1}{2\mu(1 + 4/\omega t_d)} \right]^{-1} \quad (2)$$

where μ is the ductility ratio, P_0 is the peak pressure, t_d is the blast load duration, ω is the natural frequency of vibration.

ω is calculated by Equation (3)

$$\omega = \sqrt{K_e/M_e} \quad (3)$$

where K_e is the equivalent elastic stiffness, M_e is the equivalent mass.

The resistance R_m is also computed by Equation (4), shown as

$$R_m = K_e y_m / \mu \quad (4)$$

where y_m is the maximum mid-span displacement.

Then, Equation (2) is re-arranged as Equation (5) combined with Equations (3) and (4),

$$\frac{\omega^2 y_m M_e}{\mu P_0} = \left[\frac{2}{\omega t_d} \sqrt{2\mu - 1} + \frac{2\mu - 1}{2\mu(1 + 4/\omega t_d)} \right]^{-1} \quad (5)$$

Equation (5) shows that the natural frequency of vibration ω can be calculated if the performances y_m and μ are known. After the calculation of ω , parameters of blast-resistant function R_m and K_e are easily determined according to Equations (3) and (4).

If the blast load is rectangular long-time load, calculations of R_m and K_e are simplified as

$$R_m = \frac{2\mu P_0}{2\mu - 1} \quad (6)$$

$$K_e = \frac{2\mu^2 P_0}{y_m(2\mu - 1)} \quad (7)$$

If the blast load is impulse-controlled load, calculations of R_m and K_e are simplified as

$$R_m = \frac{I^2 \mu}{M_e y_m (2\mu - 1)} \quad (8)$$

$$K_e = \frac{I^2 \mu^2}{M_e y_m^2 (2\mu - 1)} \quad (9)$$

After the calculation of R_m and K_e , parameters of cross section could be designed [22]. Present study takes a simple supported RC beam as an example. The resistance R_m is given by Equation (10),

$$R_m = 8 M_u / l^2 \quad (10)$$

where M_u is the ultimate moment capacity at the mid-span, given by Equation(11),

$$M_u = \rho_1 f_{dy} b d^2 \left(1 - \frac{\rho_1 f_{dy}}{1.7 f'_{dc}} \right) \quad (11)$$

where f_{dy} is the dynamic yield stress of the longitudinal reinforcement, f'_{dc} is the dynamic concrete compressive strength, ρ_1 is the longitudinal reinforcement ratio, b is the width of beam, d is the distance from the extreme compression fiber to the centroid of the longitudinal tension reinforcement.

K_e is given by Equation (12),

$$K_e = \frac{384 E_c I_a}{5 l^4} \quad (12)$$

where E_c is the concrete modulus of elasticity, I_a is the average moment of inertia of the beam

given by Equation(13) [22].

$$I_a = 0.5(bh^3/12 + Gbd^3) \tag{13}$$

The coefficient G in Equation (9) is evaluated by Equation (14) [13], where E_s is the steel modulus of elasticity.

$$G = (3320.3\rho_1^3 - 181.98\rho_1^2 + 5.8624\rho_1) \left(\frac{E_s}{7E_c}\right)^{0.7} \tag{14}$$

Equations (6) ~ (10) are used to compute the design variables of cross section.

The stirrup reinforcement ratio is calculated by Equation (15) [23]

$$\rho_2 = \frac{(V_u - V_c)}{\phi f_{dv} b d} \tag{15}$$

where V_u is the ultimate shear force, V_c is the shear capacity of the concrete, f_{dv} is the dynamic yield strength for shear reinforcements, ϕ is the capacity reduction factor.

NEW DESIGN PROCEDURE FOR RC MEMBERS

Equations (3)~(9) show that the maximum displacement y_m and the ductility ratio μ can be calculated using R_m and M_u . Therefore, the designers control the objective performances y_m and μ by the design of R_m and M_u . The new design procedure is shown in Figure 4. Compared with Design procedure A and B, both maximum displacement and ductility ratio are controlled without increasing the design loops.

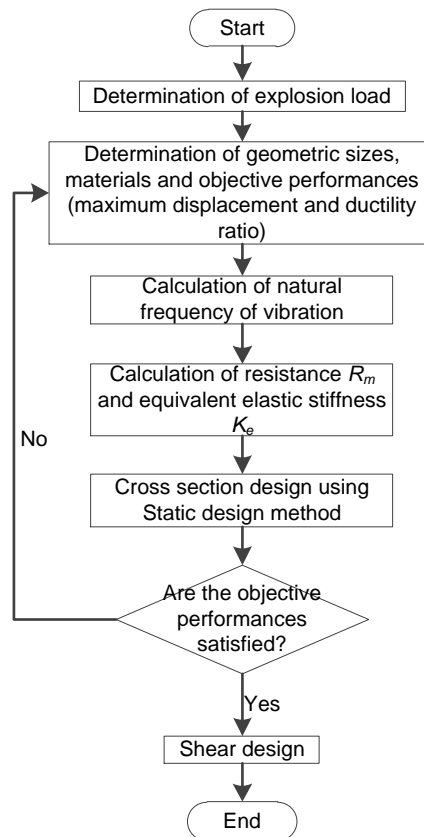


Fig. 4 – New design procedure

For convenience of design, non-dimensional P-I diagrams are proposed in Figure 5. The black lines represent the ductility ratio μ . The red lines represent the maximum displacement y_m . Drawing method of the non-dimensional P-I diagrams are described as follows.

First, non-dimensional impulse and pressure are defined as

$$I = \frac{\omega}{R_m} I_m = \frac{\omega}{R_m} \frac{P_0 t_d}{2} \tag{16}$$

$$P = P_0 / R_m \tag{17}$$

Then, Equation (5) is re-arranged as Equation (18)

$$I = \frac{AP+B+\sqrt{A^2P^2+CP+D}}{-AP+A+1} P \tag{18}$$

where $A = -2\mu$, $B = -2\mu\sqrt{2\mu-1}$, $C = 4\mu^2\sqrt{2\mu-1}$, $D = 2\mu^3 - \mu^2 - 8\mu^2\sqrt{2\mu-1} + 4\mu\sqrt{2\mu-1}$.

According to Equation (18), black P-I curves are obtained.

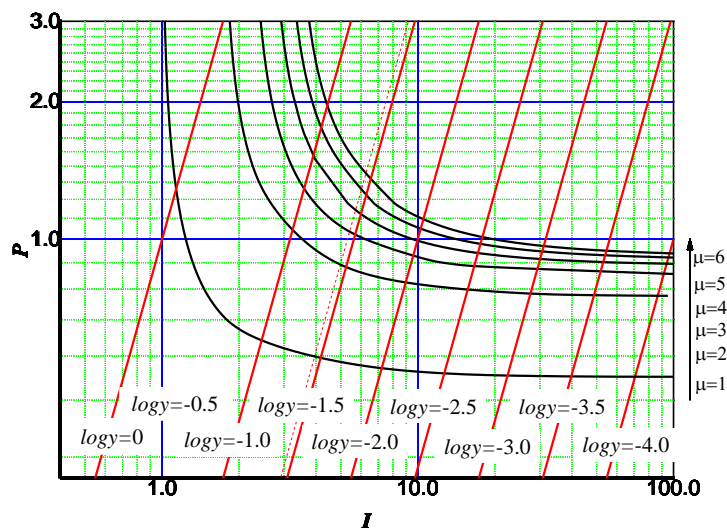


Fig. 5 – Non-dimensional P-I diagram

According to Equation (16) and Equation (17), Equation (19) is gotten as follows

$$P/I = P_0 / (\omega I_m) \tag{19}$$

Because

$$P = P_0 / R_m = \frac{\mu P_0}{\omega^2 M_e y_m} \tag{20}$$

Then, Equation (21) is obtained based on Equation (19) and Equation (20).

$$P/I^2 = y' \tag{21}$$

where

$$y' = y_m M_e \frac{P_0}{\mu I_m^2} \tag{22}$$

According to Equation (21), red P-I curves are obtained.

A simple example is present here to describe the design procedure in detail. A simply support RC rectangular beam needs to be designed. The design variables is the width b , the height h and the longitudinal reinforcement ρ_1 . The other parameters and corresponding values are listed in Table 1.

Tab. 1 – Design parameters and corresponding values

Parameters	f_c	f_y	$bh \times l$	ρ_c	d'	μ	y_m	P_0	t_d
Values	14.3MPa	300MPa	0.06×4m	2400kg/m ³	20mm	6	0.0349m	15.0kN/m	60ms

Step 1 is to calculate y' according to Equation (22).

Step 2 is to find the intersection point (I', P') of P-I curves according to the value of y' and μ . From Figure 4, we find that the intersection point $(I', P') \approx (5.5, 1.4)$.

Step 3 is to computer R_m and K_e according to Equation (19). $R_m = 10.7 \text{ kN/m}$, $K_e = 1777.8 \text{ kN/m}^2$.

Step 4 is to calculate design variables based on values of R_m and K_e using Equations (10)~(14). $b = 0.191, h = 0.314, \rho_1 = 0.038$.

The dynamic response of the designed RC beam is shown in Figure 6. The calculated results, $y_m = 0.0336\text{m}$ and $\mu = 5.9$, are quite close to the objective performances. This means that the new design procedure has good control of y_m and μ .

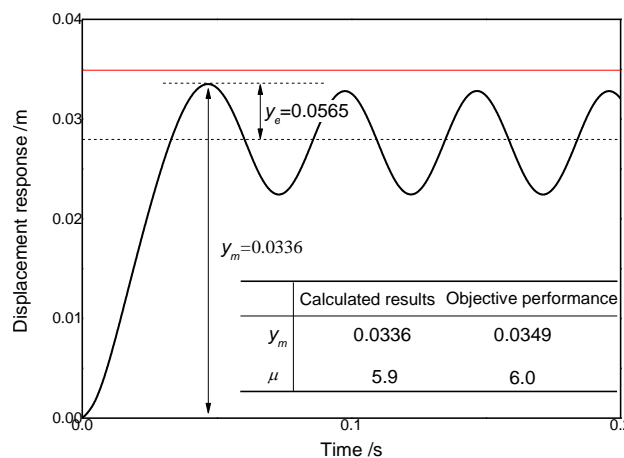


Fig. 6 – Dynamic responses of RC beam

APPLICATION OF NEW DESIGN PROCEDURE IN THE PBBD PROCEDURE

The object of PBBD procedure is to control the performances of structures under blast load to satisfy the request of building owners. However, it is hard to predict the magnitude of blast hazards [24]. The recommend method is to assume some blast scenarios which may be determined by building owners, decision maker or engineers [25]. Several blast scenarios are very necessary for design, because only one blast scenario may be unsafety, which will be illustrated in the following part.

The procedure of PBBD for RC members is shown in Figure 7. The new design procedure is used after the determination of blast load and the corresponding objective performances. The blast loads should represent the possible explosive scenarios and be determined using explosive

possibility analysis. The objective performances represent the loss expectation and determined using loss risk analysis. In order to clearly describe the application of the new design procedure, present study skips the explosive possibility analysis and the loss risk analysis.

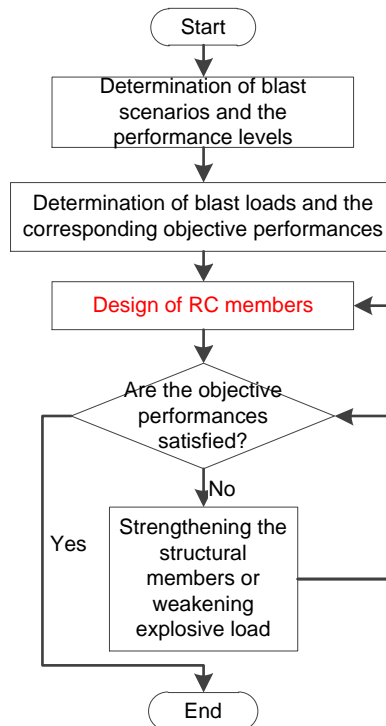


Fig. 7 – Procedure of PBBD for RC members

The new design procedure is used to design the RC beams according to several blast loads and objective performances. The key point is to find the relations between (R_m, ω) and (y_m, μ) . Steps are listed as follows:

Step 1 is to find the (P_i, I_i) ($i=1, 2, 3\dots$) corresponding to the objective performance μ using Figure 5;

Step 2 is to calculate the (R_{mi}, ω_i) corresponding to (P_i, I_i) ;

Step 3 is to find the (P_j, I_j) ($j=1, 2, 3\dots$) corresponding to the objective performance y_m using Figure 5;

Step 4 is to calculate the (R_{mj}, ω_j) corresponding to (P_j, I_j) ;

Step 5 is to determine the ranges of (R_m, ω) which satisfies the objective performance;

Step 6 is to determine a design point (R_m, ω) ;

Step 7 is to design the RC members and check performances. If the objective performance is not satisfied, return to Step 6.

A simple design example is presented here. Parameters of a simply supported RC beam are shown in Table 2. After the explosive possibility analysis and loss risk analysis. We assume that three reverse triangle blast load are considered, listed in Table 3. y_m and μ are both used as performance index. The assumed performance levels are listed in Table 4. The objective performance is shown in Table 5. The objective performance is that the RC beam should satisfy Performance level 1 under blast load 1, simultaneously satisfy performance level 2 under blast load 2 and satisfy performance level 3 under blast load 3 at the same time.

Tab. 2 – Parameters of RC beam

Parameter	f_c	f_y	$bh \times l$	ρ_c	d'
Value	14.3MPa	300MPa	0.06×4m	2400kg/m ³	20mm

Tab. 3 – Three blast loads

	Blast load 1	Blast load 2	Blast load 3
Reflected peak pressure/ (kN/m)	20	30	40
Duration time/ ms	20	30	40

Tab. 4 – Performance levels

	y_m	μ	Description
Performance level 1	$\leq 0.020m$	≤ 4	Superficial damage
Performance level 2	$\leq 0.035m$	≤ 5	Moderate damage
Performance level 3	$\leq 0.054m$	≤ 6	Heavy damage

Tab. 5 – Objective performance

		Performance level		
		Performance level 1	Performance level 2	Performance level 3
Blast loading	Blast load 1	√		
	Blast load 2		√	
	Blast load 3			√

Using the proposed design method and the corresponding non-dimensional P-I diagrams, the contour lines of y_m and μ are for blast loads 1~3 are shown in Figure 8.

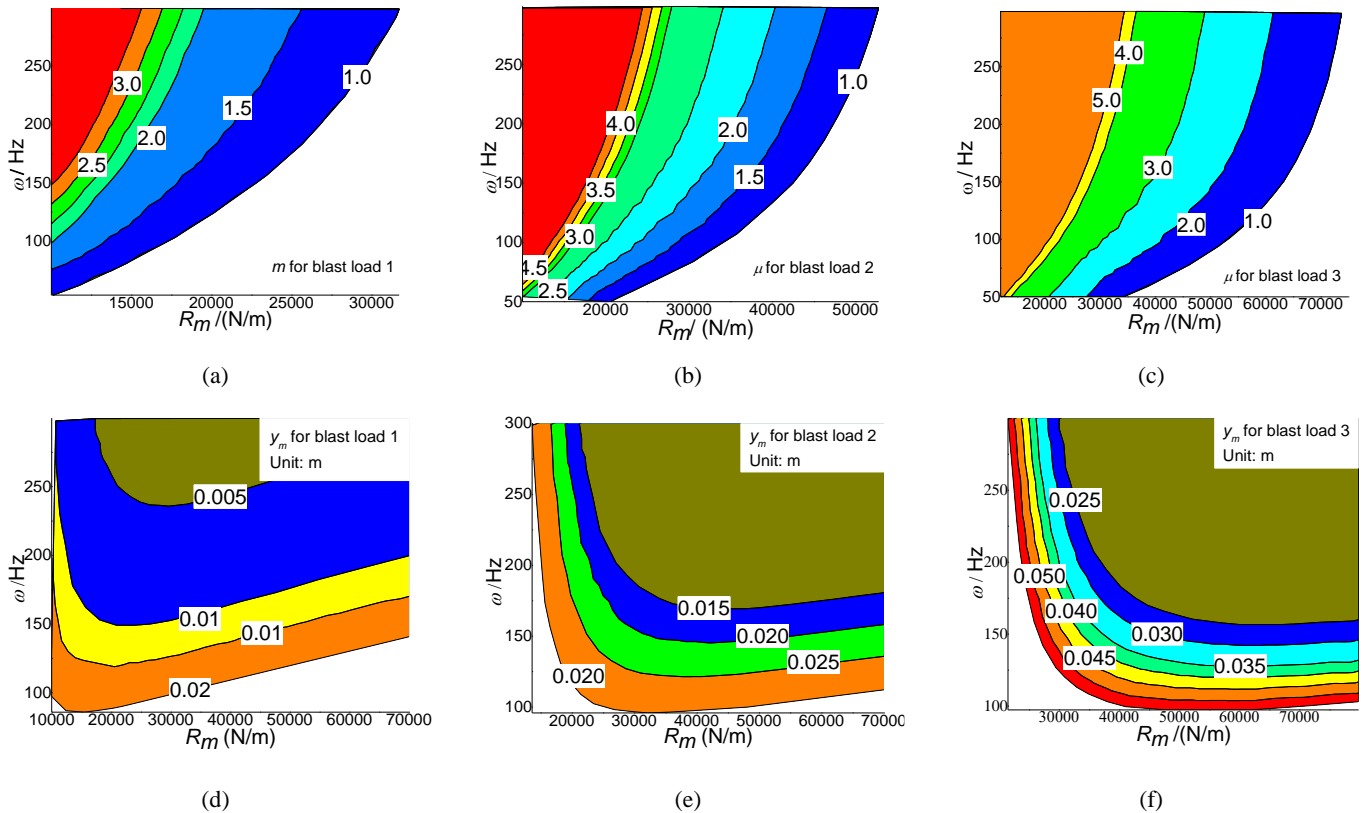


Fig. 8 – Contour lines of y_m and μ for different blast loads

According to the objective performance, the design ranges of (R_m, ω) are shown in Figure 9. And a design point $(R_m = 30 \text{ kN/m}, \omega = 150 \text{ Hz})$ is selected. Then, the design results $b = 0.19\text{m}$, $h = 0.31\text{m}$ and $\rho = 0.012$ are obtained using Equations (10)~(14).

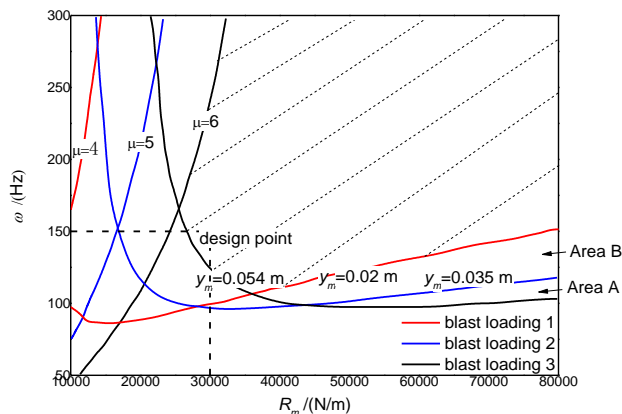


Fig. 9 – Design range of R_m and ω

Figure 9 shows the necessity of using several blast loads to design the RC members. The designers usually use a larger blast load to design and believe that the designed result can satisfy the objective performances under smaller blast load if the objective performances under larger blast load are satisfied. However, the design points in area A do not satisfy the objective performances under blast load 1 and 2 but satisfy the objective performances under blast load 3, even blast load 3 is the largest one. In the area B, the design points do not satisfy the objective

performances under blast load 1 but satisfy the objective performances under blast load 3. This indicates that using several typical blast scenarios to design the RC members is more safety.

The performances of designed RC beam are check out using SDOF method. Calculated results are listed in Table 6. It shows that the objective performances are well satisfied.

Tab. 6 – Actual performance of the designed beam

	y_m	μ
Performance level 1	0.010m≤0.020m	1.0≤4
Performance level 2	0.019m≤0.035m	1.6≤5
Performance level 3	0.046m≤0.054m	3.8≤6

CONCLUSIONS

The common used design procedures of RC members have many design loops, which adds much work to engineers and limits the development of PBBD procedure. Presented study proposed a new design procedure of RC members which has less design loops. The new design procedure is based on the SDOF method, which is widely accepted by designers. This indicates that the new procedure is convenient to use because SDOF is familiar to designers.

The new design procedure controls both the maximum displacement and the ductility very well. This means that the new procedure controls the performance well. For the convenience of design, non-dimensional design chart is proposed corresponding to the new design procedure. It shows that the new design chart is very convenient to design as well as to control the performance well.

The new design method is very suitable for the PBBD procedure. The application of the new design method in the PBBD procedure is presented in detail and explained using a design example. The example shows the importance of PBBD procedure because the PBBD procedure gives more safety design results than the common design methods.

REFERENCES

- [1] Allin C., 2000. Progress and challenges in seismic performance assessment. PEER newsletter, vol. 3(2): 1-3.
- [2] Ali R. M. and Louca L. A., 2008. Performance based design of blast resistant offshore topsides, Part I: Philosophy. Journal of Constructional steel research, vol. 64(9): 1030-1045.
- [3] Barbato M., Petrini F., Unnikrishnan V. U., and Ciampoli M., 2013. Performance-based hurricane engineering (PBHE) framework. Structural safety, vol. 45: 24-35.
- [4] Sharma H., Hurlbauss S. and Gardoni P., 2012. Performance-based response evaluation of reinforced concrete columns subject to vehicle impact. International journal of impact Engineering, vol. 43: 52-62.
- [5] Ciampoli M., Petrini F. and Augusti G., 2011. Performance-based wind engineering: towards a general procedure. Structural safety, vol. 33(6): 367-378.
- [6] Hamburger R. O. and Whittaker A. S., 2003. Considerations in performance-based blast resistant design of steel structures. In: AISC-SINY Symposium on Resisting Blast and Progressive Collapse, 1-10.
- [7] Yu R.Q., Fang Q., Chen L. and Yan H.C., 2016. Performance-based blast-resistant design of building structural components. Engineering Mechanics, vol: 33(11): 75-83.
- [8] Hall W.J., 1997. Seismic Design Methodologies for the Next Generation of Codes. Earthq. Spectra, vol 27(2): 379-380.
- [9] Hamburger R., Rojahn C., Moehle J., Bachman R., Comartin C. and Whittaker A., 2004. The ATC-58

project: development of next-generation performance-based earthquake engineering design criteria for buildings. In: the 13th World Conference on Earthquake Engineering, 1-15.

[10] Stewart M.G., 2018. Reliability-based load factor design model for explosive blast loading. *Structural Safety*, vol. 71: 13-23.

[11] Campidelli M., Tait M.J., El-Dakhakhni W.W. and Mekky W., 2015. Inference of blast wavefront parameter uncertainty for probabilistic risk assessment. *Journal of structural Engineering*, vol. 141(12): 04015062.

[12] Yu R.Q., Chen L., Fang Q. and Huan Y., 2018. An improved nonlinear analytical approach to generate fragility curves of reinforced concrete columns subjected to blast loads. *Advances in structural engineering*, vol. 21(3): 396-414.

[13] Olmati P., Petrini F. and Gkoumas K., 2014. Fragility analysis for the Performance-Based Design of cladding wall panels subjected to blast load. *Engineering structures*, vol. 78: 112-120.

[14] Nagata M., Beppu M., Ichino H. and Yashiro H., 2017. Proposal on risk assessment of reinforced concrete structures subjected to explosive loads, *International journal of protective structures*, vol. 8(3): 407-432.

[15] Asprone D., Jalayer F., Prota A. and Manfredi G., 2010. Proposal of a probabilistic model for multi-hazard risk assessment of structures in seismic zones subjected to blast for the limit state of collapse. *Structural safety*, vol. 32(1): 25-34.

[16] Yu R. Q., Chen L., Fang Q., Yan H. C. and Chen G. L., 2019. Generation of pressure–impulse diagrams for failure modes of RC columns subjected to blast loads. *Engineering failure analysis*, vol. 100: 520-535.

[17] Yu R.Q., Zhang D.D., Chen L. and Yan H.C., 2018. Non-dimensional pressure–impulse diagrams for blast-loaded reinforced concrete beam columns referred to different failure modes. *Advances in structural engineering*, vol. 21(14): 2114-2129.

[18] Taha M.M.R., Colak-Altunc A.B. and Al-Haik M., 2009. A multi-objective optimization approach for design of blast-resistant composite laminates using carbon nanotubes. *Composites part B-engineering*, vol. 40(6): 522-529.

[19] Yu R.Q., Zhang D.D. and Yan H.C., 2017. Embodied Energy and Cost Optimization of RC Beam under Blast Load, vol. 2017: 1907972.

[20] UFC 3-340-02, 2008. Structures to resist the effects of accidental explosions (Unified Facilities Criteria) 1943 pp.

[21] Standard GB 50038-2005, 2005. Code for design of civil air defence basement (Ministry of construction of the People's Republic of China) 48 pp.

[22] Bounds W.L., 2010. Design of Blast-resistant Buildings in Petrochemical Facilities (ASCE Publications) 311 pp.

[23] Rong H.C. and Li B., 2008. Deformation-controlled design of reinforced concrete flexural members subjected to blast loadings. *Journal of structural engineering*, vol. 134(10): 1598-1610.

[24] FEMA 452, 2005. Risk Assessment: A How-To Guide to Mitigate Potential Terrorist Attacks against Buildings (Federal Emergency Management Agency) 248 pp.

[25] ASCE Standard ASCE/SEI 59-11, 2012. Blast Protection of Buildings (American Society of Civil Engineers) 126 pp.

REMEDIATION TECHNOLOGY OF CLOCHE REPLACEMENT FOR WW2 FORTIFICATION IN THE CZECH REPUBLIC

Jiří Pazderka¹, Michal Ženíšek¹, Tereza Pavlů¹, Pavel Reiterman², Ondřej Holpaček²

1. CTU in Prague, Faculty of Civil Engineering, Department of Building Structures, Thákurova 7, Czech Republic; jiri.pazderka@fsv.cvut.cz
2. CTU in Prague, Faculty of Civil Engineering, Experimental Centre, Thákurova 7, Czech Republic

ABSTRACT

Nowadays many parts of the Czechoslovak border fortification built in 1935 – 1938 have been sold to the private owners who want to reconstruct it. One of the biggest problems while reconstructing these objects is missing cloches. The aim of this study is to find solution of this problem. Authors wanted to offer the owners (usually clubs of military history) authentic design of the cloche for low cost, high durability and full functionality of the cloche that enables installation of original weapons.

A result of the work was a development of a technical solution of the cloche consisting of a replica of the upper part made of reinforced concrete in combination with lower part made of concrete. This unique technical solution was confirmed as an utility model CZ32920(U1). Remediation measure was approved by the team at the pillbox T-S 20 in Červený Kostelec in 2019.

KEYWORDS

Cloche, WW2, Pillbox, Remediation, Concrete

INTRODUCTION

Cloches were typical elements of the reinforced concrete fortifications built in Europe in the 1930s and 1940s [1,2]. We can find most of them in the objects of Maginot Line (Figure 1) which was built from 1929 till the German's Nazis troops attacked France in May 1940 [3,4]. Czechoslovak cloches made in 1937 – 1938 were inspired by the French pattern however, their construction was a bit different. While Sudetenland was annexed to Germany (October 1938), there were almost 400 pieces of cloches (mostly types AJ-S-N and AJ-S-D used for light or heavy machine guns) in the objects of the heavy blockhouses built between 1936 and 1938[6]. Most of them were removed and the steel was used for war production of Nazi Germany [7]. The cloches were mostly removed by using explosives so the fortresses were damaged (Figure 2).



Fig. 1 – Cloche in the object of Maginot Line in France.



Fig. 2 – Damage of the pillbox by the explosive used for cloche removal during occupation by Nazi Germany in 1939-1945 (pillbox N-S 84 „Voda“ in Náchod, Czech Republic)

Motivation

Missing cloches in the objects of the Czechoslovak heavy fortification are one of the biggest problems while reconstructing the objects by their owners, mainly military history clubs. The clubs cannot afford to cast an exact replica in a steel plant, the price of one cloche is 2,5 million CZK. The weight of the steel cloche (AJ-S-N) is 20 tons so its transport and placement to the objects that are usually situated in hardly accessible places would cost a lot of money too.

The clubs usually solve this problem by making replicas from cheap materials as wood with covering upper layer or metal sheet. Such solutions are not long lasting, after 2 or 3 years there are leaks of water to the constructions that cause deformation of the scale model. It is not possible to put original weapons to the loophole of the cloche and demonstrate shooting during excursions (kickback while firing machine gun would damage the replica) which is another disadvantage of the cheap solution.

PRINCIPLE OF REMEDIATION TECHNOLOGY

Based on the problems mentioned above, the team of the project NAKI II DG18P02OVV063 set a goal to find a solution which would offer:

- 1) authentic design of the cloche (not only form outside but also from the inside)
- 2) low cost, friendly for the military history clubs
- 3) long life of the solution
- 4) full functionality of the cloche construction allowing the installation of the original weapons and demonstration fire for the visitors of the fortress museum.

The result of the work was a development of the technical solution of the cloche consisting of a replica of the upper part made of reinforced concrete in combination with lower part made of concrete. This unique technical solution was confirmed as a utility model CZ32920 (U1) at Czech Industrial Property Office on 4. 6. 2019 [9].

Replica of the upper part of the cloche is prefabricated reinforced concrete element (Figure 4) imitating upper visible part of the cloche, however it lacks the massive original lower part (Figure 3) which is recessed into the fortress construction. The reinforced concrete element is smaller than the original cloche, thanks to this solution its height is half, but the parts visible from outside are as big as the original element. Due to the fact that the placement of this element will be made together with concreting the damaged part of the fortress, it is possible to prepare the round shaped gap that follows up the element (concreting substitutes the lower part of the cloche).

The original shaft has been preserved in case of the fortress where was no time for installing the cloche in 1938, so the part of the fortress was not damaged by the explosives. In this case the element will be placed on the concrete part of the shaft which replaces the lower part of the cloche.

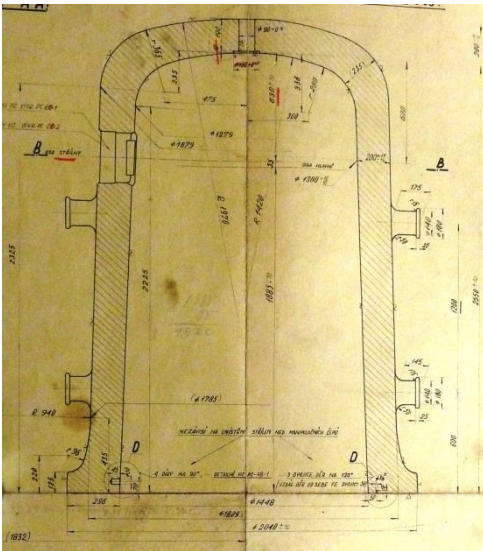


Fig. 3 – Original cloche type AJ-S-D (drawing from 1937 AČR - VÚA/VHA)

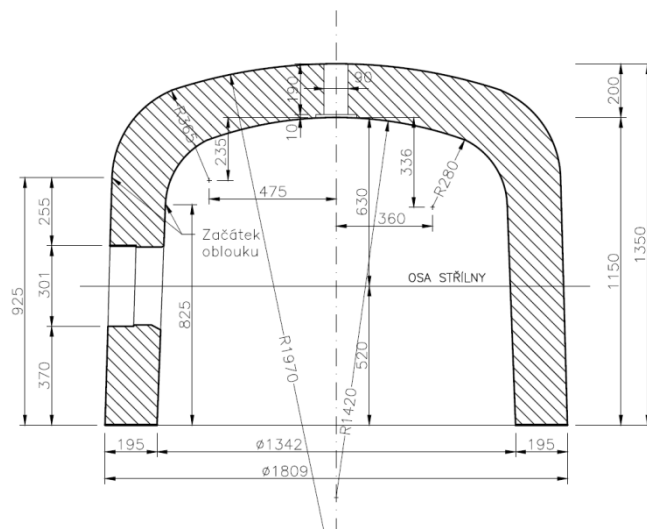


Fig. 4 – Replica of the upper part of the cloche AJ-S-D developed within the project.

It is possible to manipulate with the replica by ordinary lifting tools because its weight is only 2,8 tons in comparison with the original steel cloche of 20 tons. It is due to the fact that the replica represents only upper part of the cloche which is visible from outside and it is not made of steel but concrete. Thanks to the massive construction of the element it looks authentic also from the interior (in contrast with the wooden ones) and it is possible to use original machine gun for demonstration fire for visitors of the fortress museum. The surface of the replica is painted by original colour to ensure full authenticity. The paint continues also to the wall of the circular shaft which is a part of the newly concreted construction and reaches to the edge where the lower part of the original cloche was. The painting makes almost perfect impression of the internal appearance of the original cloche construction. The cloche is also painted by camouflage colour from outside, which makes the original appearance from 1930s.

EXPERIMENTAL APPLICATION

The technical solution of the cloche developed within the project NAKI II DG18P02OVV063 was tested on the pillbox T-S 20 „Pláň“ situated close to Červený Kostelec in Hradec Králové region in the Czech Republic in October 2019. See Figures 5 and 6.



Fig. 5 – Western wing of the pillbox T-S 20. Part for placing the cloche AJ-S-D replica is marked (shaft is covered by wooden construction, which will be removed).



Fig. 6 – Preserved original shaft from 1938 in the western wing of the pillbox T-S 20.

Construction of the pillbox T-S 20 was stopped in September 1938 exactly before placing the cloche (the concrete construction was finished and the cloches were prepared at the railway station in nearby town Náchod). After Munich Agreement, when the Sudetenland was annexed by Germany, the pillbox remained at the German's part of a new border. As the cloches were never placed to the pillbox, the construction was not damaged by explosives and the original shafts remained preserved. There should have been 3 cloches of different type in this pillbox (1xAJ-S-D for heavy machine gun, 1xAJ-S-N for light machine gun and 1 x observational cloche AJ-P).

Owner of the pillbox, Military History Club TS- 20, decided to reconstruct the AJ-S-D type of the cloche in the western wing of the pillbox so they asked the project team NAKI II DG18P02OVV063 from the Faculty of Civil Engineering for help. Due to this fact the replica of upper part of the cloche was designed as a type AJ-S-D (method could be used also for creating the AJ-S-N cloche type, which differs from AJ-S-D type only in a shape and position of loophole gaps).

MATERIALS AND METHODS

It was necessary to develop a unique manufacturing process for making the upper part of the reinforced concrete cloche replica, because nothing similar has been realized yet.

Molds

Two specially developed molds were a basic for the manufacturing process of the reinforced concrete element. Outer reusable fiberglass mold (Figure 9) was made on the polystyrene backing (cupola) with special surface adjustment allowing lamination. For easier removal after concreting the mold is composed of two parts. Inner mold was made of polystyrene with specially paved surface, there were also two molds for loopholes (Figures 7, 8). This inner mold is disposable (it was damaged after formwork). In the future there is a plan to make a

reusable mold consisting of two parts as well as in the case of the outer mold. Production of the complicated molds was made by external suppliers and was based on the documentation prepared by the project team NAKI II DG18P02OVV063. Size of the reinforced concrete prefabricated element (as well as the size of both molds) is determined exactly according the project documentation of the cloche from 1937. We got the documentation in the Military Historical Archive of the Czech Republic. Production of the reinforced concrete element took place in the laboratories of the CTU in Prague, Faculty of Civil Engineering

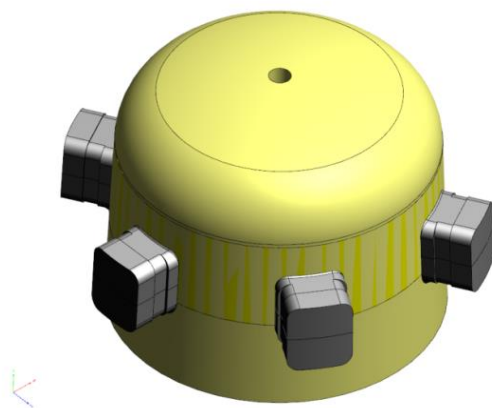


Fig. 7 – 3D model of inner mold



Fig. 8 – Assembly of reinforcement on the inner mold in the laboratories of the Faculty of Civil Engineering CTU in Prague.

Concrete

Lightweight concrete mixture of specification LC40/44 D2.0 XF2 which well declares required level of compressive strength was designed for the production of the element. The lightweight concrete had to be used due to limited manipulation technique during demoulding and especially during placing under complicated condition. Hence, the maximum weight of an entire element could be 2.0t. The concrete consists 400 kg/m³ of common Portland cement CEM I 52.5 R and addition of milled limestone as a filler for higher dense of concrete. The water-cement ratio was 0.40. The superplasticizer was used to improve the consistency of a fresh mixture. The artificial lightweight aggregate Liapor 2-10mm was used. Total volume of the lightweight aggregate was approximately 20% of the mixture. The mixture was produced in one batch to attain ideal homogeneity; hence the restarting agent was dosed to postpone the setting time.

The lightweight aggregate Liapor 2-10mm was used as a partial replacement of natural aggregate to achieve required level of bulk density, which should be below 2000kg/m³. Liapor is a natural clay product. The raw clay is burned in a rotary kiln at a temperature of approximately 1200 °C. The clay beads expand, resulting in a porous, air-filled Liapor. The water absorption of Liapor aggregate is more than 10 times higher in comparison with a natural aggregate, which negatively influence especially workability of fresh concrete. The freeze-thaw resistance of Liapor aggregate did not decrease with high water absorption due to the specific porous system inside the particles. The properties of natural aggregate were verified in the laboratory to compare with Liapor aggregate. The properties of used aggregate and its comparison – Liapor aggregate [10] and natural aggregate are shown in Table 1.

Table 1 - The properties of aggregate

Types of aggregate Properties	Natural aggregate	Liapor aggregate
Oven-dried particle density (kg/m ³)	2530	1190
Fines content (% _{mass})	0.1	
Water absorption capacity w ₆₀ (% _{mass})	0.6	9
Water absorption capacity w _{24h} (% _{mass})	1.7	15
Freezing and thawing resistance (% _{mass})	< 1	< 2

The consistency of fresh mixture was controlled in terms of CSN EN 12350-2. The examination of workability of fresh concrete was measured two times during the concreting, due to the expected decline of workability causing by high water absorption of used lightweight aggregate. In the beginning, the initial consistency was S5, which means slump exceed 210 mm, however, the consistency gradually got worse over time. At the end of the production, approximately after 3 hours, the slump was only 120 mm, what corresponds with the class of S3.



Fig. 9 – Fitting the outer mold part
(Laboratory of the Faculty of Civil
Engineering, CTU)



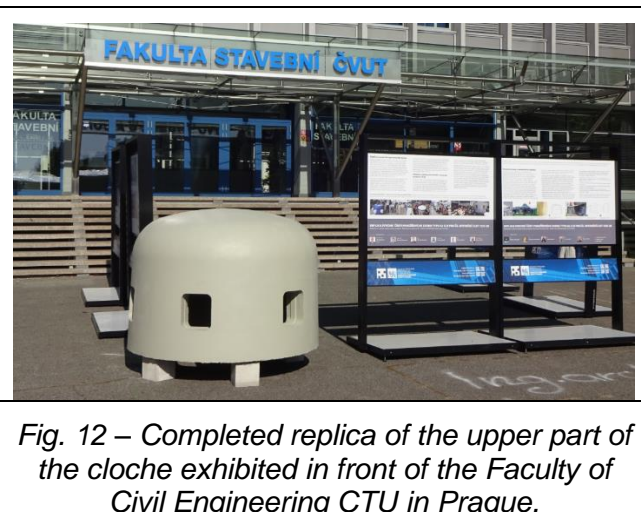
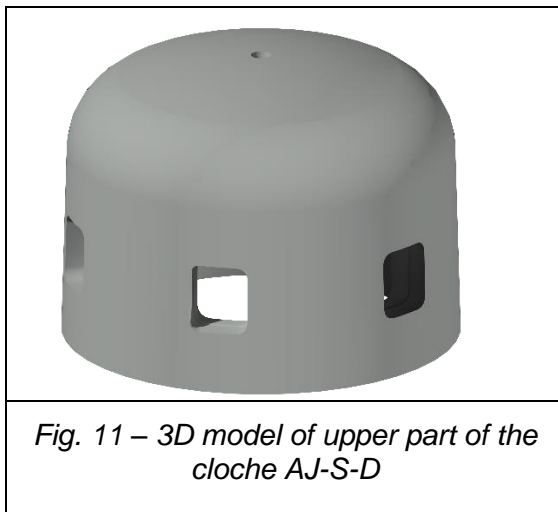
Fig. 10 – Concreting of the cloche after turning
the completed mold parts (Laboratory of the
Faculty of Civil Engineering, CTU)

Mechanical properties were investigated in terms of compressive strength in accordance with EN 12390-3 [11] by using cubic specimens of edge 150 mm. The compressive strength was controlled after 7 and 28 days; the attained values were gradually 49.6 and 54.0 MPa, respectively. The permeability of the hardened concrete was investigated in terms of water penetration test (EN 12390-8 [12]) after 28 days of curing. The achieved penetration was only 7 mm, which confirmed very impermeable structure of the concrete. The results of mechanical properties of lightweight concrete correspond with the results of previous studies [13-15]. The properties of the used concrete mixture are summarized in Table 2.

Table 2 - The properties of concrete

Properties	Slump (mm)	Density (kg/m ³)	Compressive Strength 7 days (MPa)	Compressive Strength 28 days (MPa)	Permeability (mm)
LC40/44 D2.0 XF2	210	1970	49.6	54.0	7.0

Completed prefabricated reinforced concrete element of the cloche type AJ-S-D was exhibited in front of the Faculty of Civil Engineering from 21. 9. till 11.10. 2019. There were also two posters describing the manufacturing process.



ON –SITE IMPLEMENTATION

In parallel with the production of the upper cloche part described in a previous chapter the lower part of the cloche was concreted directly in the pillbox T-S 20 (Figure 17). Inner surface of concreting was made with the help of a formwork with smooth surface so after the upper part of the cloche will be placed and everything will be finally painted by original colour, it will seem to be as high as the original cloche. Finally, the upper part of the cloche was moved from the faculty to Červený Kostelec and placed to the pillbox T-S 20 (Figures 18 and 19). Cement mortar with crystallization admixture (in 1938 it was only standard cement mortar) was used for connecting of both cloche parts. We used the crystallization admixture because of its ability to ensure the waterproof structure of the mortar, so it prevents leaking to the space between the cloches and the construction of the object. Features of the crystallization materials have been verified by many studies [16-20].

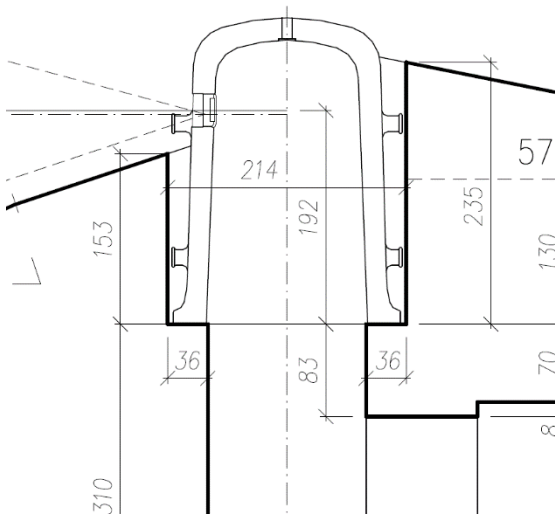


Fig. 13 – Original solution of the cloche type AJ-S-D from 1937 (part of the drawing cut through the pillbox)

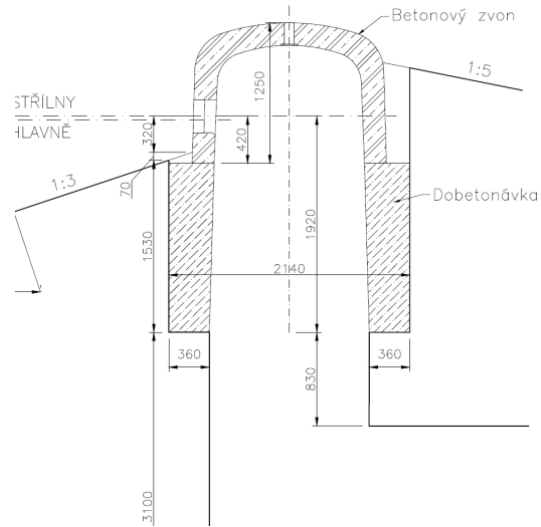


Fig. 14 – Technical solution of the reconstruction developed within the project (used at pillbox T-S 20)

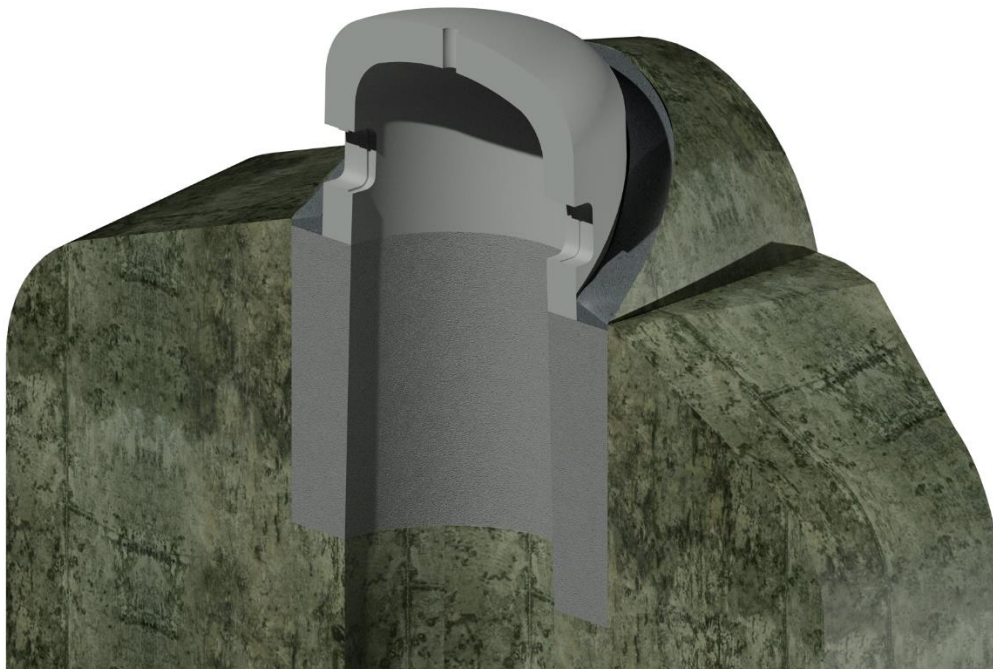


Fig. 15 – 3D model of remediation steps – fitting the replica of the upper part of the cloche on the concreted part of the shaft and final connection by cement mortar with cristalization admixture.

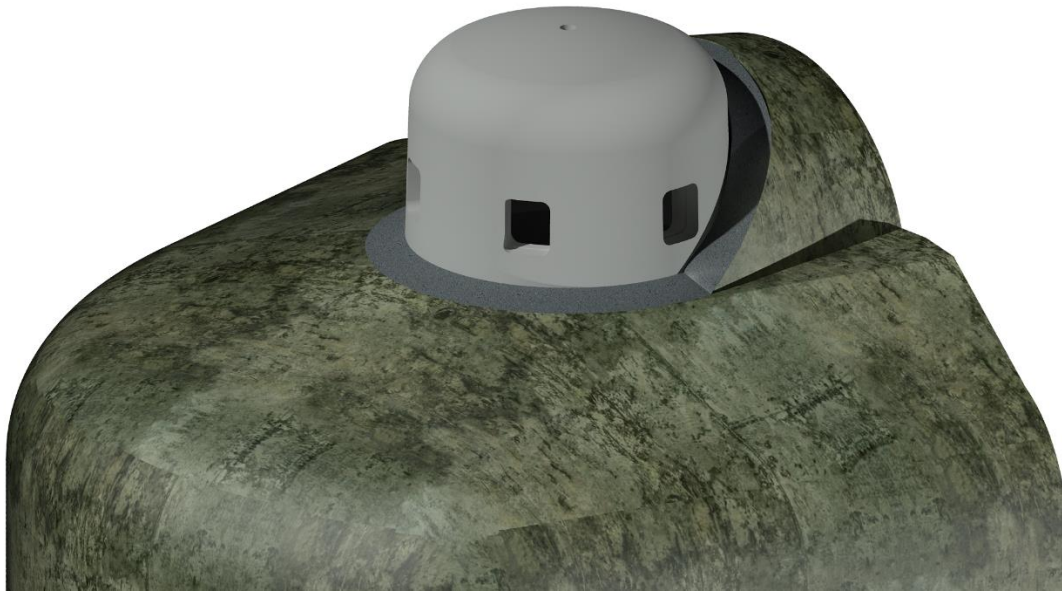


Fig. 16 – 3D model of a final state



Fig. 17 – Realization of the lower monolithic part of the cloche (pillbox T-S 20)



Fig. 18 – Placement of the replica and realization of concreting (pillbox T-S 20)



Fig. 19 – Current state of the pillbox T-S 20 (April 2020). Replica of the cloche was painted by the colour imitating metal, reconstruction of the surface plasters has not been made yet (due to COVID 19 pandemic)

CONCLUSION

Main phase of the reconstruction of the cloche AJ-S-D at the pillbox T- S 20 was successfully completed by placement of the prefabricated element and its monolithic connection with the construction of the object on 13. 10. 2019. Complete reconstruction is not finished. Following steps are: levelling and painting the inner surface of the shaft and especially overall external reconstruction of the plaster layer of the fortress, including the application of an original masking to the fortress and cloche. Then the replicas of loopholes will be placed as well as the gun carriage for the contemporary machine gun ZB type 37 which is a property of the historical club T- S 20. There will be also a functional shooting platform inside the cloche and a ventilation system. Everything was supposed to be finished in May or June 2020. However, the current crisis caused by the COVID 19 pandemic delayed the remediation measures.

The technical solution of the complete reconstruction of the cloche made at the pillbox T- S 20 in Červený Kostelec, was positively received by the military history clubs as well as the private owners of the fortresses in the Czech Republic. The team of the project NAKI II - DG18P02OVV063 has been already contacted by other owners of fortresses who are interested in the solution.

ACKNOWLEDGEMENT

This work was supported by the research project NAKI II - DG18P02OVV063.

REFERENCES

- [1] Kaufmann J.E., Jurga R.M.: Fortress Europe – European Fortifications of World War II. Da Capo Press, Perseus Book Group, 1999.
- [2] Grasser K., Stahlmann J.: Westwall, Maginot Linie, Atlantikwall. Leoni am Starnberger See: Druffell-Verlag, 1983.
- [3] Hughes J.M.: To the Maginot Line. Cambridge, Mass: Harvard University Press, 1971
- [4] Wahl, J.B.: La Ligne Maginot en Alsace. Steinbrunn-le-Haut, France: Editions Rhin, 1987.

- [5] Rowe V.: The Great Wall of France. Putman and Sons, New York, 1961.
- [6] Ráboň M.: Přehled těžkého opevnění. Military Club Brno, Brno, 1994.
- [7] Stehlík E.: Lexikon tvrzí čs. opevnění 1935-38. FORT Print, Dvůr Králové nad Labem, 1992.
- [8] Lakosil J., Svoboda T.: Československé opevnění 1938. Mladá fronta, Praha, 2017.
- [9] Pazderka J., Pavlů T., Ženíšek M.: Prvek pro celkovou rekonstrukci poškozených částí historických železobetonových pevnostních objektů, užitiný vzor no. CZ 32920(U1), Praha. 2019.
- [10] Declaration of Performance – No 08, Liapor 6,5 2/10 [online], 2019, http://www.liapor.com/medien_en/lia_downloads/datei/129_dop08_liapor_65_210.pdf
- [11] EN 12390 - Testing hardened concrete, Part 3 - Compressive strength of test specimens. Standard, European Committee for Standardization, Brussels, 2019.
- [12] EN 12390 - Testing hardened concrete, Part 8 – Depth of penetration of water under pressure. Standard, European Committee for Standardization, Brussels, 2009.
- [13] Bobas, J.A., Gomes A.: Compressive behavior and failure modes of structural lightweight aggregate concrete – Characterization and strength prediction. *Materials & Design* [online]. 2013, 46, 832–841. doi:10.1016/j.matdes.2012.11.004
- [14] Dilli, M.H., Atahan N., Sengul C.: A comparison of strength and elastic properties between conventional and lightweight structural concretes designed with expanded clay aggregates. *Construction and Building Materials* [online]. 2015, 101, 260–267. doi:10.1016/j.conbuildmat.2015.10.080
- [15] Nahhab, A.H., Ketab A.K.: Influence of content and maximum size of light expanded clay aggregate on the fresh, strength, and durability properties of self-compacting lightweight concrete reinforced with micro steel fibers. *Construction and Building Materials* [online]. 2020, 233, 117922. doi:10.1016/j.conbuildmat.2019.117922
- [16] M. Al-Kheetan, M. Rahman, D. A. Chamberlain. Development of hydrophobic concrete by adding dual-crystalline admixture at mixing stage. *Structural Concrete* 19:1504–1511, 2018. doi:https://doi.org/10.1002/suco.201700254.
- [17] M. Al-Kheetan, M. Rahman, D. A. Chamberlain. A novel approach of introducing crystalline protection material and curing agent in fresh concrete for enhancing hydrophobicity. *Construction and Building Materials* 160:644–652, 2018. doi:https://doi.org/10.1016/j.conbuildmat.2017.11.108.
- [18] M. Al-Kheetan, M. Rahman, D. A. Chamberlain. Influence of early water exposure on modified cementitious coating. *Construction and Building Materials* 141:64–71, 2017. doi:https://doi.org/10.1016/j.conbuildmat.2017.02.159.
- [19] J. Pazderka, E. Hájková, M. Jiranek. Underground air duct to control rising moisture in historic buildings: Improved design and its drying efficiency. *Acta Polytechnica* 57:331, 2017. doi:https://doi.org/10.14311/AP.2017.57.0331.
- [20] P. Reiterman, V. Baumelt. Long-term sorption properties of mortars modified by crystallizing admixture. *Advanced Materials Research* 1054:71–74, 2014. doi:https://doi.org/10.4028/www.scientific.net/AMR.1054.71

STUDY ON THE PERFORMANCE OF HIGH-MODULUS ASPHALT CONCRETE PAVEMENT IN EXTREME CURVES OR STEEP SLOPES OF TRUNK HIGHWAY

Honglei Zhang, Mingrui Yang, Youcheng Ma

*Beijing Xinqiao Technology Development Co., Ltd, Beijing, 100088, China;
765310906@qq.com, 1391920813@qq.com, 438287003@qq.com*

ABSTRACT

With the purpose of the project, we determined the performance of high modulus asphalt concrete (HMAC) pavement in sharp curves or steep slopes of the trunk highway. We selected bending of road surface, bending and stretching strain at the bottom of surface layer, vertical compressive strain at the bottom of surface layer as research parameter index. By using the three-dimensional model analysis function of the finite element software ANSYS, the mechanical models of asphalt pavement with three different structures under the action of steep slope and heavy traffic are established. Firstly, the conventional asphalt pavement consists of 4cmAC-13 bituminous pavement (the top layer) and 6cmAC-20 bituminous pavement (the bottom layer). Then, the HMAC pavement 1 consists of 4cmAC-13 bituminous pavement (the top layer) and 6cmAC-EME14 bituminous pavement (the bottom layer). The HMAC pavement 2 consists of 6cmAC-EME14 bituminous pavement (the top layer) and 4cmAC-13 bituminous pavement (the bottom layer). Then we tried it out that for the deflection value, the HMAC pavement 1 was 5.34 percentage point reduced than the conventional asphalt pavement. At the same time, the HMAC pavement 2 was 6.95 percentage point reduced than the conventional asphalt pavement. So, it can significantly reduce the bending strain at the bottom of the surface layer by using HMAC as asphalt pavement structure. For the resistance to shear strain and vertical compressive strain at the bottom of the surface layer, the HMAC pavement 1 is the best. Then the HMAC pavement 2 follows and then the conventional asphalt pavement. The results show that the HMAC can significantly improve the overall stiffness of the pavement and reduce the bending, shearing and vertical strain. Meanwhile, it can also reduce the occurrence of wheel rut, upheaval, fatigue crack and other common diseases.

KEYWORDS

Asphalt pavement, Pavement performance, Mechanical model, High modulus asphalt concrete, Sharp curves or steep slopes

INTRODUCTION

High modulus asphalt concrete (HMAC) is a kind of pavement material with high modulus and good anti-fatigue performance. So it can effectively reduce the road thickness and save resources [1]. The concept of HMAC was first proposed by France. For the sake of solving the problem of

insufficient rutting resistance of asphalt pavement and insufficient base course stiffness, the concept of HMAC was first proposed by France [2-3]. According to the French “LPC Bituminous Mixtures Design Guide”, only the asphalt mixture that meet requirements of modulus (15°C , 10Hz, 0.02s) $\geq 14000\text{Mpa}$, richness modulus $> 3.4\%$ and rut depth (30000cycles) $< 7.5\%$ can be called the “durability high-modulus asphalt mixture”[4].

In recent years more and more attention has been paid to the research of HMAC in China. But the asphalt used is mainly low-mark asphalt, modified asphalt, etc. Some organizations such as South China University of Technology, Chang’an University, Jiangsu Transportation Institute, Liaoning Transportation Research Institute Co.,ltd experimental studied its high temperature performance, low temperature performance, moisture susceptibility and fatigue resistance. The problem is that the durability of the mixture is neglected in the pursuit of the increase of modulus.

BACKGROUND

The dependent subject is supported by transportation science and technology fund in Guizhou China. Trunk highway has a large volume of traffic and a high proportion of heavy vehicles in China. The consequence is that rutting, shifting, cracking and other diseases appear on the road too early. This has had a serious impact on the regional economy. The results show that the HMAC can be used to reduce the thickness of the surface structure and improve the durability [5]. So it is suitable for heavy load, steep slope, hot summer and cold winter [6].

We selected G326 in Zunyi as the test section. The width of the pavement is 12m, and the original pavement structure is: 25cm lime flying-ash+6cm bituminous concrete surface course of AC-16. Before construction, the asphalt pavement mainly exist ruts, pits, cracks, loose, peeling and other diseases. In order to ensure the calculation accuracy and reduce the computational workload, software ANSYS was used for modeling and analysis [7].

PREPARATION OF HIGH MODULUS ASPHALT MIXTURE

Aggregate

The pavement in extreme curves or steep slopes of trunk highway requires strong shear strain resistance.

The internal friction angle is positively correlated with the internal friction resistance between aggregates. It can be concluded that to improve the shear strain resistance of asphalt mixture, the internal cohesion and internal friction angle of the mixture should be improved. So we chose the aggregate with the characteristics of hard texture, rough appearance, embedded extruding force, and strong adhesive with asphalt. The aggregate should meet the requirements of form2D, angularity index, etc.

Form2d

Form2D is divided into four grades from 0 to 20. The smaller the value, the closer the two-dimensional shape is to the circle.

$$Form\ 2D = \sum_{\theta=0}^{\theta=360-\Delta\theta} \left[\frac{R_{\theta+\Delta\theta} - R_{\theta}}{R_{\theta}} \right] \tag{1}$$

In the formula: R_{θ} — The radius of the particle at the Angle θ

Δ_{θ} — Angular micro-increment

Form 2D test results of fine aggregate is just as Figure 1. The abscissa is form2D, and the ordinate is the cumulative of particles.

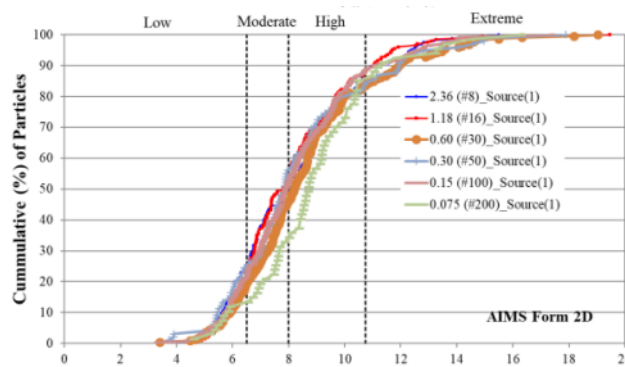


Fig.1 - Different particle size form2D test results

Angularity index

The angularity index is usually used to describe the concave and convex state of aggregate. Aggregate image measurement system (AIMS) was used to scan the shape profile of aggregate particles to identify the edges and corners. Then we can calculate the angularity index of each aggregate as the formula below.

$$GA = \frac{1}{n/3 - 1} \sum_{i=1}^{n-3} |\theta_i - \theta_{i+3}| \tag{2}$$

In the formula: GA — angularity index

θ — The angle direction of aggregate's vertex

n — Number of edges and vertices

i — edges and vertices of i

The test results of angularity index are shown in Figure 2.

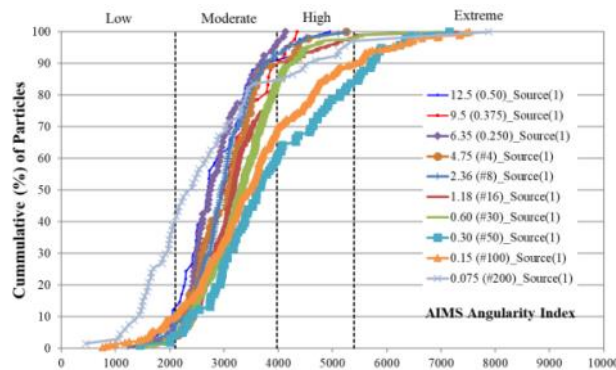


Fig.2 - Test results of angularity index

Hard asphalt

Hard asphalt is the key material of high modulus asphalt mixture. In this project, the hard asphalt produced in Luoyang is configured with 70# asphalt in a certain proportion. However, it is necessary to admixture or premix in advance before the construction. The testing results of various index of hard asphalt are as follows.

Tab.1 - Performance index of hard asphalt

Index	Unit	Results	Test method
penetration (25°C, 5s, 100g)	0.1mm	14	T0604-2011
Softening point (R & B)	°C	64.0	T0606-2011
Flash point	°C	321	T0611-2011
density (15°C)	g/cm ³	1.038	T0603-2011

High modulus asphalt mixture

According to the recommended grading range of French high modulus asphalt mixture EME2, the high modulus asphalt mixture suitable in extreme curves or steep slopes of trunk highway is designed with reference to the aggregate gradation and asphalt aggregate ratio (AAR) of previous engineering applications to determine the compaction characteristics of the mixture. The asphalt aggregate ratio is 5.6%. The aggregate gradation after sieving analysis test is just as Table 2.

Tab.2 - Aggregate gradation after sieving analysis test (The sieve hole, mm)

Aggregate gradation	The percentage of passing through the sieve hole (%)									
	0.075	0.15	0.3	0.6	1.18	2.36	4.75	9.5	13.2	16.0
EME14	6.9	9.2	12.1	17.6	24.5	35.3	49.4	75.0	98.0	100.0

PAVEMENT MECHANICAL MODEL IN EXTREME CURVES OR STEEP SLOPES

Effect of slope on mechanical properties of pavement

Loading mode: single side dual tires.

Model size: lateral 6.0m, driving direction 10.0m, depth direction 5.0m, represented by x axis, y axis and z axis.

Longitudinal slope: 6%.

Automotive braking force: $\phi = 0.5$.

Load distribution method: bzz-100 standard axial load was adopted in stress analysis, which was simplified as rectangular local load. The width of single track was 18.6cm, the length was 19.2cm, the net distance between two tracks was 12.8cm, and the pressure of single tire was 0.7MPa[8].

The influence of longitudinal slope on the pavement deflection is not obvious. The pavement deflection increases slowly with the increase of slope, from 0.14248mm at 0% to 0.14326mm at 6%, increasing by 0.55%.The result is shown in Figure 3.

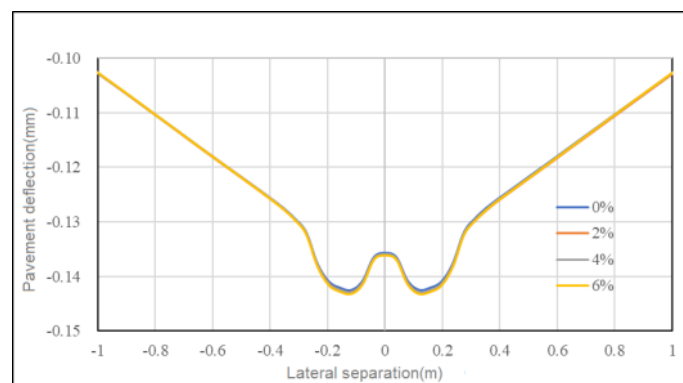


Fig.3 - The pavement deflection along the transverse direction of different slopes

With the increase of slope, the longitudinal shear strain at the bottom of the surface layer has small fluctuations, as shown in Figure 4.

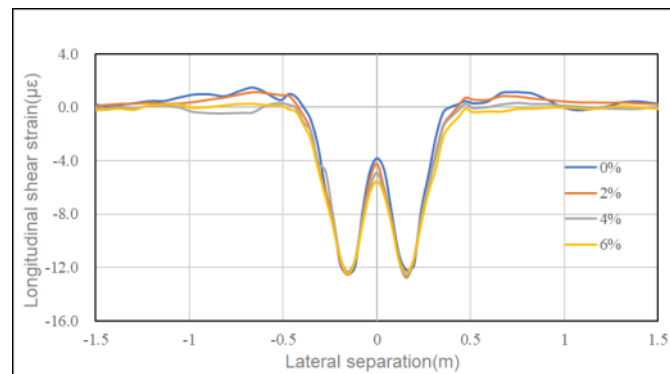


Fig.4 - The longitudinal shear strain along the transverse direction of different slopes

The vertical compressive strain fluctuates along the transverse direction. As the slope increases, the strain value increases, and the strain peak increases from 34.811 $\mu\epsilon$ of slope 0% to 36.561 $\mu\epsilon$ of slope 6%, with a small increase of 5.03%, as shown in Figure 5.

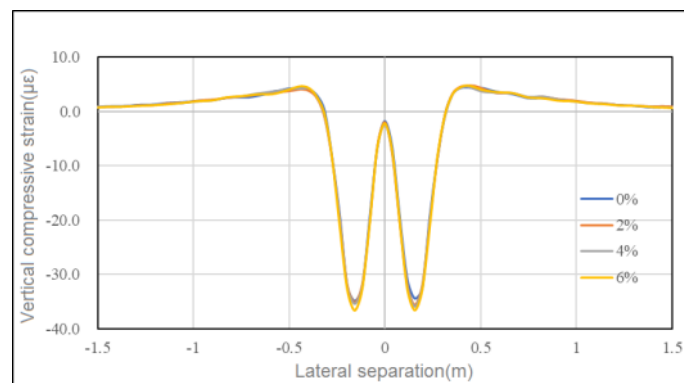


Fig.5 - The vertical compressive strain along the transverse direction of different slopes

The model of finite element

By using the three-dimensional model analysis function of the finite element software ANSYS, the mechanical model of asphalt pavement with three different structures under the extreme curve or steep slope is established and the corresponding conditions of asphalt pavement with three different structures are analyzed. The input parameters are in chapter effect of slope on mechanical properties of pavement. Figure 6 is the schematic diagram of the longitudinal section of extreme curve and steep slope, and Figure 7 is the finite element model.

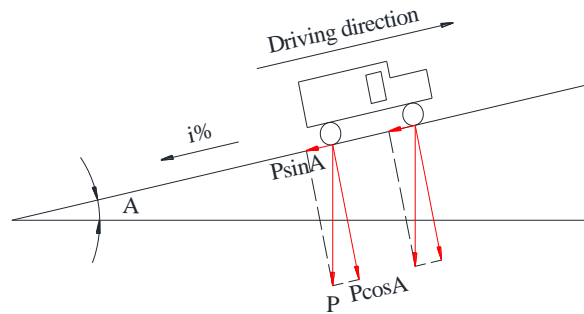
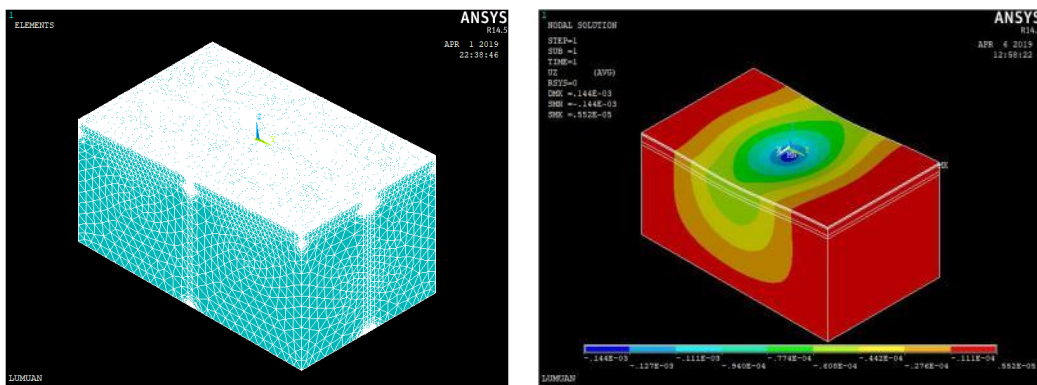


Fig.6 - Schematic diagram of vertical section of extreme curve and steep slope



(a)

(b)

Fig.7 - Finite element model and unit division

Pavement structure parameter

Table 3 ~ Table 5 show the structure composition and material parameters of conventional asphalt pavement and high-modulus asphalt pavement of trunk highway. The dynamic compression modulus under the condition of 20°C and 10Hz is adopted for the asphalt surface layer, the elastic modulus is adopted for the cement stabilized gravel base, the wet-adjusted rebound modulus is adopted for the graded gravel subbase, and the equivalent rebound modulus of the top surface is adopted for the soil subgrade. The mechanical effect of freezing-thawing cycle in the dry and wet state is fully considered.

Tab.3 - Materials and properties of the conventional asphalt pavement

Structural layer	Thickness(cm)	Elastic modulus (MPa)	Poisson ratio
Top layer:AC-13	4	8000	0.25
Following layer:AC-20	6	9000	0.25
Base: cement stabilized macadam	45	15000	0.25
Soil subgrade	-	50	0.4

Tab.4 - Materials and properties of the HMAC pavement 1

Structural layer	Thickness(cm)	Elastic modulus (MPa)	Poisson ratio
Top layer:AC-13	4	8000	0.25
Following layer:AC-20	6	16000	0.25
Base: cement stabilized macadam	45	15000	0.25
Soil subgrade	-	50	0.4

Tab.5 - Materials and properties of the HMAC pavement 2

Structural layer	Thickness(cm)	Elastic modulus (MPa)	Poisson ratio
Top layer:AC-13	6	16000	0.25
Following layer:AC-20	4	9000	0.25
Base: cement stabilized macadam	45	15000	0.25
Soil subgrade	-	50	0.4

Finite element analysis of asphalt pavement in extreme curve and steep slope

The pavement deflection

The peak value of surface deflection was 0.14326mm for the conventional asphalt pavement, and 0.13561mm of surface deflection of the HMAC pavement1, 5.34% lower than that of conventional asphalt pavement. The peak value of surface deflection of the HMAC pavement 2 is 0.1333mm, which is 6.95% lower than that of conventional asphalt pavement. Therefore, the

adoption of HMAC as the asphalt pavement structure can improve the overall stiffness and deformation resistance.

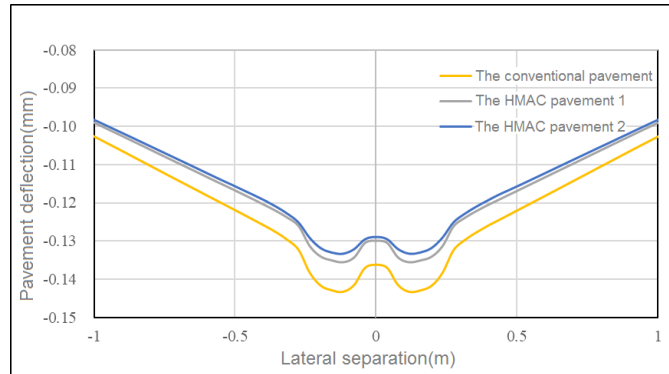


Fig.8 - The pavement deflection along the transverse direction of different pavement

Shear strain

It can be concluded that using HMAC as the asphalt pavement can significantly reduce the longitudinal shear strain of the pavement bottom surface, reduce the probability of bond failure between the surface layer and the base layer, and reduce the rutting, cladding, crack and other early failure phenomena of the asphalt pavement.

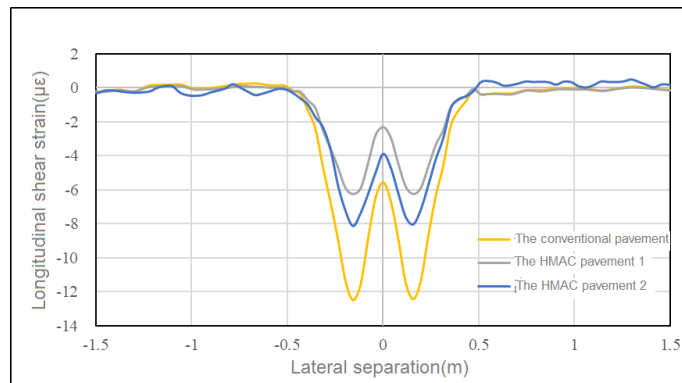


Fig.9 - The longitudinal shear strain along the transverse direction of different pavement

Vertical compressive strain of the bottom of the surface layer

Figure 10 shows that the vertical compressive strain at the bottom of HMAC pavement 1 is significantly reduced compared with the other two types of pavement, and its peak is 28.87% lower than conventional pavement and 23.18% lower than HMAC pavement 2. HMAC pavement 1 has better resistance to permanent deformation of the structure.

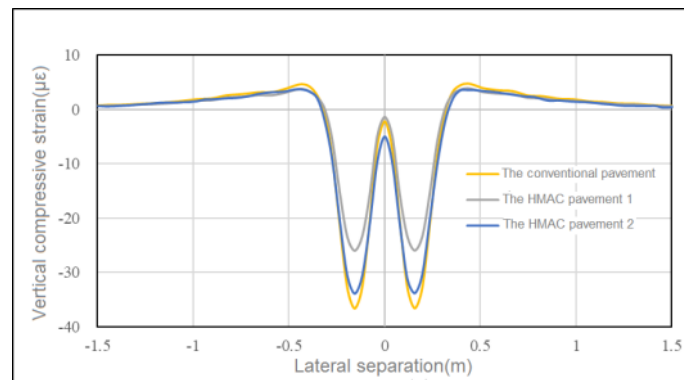


Fig.10 - The vertical compressive strain along the transverse direction of different pavement

THE ENGINEERING APPLICATION OF HMAC IN EXTREME CURVES OR STEEP SLOPES

Asphalt pavement construction

According to the characteristics of the road diseases, in order to improve the durability, rutting resistance, and considering test section cannot interrupt the traffic for a long time, we make a thorough treatment of these diseases at first and then adopted the overall plan of laying 6cm HMAC. So, there is not necessary to mill and resurface as a whole.

Production mix proportion

According to the available data, the final production mix proportion was determined after several tests, as shown in Table 6.

Tab.6 - Design of mix proportion

Materials & Quantity	Aggregate gradation after sieving analysis test (the sieve hole,mm) (%)									
	0.075	0.15	0.3	0.6	1.18	2.36	4.75	9.5	13.2	16
4#silo (30)	1.5	1.8	2.0	2.2	2.2	2.2	2.4	26.0	88.0	100.0
3#silo (20)	1.9	2.2	2.4	2.4	2.4	2.6	5.6	99.0	99.9	100.0
2#silo (15)	3.1	3.4	3.6	3.7	3.8	8.2	80.8	99.9	100.0	100.0
1#silo (33)	11.3	18.4	24.8	38.0	57.1	86.6	98.4	100.0	100.0	100.0
Mineral powder (2)	95.0	99.9	100.0	100.0	100.0	100.0	100.0	100.0	100.0	100.0
Aggregate gradation	7.0	9.5	11.8	16.3	22.6	33.0	48.4	77.6	96.4	100.0



Fig.11 - HMA pavement after construction

Field test of test section

The content of field test includes: core sample thickness and compaction, and the test results are shown in Table 7.



Fig.12 - Drilling core sample and the core sample

Tab.7 - Core sample thickness and compaction

No.	Stake mark	Core sample thickness(cm)	Measured relative density	Theoretical relative density	Compaction (%)
1	K388+955	5.5	2.372		96.0
2	K389+055	6.8	2.419	2.470	97.9
	Average	6.2	2.396		97.0

From the core sample, the distribution of coarse and fine aggregate is uniform and the gradation is reasonable. From the core sample compactness test results, the compactness all meets the requirements of interior design.

Tracking

Our research group kept track of the test section for a whole year. After a hot season and heavy traffic, there are no ruts and pits and other diseases. At the same time, after a low temperature season and heavy traffic, no spalling, loose, shrinkage, fatigue cracks and other diseases appeared. Road performance is satisfactory.

CONCLUSION

(a) The comparative analysis of the mechanical models of different asphalt pavement structures under the condition of extreme curves or steep slopes shows that adopting the HMAC as asphalt pavement can significantly reduce the longitudinal or transverse positive strain, and prevent fatigue cracking of asphalt concrete. At the same time, the resistance of pavement to fatigue cracking is improved, and the rutting, enveloping and cracking of pavement are reduced.

(b) Through the experimental research in the test section, the field compaction degree, uniformity, compaction performance and other indicators meet the design expectations. After one year of operation, under the action of high temperature and heavy vehicle, ruts and pits and other diseases did not appear, while under the action of low temperature and heavy vehicle, low-temperature cracks and loose diseases did not appear, showing good road performance. We could conclude that HMAC pavement has a good road performance.

(c) Through mixing ratio, model analysis, and evaluation after paving the test section, EME14 structure scheme can effectively improve the anti-cracking and anti-deformation capacity of asphalt pavement, meanwhile it improves road performance and improve driving comfort and safety. So EME14 structure scheme meets the use requirements in extreme curves or steep slopes.

REFERENCES

- [1] F.Moreno-Navarroa, M.Sol-Sánchez, M.C.Rubio-Gómez, M.Segarra-Martínez. The use of additives for the improvement of the mechanical behavior of high modulus asphalt mixes[J]. Construction and Building Materials, 2014, 70.
- [2] Corte JF. Development and Uses of Hard-grade Asphalt and of High-modulus Asphalt Mixes in France[J]. Transportation Research Circular, 2001, 503: 12-31.
- [3] Capit OSD, Picado-santos L. Assessing Permanent Deformation Resistance of High Modulus Asphalt Mixtures[J]. Journal of Transportation Engineering, 2006, 132(5): 394-401.
- [4] Delorme J L, De La Roche C, Wendling L. LPC bituminous mixtures design guide[M]. Paris: Central Laboratory for Bridge and Road, 2007.
- [5] Li HB. Experimental Study on Road Performance of High Modulus Asphalt Mixture[J]. Highway, 2011, (2): 123-126.
- [6] Huang XY, Sha AM, Zou XL, et al. Performance of High Modulus Asphalt Mixture and Applicable



Situation[J]. Journal of Highway and Transportation Research and Development, 2016, (12): 35-41.

[7] Xie TT. Long Steep Asphalt Concrete Pavement Structure Under Heavy Load Analysis [D]. Chongqing: Chongqing Jiaotong University, 2013.

[8] CCCC Infrastructure Maintenance Group CO.,LTD. Specifications for Design of Highway Asphalt Pavement: JTG D50-2017[S]. Beijing: China Communications Press CO., LTD, 2017.

ANALYSIS ON CONSTRUCTION DEFORMATION AND SUPPORTING STRUCTURE OF TWO-STEP AND THREE-SECTION EXCAVATION METHOD FOR SUPER LARGER SPAN HIGHWAY TUNNEL

Fujin Hou¹, Yanbin Luo², Qing Jiang³, Jianxun Chen², Tao Li³, Fangfang Dong²

1. *Shandong University, Research Center of Geotechnical and Structural Engineering, No. 27 Shanda South Road, Licheng District, Jinan City, Shandong Province, China; 188978807@qq.com*
2. *Chang'an University, Highway Institute, Middle Section of Nan Erhuan Road, Xi'an City, Shannxi Province, China; lyb@chd.edu.cn, 563303323@qq.com, chenjx1969@163.com*
3. *Shandong Expressway Jilai Intercity Highway Co., Ltd. 788 Jingshan Road, Lixia District, Jinan City, Shandong Province, China, 279415652@qq.com, 552126247@qq.com*

ABSTRACT

The super larger span tunnel is a common form of highway reconstruction and expansion projects in recent years. In order to determine the stability of tunnel structure of the two-step and three-section excavation method of the III-level surrounding rock mass of the super larger span highway, the field test method was adopted. Relying on the Laohushan Tunnel in Jinan, Shandong, China, the deformation and the structure performance of the super larger span tunnel in III-level surrounding rock mass are analyzed, and the safety of the tunnel and the support structure is evaluated on this basis. The results show that the maximum settlement of the arch section of the Grade III surrounding rock section is 12.5mm, and the maximum clearance convergence is 5.8mm. Both of them are much smaller than the design reserved deformation of 80mm. The maximum pressure of the surrounding rock is 0.091MPa, showing that the force acting on the supporting structure by surrounding rock mass is small. The inner and outer arched parts of the steel frame are subject to large stresses, and most of them are tensile stresses. The maximum stress of the steel frame is 283 MPa, and occurs at the inner side of right arch waist. Although the local stress exceeds the yield strength of the steel (235 MPa), it does not exceed its ultimate compressive strength of 400 MPa, and the tensile and compressive stress values of the other inner and outer parts do not exceed the yield strength. Mainly, the maximum stress appears on the left side wall, reaching 4.83 MPa, which is far less than the ultimate compressive strength of sprayed concrete (11.9 MPa). For super larger span highway tunnels, located in III-level surrounding rock mass, constructed by two-step and three-section excavation method, the initial support effectively controlled the tunnel deformation, the supporting structures were fully protected and the tunnel structure was stable. The super larger span tunnel is a common form in the road reconstruction and expansion project in recent years. In order to determine the stability of tunnel structure of the two steps and three excavation method of the III-level surrounding rock mass of the super larger span highway, the field test method was adopted. Relying on the Laohushan Tunnel, the deformation and the structure performance of the super larger span tunnel in III-level surrounding rock mass were analyzed. The results show that the maximum settlement of arch of the III-level surrounding rock mass is 12.5mm in super larger span highway tunnel, and the maximum clearance convergence is 5.8mm. Both of them are smaller than the design reserved deformation of 80mm. The maximum surrounding rock mass pressure is 0.091MPa, the force acting on the supporting structure by surrounding rock mass are small. The inner and outer arched parts of the

steel frame bear larger stress, and are mostly tensile stress. The maximum stress on inner side of the steel frame is 283 MPa, and occurs at the right arch waist. The maximum stress on the outer side of the steel frame is 184 MPa, and occurs at the vault. The steel frame plays an important role in the initial support, however the force does not reach the yield strength of the steel. The shotcrete is subjected to pressure, the maximum stress appears on the left side wall is 4.83 MPa, which is much smaller than the ultimate compressive strength of shotcrete of 25 MPa. So for super larger span highway tunnels, located in III-level surrounding rock mass, constructed by two-step and three-excitation method, the whole structure is stable.

KEYWORDS

Super larger span highway tunnel, Two-step and three-section excavation method, Deformation, Support structure stress, Analysis

INTRODUCTION

In recent years, with the rapid increase of highway transportation volume, the proportion of super larger span tunnel in the reconstruction and expansion project of highway tunnel are increasing. Many scholars in China have carried out related research on super larger span highway tunnel. For example, combined with actual engineering or numerical model analysis, Qu et al. (2008) and Liu et al (2015) researched the calculation method of surrounding rock mass pressure based on the traditional theoretical calculation method of surrounding rock mass pressure. Taken Guangzhou Longtoushan Tunnel as the engineering background, Zhou et al. (2009a, b; 2011) focused on the deformation rules of surrounding rock mass with time and excavation process of super larger span highway tunnel with the construction of double-side guide pit method. The regularity and the mechanical behaviour of the support system during tunnel construction are also researched. In addition, Yong Zhao, Shucui Li et al (2012) used the Lanyu Railway Liangshui tunnel as the engineering background to research the release process of surrounding rock mass load during tunnel excavation through geomechanical model experiments. According to monitoring and measurement analysis of the Kuiqi 2# tunnel, Jiang et al. (2010) researched the deformation and surrounding rock mass pressure distribution characteristics of the two-way eight-lane small clear distance highway tunnel. The relevant research about super larger span tunnel has achieved certain results at present, but there is no systematic technical specification for the design and construction of super larger span highway tunnel (Zhou et al. 2009b), resulting in the construction method and supporting parameters of super larger span highway tunnel engineering are mixed.

Given that super larger span four-lane highway tunnel structure has flat shape, large span and thin arch wall etc. characteristics, the deformation of surrounding rock mass and mechanical characteristics of support structure are more complicated than the conventional two-lane and three-lane tunnels. Based on the actual engineering, the rules of tunnel deformation, surrounding rock mass deformation and stress of supporting structure of the super larger span highway tunnel was analyzed, under different level of surrounding rock mass conditions with different construction method and supporting parameter. It is the necessary way to confirm reasonable construction method and supporting parameter of super larger span highway tunnel.

Up to now, we only have studies about larger span tunnel and super larger span tunnel with double-wall guide pit method, CRD method and other excavation (e.g. Xia et al. 2007; Gong et al. 2009; Sharifzadeh M. et al. 2013; Li et al. 2014; Zhou et al. 2017), there is almost no research on the construction of two-step three-section excavation method for super larger span tunnel.

METHODS

In this paper, using Laohushan Tunnel, the super larger span highway tunnel as the engineering background, the surrounding rock mass deformation discipline and support structure stress of the super larger span highway tunnel during the construction of the two-step and three-section excavation method of the III-level surrounding rock mass section was researched. Among them, the division of surrounding rock is based on China's *Specifications for Design of Highway Tunnels* (JTG 3370.1-2018).

Engineering survey

Laohushan Tunnel is located in Jinan, Shandong province, China, and is the first two-way eight-lane municipal highway tunnel in Shandong province. The tunnel spans two places, Lixia District and Shizhong District, Jinan. The entrance is located on the southwest side of Huangjin Shanshui County, south of the intersection of Tourism Road and Erhuan East Road, and the exit is located in Bandaoling Village, which is adjacent to the Erhuan Southeast Road as shown in Figure 1.

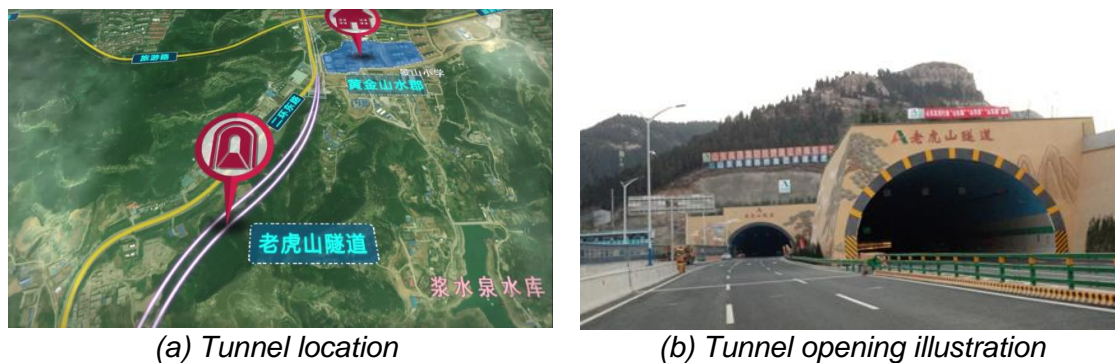


Fig. 1 – Laohushan Tunnel Overview

The maximum excavation span of a single tunnel is 20.08m and the maximum excavation height is 13.4m which belongs to super larger span highway tunnel. The right line of the tunnel is 1888m and the left line is 1740m. Construction started in March 2016 and completed in July 2017. It is the pivotal dominant engineering of the South Extension Project of the Second Ring Road of Jinan Link of Beijing-Shanghai Expressway.

Geological conditions

The fracture structure of the stratum passing through the Laohushan Tunnel is relatively developed, and it has a wide distribution and strong directionality, mainly in the northeast-southwest direction and southeast-northwest direction. The overall area stability is general. The entrance of the tunnel is located at the foot of the mountain. There is a residual layer of slope on the surface layer, and the thickness of the soil layer is about 0.4m to 10.7m. The outcrop layer at the portal of right tunnel entrance is mainly Ordovician limestone, and its strike is perpendicular close to the axis of the cave. The portal of right tunnel is dominated by Yanshanian diorite, joint fissure development.

Support parameters and construction plan

The excavation of the III-level surrounding rock mass section of the Laohushan Tunnel used two-step and three-section excavation method. The construction sequence of the field excavation is shown in Figure 2. (1) Excavation of the upper bench → (2) Excavation of the right side of the lower bench → (3) Excavation on the left side of the lower bench.

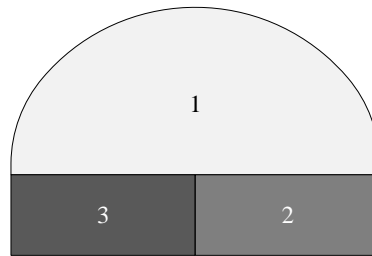


Fig. 2 – Two-step and three-section excavation method

The initial support parameters of the Laohushan Tunnel are shown in Figure 3. The steel frame is made of I18 I-beam, with a longitudinal distance of 120 cm. The steel frame was welded with 20 cm × 20 cm steel mesh and $\Phi 22$ mm anchor rod was placed at the vault, 30°, 60°, and arched which length $L=350$ cm.

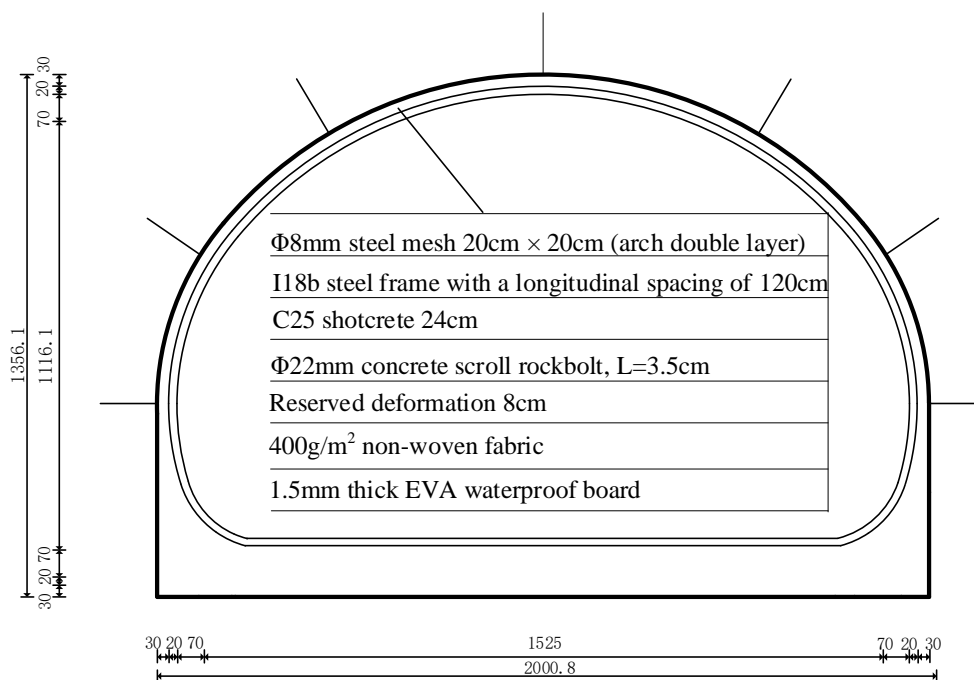


Fig. 3 – Initial support parameters of the Laohushan Tunnel

Monitoring measurement plan

Selection of monitoring and measuring section about III-level surrounding rock mass

The monitoring section of the two-step construction of the Laohushan Tunnel was selected on the right line, and the mileage of the section is YK2+860. The section is far away from the rescue passage of the Laohushan Tunnel, and serves as construction guide hole during the construction period. Avoiding the interference of factors such as the increase of the span at the intersection of the construction guide hole and the main hole. Meanwhile, the construction of the III-level surrounding rock mass section of the left tunnel was postponed to two months after the YK2+860 section is monitored. So the monitoring and measurement of the III-level surrounding rock mass section excavated by two-step and three-section excavation method of right-hole tunnel is carried out, which can provide a reliable reference for the construction of the III-level surrounding rock mass of the left hole later. The surrounding rock condition of III-level surrounding rock section in the tunnel is shown in Figure 4.



Fig. 4 – Monitoring section rock condition

Monitoring measurement point arrangement

According to the requirements of China's "Technical Specifications for Highway Tunnel Construction" (JTJ F60-2009), combined with the structural characteristics and construction methods of the Laohushan super larger span tunnel, the monitoring and measurement projects were developed, which includes deformation monitoring and force monitoring. Among them, the deformation monitoring has arch settlement and clear air convergence, the force monitoring includes surrounding rock mass pressure, shotcrete stress, steel frame stress, etc. And the key parts of tunnel construction are tracked and monitored. In view of the two-step and three-section excavation method used in the tunnel monitoring and measuring section, and the excavation of the right side of the lower bench is delayed for 50 days, which is compared with the upper bench. There is no condition for the deformation monitoring point at the lower bench. The deformation monitoring measurement scheme is determined to arrange five settlement deformation monitoring points and 2'-3', 4'-5' horizontal convergence deformation lines around the arch of upper bench, as shown in Figure 5 The layout of stress monitoring components including surrounding rock mass pressure, steel frame stress, and concrete stress is shown in Figure 4 With the initial support of tunnel face, the stress monitoring components of the corresponding parts of 0~6 in Figure 6 are buried, and the corresponding 7 and 8 parts of Figure 6 are buried respectively after the subsequent step excavation.

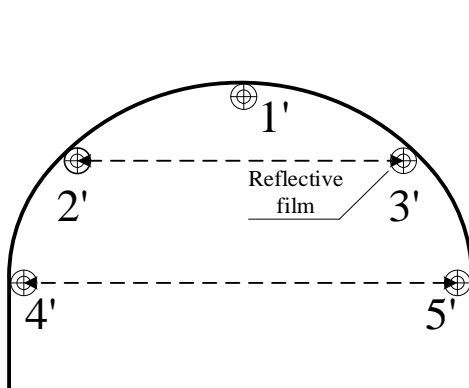


Fig. 5 – Monitoring point layout

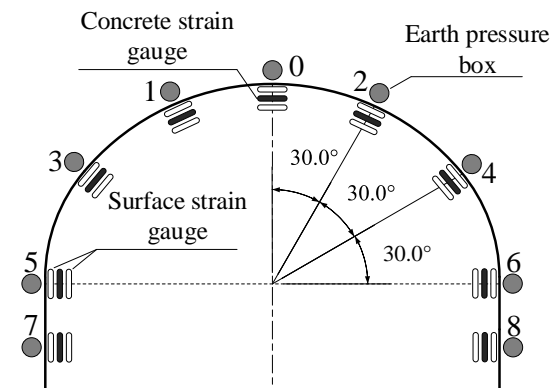


Fig. 6 – Stress monitoring component layout

RESULTS

Deformation monitoring results analysis

Arch settlement

The on-site monitoring and measurement data of YK2+860 section arch settlement is shown in Table 1. The arch settlement curve is shown in Figure 7.

Tab. 1 - Monitoring results of arch settlement in monitoring section

Position	Test section	Maximum settlement value/mm	Cumulative settlement/mm
Vault (1')	YK2+860	8.6	7.2
Left arch waist (2')	YK2+860	2.4	2.3
Right arch waist (3')	YK2+860	4.8	4.5
Left arch (4')	YK2+860	3.2	2.8
Right arch (5')	YK2+860	12.5	10.9

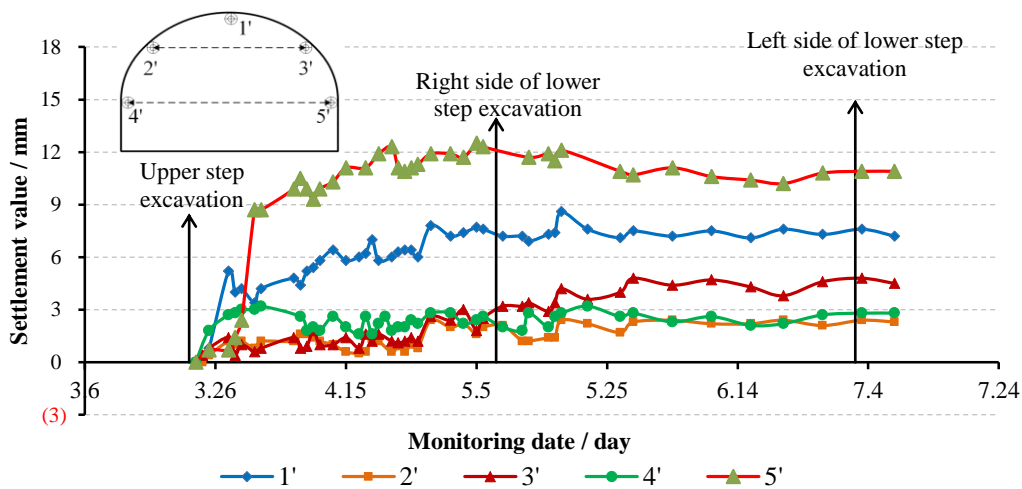


Fig. 7 –Settlement temporal curve on YK2+860 section

It can be seen from Table 1 that the maximum settlement value of the vault of the YK2+860 section is 8.6 mm. The maximum settlement value of the left arch waist is 2.4 mm, the maximum settlement value of the right arch waist is 4.8 mm, and the maximum settlement value of the left wall is 3.2mm, the maximum settlement value of the right wall is 12.5mm. It can be seen that the settlement deformation of the monitoring section in the initial support stage is relatively small.

It can be seen from the sedimentation temporal curve in Figure 7 that the settlement values of 1' point (vault) and 5' point (right wall) are relatively large, and the settlement values after stabilization are about 11mm and 8mm, respectively. The settlement amplitudes of the monitoring points are not much different, and are less than 5 mm. After the excavation of the tunnel face, the sedimentary temporal curve of each monitoring point generally appears as three stages: rapid growth, slow growth and steadiness. Rapid growth stage: the settlement value increases rapidly in the week after the step excavation on the monitoring section. The cumulative settlement at this stage accounts for about 75% of the total settlement. The slow growth stage, 2~5 weeks after the step excavation on the monitoring section, the sedimentation temporal curve slowly rises. Due to

the influence of the excavation of the front face, the settlement curve has a small fluctuation, but the overall trend keeps growing slowly. The stationary phase: the step excavation on the monitoring section is 5 weeks. After that, the subsidence enters the stable phase from the slow growth phase and gradually stabilizes. Affected by factors such as blasting vibration during construction, the sedimentation time curve has slight fluctuations, but the overall stability is stable. The settlement values of each point after stabilization are different, but they are all within 13mm, which is much smaller than the designed deformation of 80mm.

Clearance convergence

The field monitoring and measurement data of YK2+860 section surrounding rock mass convergence are listed in Table 2, and the headroom convergence time curve is shown in Figure 8.

Tab. 2 - Monitoring section convergence deformation monitoring results

Position	Monitoring section	Maximum convergence value / mm	Cumulative convergence value / mm
Arch waist convergence (2-3)	YK2+860	2.8	2.4
Arch foot convergence (4-5)	YK2+860	5.8	3.8

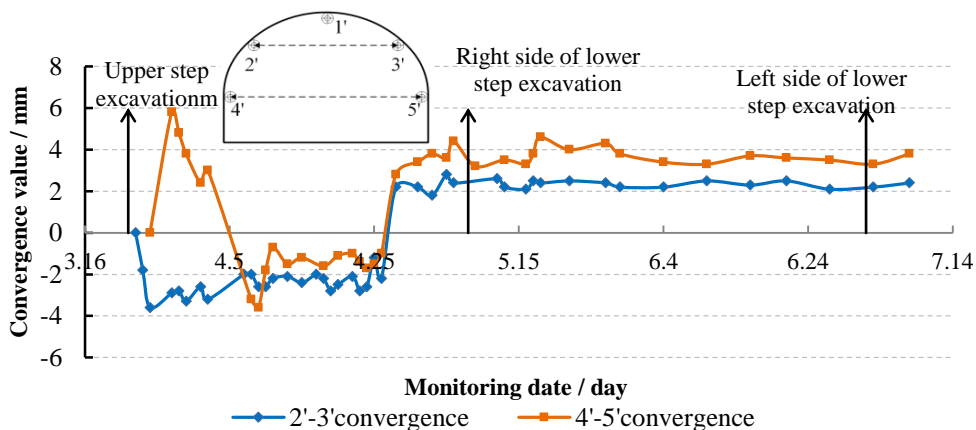


Fig. 8 –Convergence temporal graph on YK2+860 section

It can be seen from Table 2 that the maximum convergence value of the 2'-3' at the waist of the YK2+860 section is 2.8mm, and the maximum convergence value of the 4'-5' at the arch is 5.8mm, and the cumulative convergence values at the arch waist and the arch foot are respectively 2.4mm and 3.8mm.

From Figure 8 of the YK2+860 cross-section headroom convergence, it can be seen that after the excavation of the tunnel face, the convergence around the tunnel shows a negative value, indicating that the initial support and surrounding rock mass occur a certain expansion deformation under the load of the upper part of the surrounding rock mass. The expansion deformation of the arch waist in the horizontal direction is between 2.0 and 3.5 mm, and the expansion deformation of the arch is slightly smaller than that of the arch waist, which is between 0.5 and 2.0 mm. Under the influence of excavation, redistributed surrounding rock mass pressure and so on, the convergence deformation temporal curve has obvious fluctuations at this stage, but the deformation value is small overall. As the tunnelling surface on the right side of the lower bench gradually approaching the monitoring section, due to the influence of its construction disturbance, the headroom convergence occurs in the horizontal direction, and the convergence value suddenly increases

above the abscissa, and the convergence value of the arch waist fluctuates slightly above and below 2.0 mm. The convergence of the arch foot is larger than that of the arch waist, and the convergence value fluctuates slightly above and below 4.0 mm. After the right side of the lower bench has been dug into the monitoring section, the convergence deformation time curve of the arch waist and the arch foot tend to be stable, and the tunnelling construction of the lower bench's left side which is near the monitoring section has no obvious influence on the convergence deformation.

It can be seen that the super larger span highway tunnel is constructed by two-step and three-section excavation method in the class III surrounding rock mass. The maximum settlement of the arch is 12.5mm. The maximum convergence of the clearance is 5.8mm, and the deformation is much smaller than the designed deformation which is 80mm.

Analysis of stress monitoring results

Surrounding rock mass pressure

Monitoring is from March 22, 2017, when the components were buried, to July 18, 2017, when the secondary lining was applied. The maximum surrounding rock mass pressure during this period is listed in Table 3. The variation curve of surrounding rock mass pressure is shown in Figure 7. The numbers in Table 3 and Figure 7 indicate different parts, and the specific parts are shown in the cross section of Figure 9.

Tab. 3 - Distribution of pressure values of surrounding rock mass on YK2+860 section

Measuring point	Maximum pressure value / MPa	Measuring point	Maximum pressure value / MPa
Y0	0.009	Y5	0.009
Y1	0.018	Y6	0.012
Y2	0.052	Y7	0.013
Y3	0.091	Y8	0.007
Y4	0.019		

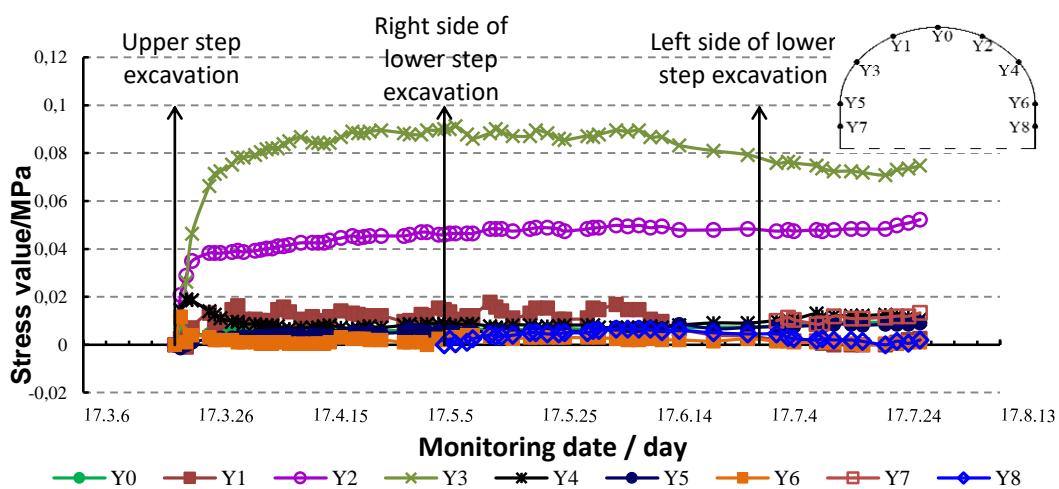


Fig. 9 – Temporal curve of surrounding rock pressure on YK2+860 section

It can be seen from Table 3 that the maximum value of the surrounding rock mass pressure of the YK2+860 section appears at the left arch waist (Y3), the value is 0.091 MPa. And the value of the surrounding rock mass pressure at 30° to the right of vault (Y2), which comes second, is 0.052 MPa. The rest of the surrounding rock mass pressure is relatively small, all less than 0.020MPa, indicating that the surrounding rock mass acts less on the supporting structure.

From the surrounding rock mass pressure temporal curve in Figure 9, it can be seen that except for the right arch waist 30 ° (Y2) and the left arch waist (Y3), the surrounding rock mass pressures of all other points are within 0.020 MPa. The pressure of the surrounding rock mass at the right arch waist 30° (Y2) and the left arch waist (Y3) is relatively large, and it is about 0.05MPa and 0.08MPa respectively after stabilization and the surrounding rock mass exerts less force on the support. The variation trend of the surrounding rock mass pressure temporal curve is similar. The curve increases sharply within 7 days after the excavation of the upper bench, and then quickly stabilizes. The overall trend of the stabilized tense curve is stable and the change is slow. The lower bench excavation process has no significant effect on the surrounding rock mass pressure at upper bench arch.

Steel frame stress

The maximum stress of YK2+860 section steel frame at the initial monitoring points are listed in Table 4 and Table 5. The stress temporal curves of the monitoring section steel frame at inner and outer sides are shown in Figure 10 and Figure 11. In Figure 10 and Figure 11, the letter "B" in B0-1 indicates the steel frame stress, and the numbers indicate different "parts - inner and outer sides" (the outer side indicates the side which the flange plate of steel frame is near the surrounding rock mass "-1", the inner side indicates the side which the flange plate of steel frame is away from the surrounding rock mass "-2"). The positive value indicates that the steel frame stress is compressive stress while the negative value indicates that the steel frame stress is tensile stress.

Tab. 4 - Stress distribution on the outer side of steel frame on YK2+860 section

Measuring point	Maximum stress value / MPa	Measuring point	Maximum stress value / MPa
B0	165	B5	55
B1	120	B6	-48
B2	113	B7	22
B3	-	B8	-24
B4	184		

Tab. 5 - Stress distribution on the inner side of steel frame on YK2+860 section

Measuring point	Maximum stress value / MPa	Measuring point	Maximum stress value / MPa
B0	103	B5	-55
B1	81	B6	-35
B2	283	B7	-11
B3	-2	B8	23
B4	56		

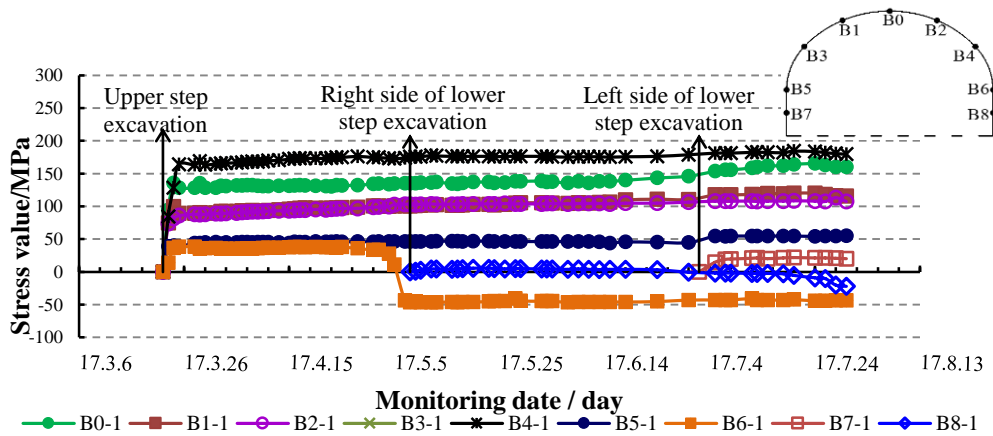


Fig. 10 – Temporal curve of stress on the outer side of steel frame on YK2+860 section

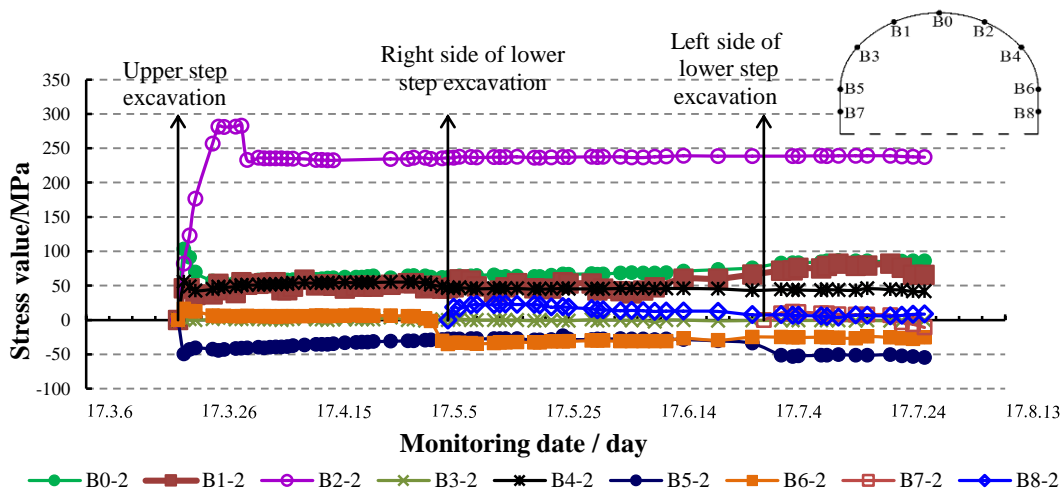


Fig. 11 – Temporal curve of stress on the inner side of steel frame on YK2+860 section

According to Table 4 and Table 5, the stress on the steel frame changes greatly and the load distribution is uneven. From the overall structure, the inner and outer arches (B0, B1, B2, B4) of the steel frame are subjected to large forces, and the compressive stress is the main one. The force at the side wall is small, and the tensile stress is mostly. The steel frame stress, especially the outer edge of the arch, is mainly composed of compressive stress, which indicates that the steel frame effectively played the role of bearing and restricting the deformation of the surrounding rock mass. The maximum stress on the outer side of the steel frame occurs at the arch waist, the value is 184 MPa, and the maximum stress on the inner side of the steel frame occurs at 30° of the right arch waist, the value is 283 MPa, which indicates that the steel frame is subjected to large force and plays the role of bearing and restricting the surrounding rock mass deformation.

From the stress temporal curves of the inner and outer side of the steel frame in Figure 10~11, it can be seen that the stress increases sharply within 1~7 days after the steel frame is applied; the steel frame tends to be stable after 7 days of application, and the stress value of the steel frame changes little with time at this stage. Due to the excavation construction on the right side of the lower bench, the state of the steel frame stress at the right arch (B6) is abrupt. The internal and external compressive stresses of B6 steel frame before May 4, 2017 were 2 MPa and 34 MPa respectively. After the excavated section on the right side of the lower bench approached and exceeded the monitoring section within four days from May 5 to 8, 2017, the internal steel frame stress suddenly changed to tensile stress, and the internal and external tensile stress values

were 35 MPa and 46 MPa, respectively. The time for the abrupt deformation to mutate is more consistent.

Shotcrete stress

The maximum concrete stress of YK2+860 section is shown in Table 6. The stress temporal curve of shotcrete is shown in Figure 10. The parts corresponding to the numbers in Table 7 and Figure 10 are shown in the schematic diagram of the components' position in Figure 12. The positive values in Table 6 and Figure 12 are the compressive stress and the negative value is the tensile stress.

Tab. 6 - Stress distribution of shotcrete on YK2+860 section

Measuring point	Maximum stress value / MPa	Measuring point	Maximum stress value / MPa
0	0.81	5	4.83
1	2.51	6	2.58
2	3.99	7	-0.84
3	1.89	8	-0.71
4	3.80		

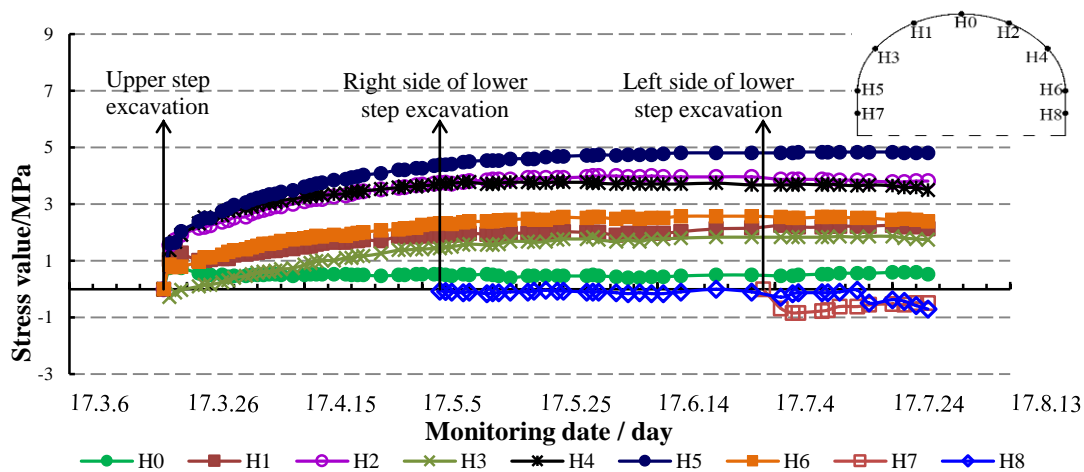


Fig. 12 – Stress temporal curve of shotcrete on YK2+860 section

It can be seen from Table 6 that the concrete of the test section is mainly pressed. The maximum compressive stress of concrete at the monitoring section appears at the left side wall, and its value is 4.83 MPa. The maximum concrete stress is much smaller than 25 MPa, which is the ultimate compressive strength of shotcrete.

It can be seen from Figure 12 that the development trend of the shot concrete stress temporal curve of each monitoring point is basically the same for YK2+860 section. The stress growth is faster within 7 days after the application of the shotcrete, and the stress growth is slow after 7 days of application. After 60 days of application, the stress value is basically in a stable state, and the step construction process has no obvious influence on the concrete stress state.

To sum up, it can be seen that for super larger span highway tunnels constructed using two-step and three-section excavation method for III-level surrounding rock mass, the deformation and the force of support structure are relatively small after the excavation of the upper bench. The supporting structure can well restrain the deformation of the surrounding rock mass and make the surrounding rock mass enter the stable state in a short time. The subsequent lower bench construction will have less influence on the deformation of the tunnel and the support structure.

Safety evaluation of tunnels and supporting structures

According to the monitoring results of the tunnel deformation and supporting structure stress of YK2 + 860 section, the safety of each supporting structure was evaluated. The detailed evaluation contents are listed in Table 7.

Tab. 7 - Safety evaluation of tunnel and supporting structures on YK2 + 860 section

Monitoring project		Position	Maximum value	Design value	Proportion (maximum / design)	
Initial support	Arch settlement (mm)	Right arch foot (5')	12.5	80	16%	
	Clearance convergence (mm)	Arch foot (4-5)	5.8	80	7%	
Surrounding rock pressure		Left arch waist 60° (3)	0.091	/	/	
Shotcrete stress (MPa)	Compressive stress	Left arch foot (5)	4.83	11.9	41%	
	Tensile stress	Left wall foot (7)	-0.84	-1.27	66%	
Steel frame stress (MPa)	Outside	Compressive stress	Right arch waist 60° (4)	184	235	78%
		Tensile stress	Right arch foot (6)	-48	-235	20%
	Inside	Compressive stress	Right arch waist 30° (2)	283	235	120%
		Tensile stress	Left arch foot (5)	-55	-235	23%

It can be known from Table 7 that the maximum value of the initial settlement of the supporting arch in this section is 12.5mm, and the maximum value of headroom convergence is 5.8mm, which is far less than the designed deformation of 80mm. The maximum value of surrounding rock pressure appeared at 60° of the left arch waist, reaching 0.091 MPa. The local compressive stress on the inner side of the steel frame exceeds the yield strength of the steel 235 MPa, but it does not exceed the ultimate compressive strength of the steel 400 MPa, and the tensile and compressive stress values of the other inner and outer parts do not exceed the yield strength (up to 78% of the yield strength). The maximum compressive and tensile stresses of shotcrete are located at the left arch foot and wall foot respectively, and they do not exceed the design tensile and compressive strength of C25 shotcrete.

CONCLUSION

Based on the above monitoring measurement data analysis, the following conclusions can be drawn:

- (1) For super larger span highway tunnels, located in III -level surrounding rock mass, constructed by two-step and three-section excavation method, the maximum arch settlement is 12.5 mm, the maximum clearance is 5.8 mm, and the deformation is much smaller than the designed deformation of 80mm. After digging, the effect of support to control tunnel deformation is better.
- (2) For super larger span highway tunnels, located in III-level surrounding rock mass, constructed by two-step and three-section excavation method, the maximum value of surrounding rock pressure is 0.091 MPa. According to engineering experience, this value is within the normal

range of class III surrounding rock pressure and acts on the support. The force on the protective structure is small.

(3) For super larger span highway tunnels, located in III-level surrounding rock mass, constructed by two-step and three-section excavation method, the inner and outer arches of the steel frame are subject to large stresses and mostly tensile stresses, although the local compressive stress on the inside of the steel frame exceeds the yield strength of the steel 235 MPa but did not exceed the ultimate compressive strength of the steel 400 MPa, and the tensile and compressive stress values of the other inner and outer parts did not exceed the yield strength (up to only 78% of the yield strength), indicating that the steel frame played an important role in the initial support. The shotcrete is mainly compressed, and its maximum compressive and tensile stresses are located at the left arch foot and the wall foot respectively, and both do not exceed the design tensile and compressive strength of the C25 shotcrete.

(4) Based on the comprehensive test results of tunnel deformation and supporting structure stress, it can be seen that after the two-stage and three-section excavation method of the III-stage surrounding rock section of a super-long-span highway tunnel, the initial support effectively controlled the tunnel deformation, and each stress of supporting structures was safety, the tunnel structure is stable.

ACKNOWLEDGEMENTS

The authors would like to acknowledge the financial support provided by the national key research and development program (grant no. 2016yfc0802202), the national natural science fund project of china (grant nos.51108034, 51408054 and 51678063), the china postdoctoral science foundation (grant no.2016m602738), the basic research project of natural science in shaanxi province (grant no. 2017jm5051) and the chang jiang scholars program (grant no. T2014214).

REFERENCES

- [1] Barton N, Lien R, Lunde J, 1974. Engineering classification of rock masses for the design of tunnel support Publikasjon - Norges Geotekniske Institutt
- [2] Bizjak KF, Petkovek B, 2004. Displacement analysis of tunnel support in soft rock around a shallow highway tunnel at Golovec Engineering Geology 75:89-106 doi:10.1016/j.enggeo.2004.05.003
- [3] Chen J-J, Zhou F, Yang J-S, Liu B-C, 2009. Fuzzy analytic hierarchy process for risk evaluation of collapse during construction of mountain tunnel Yantu Lixue/Rock and Soil Mechanics 30:2365-2370
- [4] Choi SO, Chung S-K, 2004. Stability analysis of jointed rock slopes with the barton-bandis constitutive model in udec International Journal of Rock Mechanics and Mining Sciences 41:2B 20 21-26 doi:10.1016/j.ijrmms.2004.03.103
- [5] Fang Q, Su W, Zhang D, Yu F, 2016. Tunnel deformation characteristics based on on-site monitoring data Yanshilixue Yu Gongcheng Xuebao/Chinese Journal of Rock Mechanics and Engineering 35:1884-1897 doi:10.13722/j.cnki.jrme.2014.1663
- [6] Gong J-W, Xia C-C, Zhu H-H, Tang Y, 2009. Optimal analysis of construction schemes for Heshang small-space tunnels with large section Yantu Lixue/Rock and Soil Mechanics 30:236-240
- [7] Gonzalez-Nicieza C, Alvarez-Vigil AE, Menendez-Diaz A, Gonzalez-Palacio C, 2008. Influence of the depth and shape of a tunnel in the application of the convergence-confinement method Tunnelling and Underground Space Technology 23:25-37 doi:10.1016/j.tust.2006.12.001
- [8] Jiang K, Xia C, 2010. Analysis of monitoring and measurement of small clear spacing highway tunnel with eight lanes Yanshilixue Yu Gongcheng Xuebao/Chinese Journal of Rock Mechanics and Engineering 29:3755-3761
- [9] Jiang Y, Yoneda H, Tanabashi Y, 2001. Theoretical estimation of loosening pressure on tunnels in soft rocks Tunnelling and Underground Space Technology 16:99-105 doi:10.1016/S0886-7798(01)00034-7

- [10] Li P, Zhao Y, Zhang D, Wu D, 2013. Study of distribution laws of tunnel surrounding rock pressure based on field measured data statistics *Yanshilixue Yu Gongcheng Xuebao/Chinese Journal of Rock Mechanics and Engineering* 32:1392-1399
- [11] Li S, Yuan C, Feng X, Li S, 2016. Mechanical behaviour of a large-span double-arch tunnel KSCE *Journal of Civil Engineering* 20:2737-2745 doi:10.1007/s12205-016-0456-y
- [12] Liu Y-P, He S-H, Wang D-H, Li D-Y, 2015. Study of surrounding rock pressure calculation of deep super-span underground structures *Yantu Lixue/Rock and Soil Mechanics* 36:118-124 doi:10.16285/j.rsm.2015.S2.015
- [13] Priest SD, 2005. Determination of shear strength and three-dimensional yield strength for the Hoek-Brown criterion *Rock Mechanics and Rock Engineering* 38:299-327 doi:10.1007/s00603-005-0056-5
- [14] Qu H-F, Zhu H-H, Cai Y-C, 2008. Discussion on calculation of loose load on extra-large cross-section and large-span road tunnel *Yantu Lixue/Rock and Soil Mechanics* 29:989-994+1000
- [15] Sharifzadeh M, Kolivand F, Ghorbani M, Yasrobi S, 2013. Design of sequential excavation method for large span urban tunnels in soft ground - Niayesh tunnel *Tunnelling and Underground Space Technology* 35:178-188 doi:10.1016/j.tust.2013.01.002
- [16] Shen B, Barton N, 1997. The disturbed zone around tunnels in jointed rock masses *International journal of rock mechanics and mining sciences & geomechanics abstracts* 34:117-125 doi:10.1016/S0148-9062(96)00048-4
- [17] Singh B, Goel RK, Jethwa JL, Dube AK, 1997. Support pressure assessment in arched underground openings through poor rock masses *Engineering Geology* 48:59-81 doi:10.1016/S0013-7952(97)81914-X
- [18] Wu Q-J, Wang M-N, Liu D-G, 2012. Research on stability of tunnel surrounding rocks based on statistical analysis of on-site displacement monitoring data *Yantu Lixue/Rock and Soil Mechanics* 33:359-364
- [19] Xia C, Gong J, Tang Y, Zhu H, 2007. Study on site monitoring of large-section highway tunnels with small clear spacing *Yanshilixue Yu Gongcheng Xuebao/Chinese Journal of Rock Mechanics and Engineering* 26:44-50
- [20] Zeng S, Qin Q-T, Yang J-S, 2008. In-situ monitoring behaviors of middle wall of large-span multi-arch tunnel *Yantu Lixue/Rock and Soil Mechanics* 29:2537-2541
- [21] Zhang G-H, Chen L-B, Qian S-X, Cai G-Y, Wu C-F, Li Q, 2010. On-site supervision measure and analysis of Damaoshan tunnels with large section and small clear-distance *Yantu Lixue/Rock and Soil Mechanics* 31:489-496
- [22] Zhou D, Cao L, Ma Y, Fang S Stability monitoring and analysis of core rock in a tunnel with extra-large cross section and low flat-ratio during construction. In: 2011 GeoHunan International Conference - Tunnel Management, Emerging Technologies, and Innovation, June 9, 2011 - June 11, 2011, Hunan, China, 2011. Geotechnical Special Publication. American Society of Civil Engineers (ASCE), pp 56-63. doi:10.1061/47632(411)8
- [23] Zhou D, Cao L, Qu H, Yi L, Fang S, 2009. Deformation monitoring and control of super large section highway tunnel with different surrounding rocks *Yanshilixue Yu Gongcheng Xuebao/Chinese Journal of Rock Mechanics and Engineering* 28:2510-2519
- [24] Zhou D, Qu H, Cai Y, Cao L, Yang H, 2009. In-situ test on surrounding rock deformation in super-large section and large-span tunnel *Yanshilixue Yu Gongcheng Xuebao/Chinese Journal of Rock Mechanics and Engineering* 28:1773-1782
- [25] Zhou Z, Li J, Jin B, Liu Y Numerical Investigation of the Optimal Construction Sequence of an Actual Super Shallow Large-Span Tunnel. In: World Multidisciplinary Civil Engineering-Architecture-Urban Planning Symposium 2017, WMCAUS 2017, June 12, 2017 - June 16, 2017, Prague, Czech republic, 2017. IOP Conference Series: Materials Science and Engineering. Institute of Physics Publishing. doi:10.1088/1757-899X/245/2/022003

CHARACTERISATION OF THERMAL-LOADED CEMENT-BASED COMPOSITES BY COMBINED TIME-LAPSE TOMOGRAPHY AND THE FOUR-POINT BENDING TEST

Ivana Kumpová^{1,2}, Tomáš Fíla², Petr Koudelka², Iva Rozsypalová¹, Zbyněk Keršner¹, Daniel Kytýř², Michal Vopálenský², Daniel Vavřík²

1. *Brno University of Technology, Faculty of Civil Engineering, Veverí 331/95, 602 00 Brno, Czech Republic; Ivana.Kumpova@vutbr.cz*
2. *Institute of Theoretical and Applied Mechanics of the Czech Academy of Sciences, Prosecká 809/76, 190 00 Prague 9, Czech Republic*

ABSTRACT

Quasi-brittle materials like cement-based composites, rocks, and bricks are subjected to a number of environmental loadings throughout the life cycle of buildings. For instance, fluctuation of the ambient temperature (climatic cycles or fire) causing a variety of physical and chemical transitions resulting in structural changes and affecting the mechanical properties. In this work a special mixture containing glass spheres and Portland cement was evaluated by a combination of four-point bending and time-lapse X-ray computed tomography to verify the feasibility of this novel combined method.

The effect of temperature on the behavior of investigated material in terms of sphericity of the present glass spheres and the way of crack propagation under load together with its influence to mechanical fracture parameters was studied. The described methodology was used especially to be able to monitor these changes throughout the loading process, as the characterization of the fracture surface using conventional optical methods is possible only after the complete fracture of the specimen and total damage of used material results in loosening of the matrix and filler to such an extent, that the results of these methods may be very distorted. It has been proven that the developed method can be used to characterize the internal structural changes in building materials and thus contribute to the understanding of the fracture processes during mechanical loading. Up to 600°C the glass spheres stay spherical and the crack is propagating through the interfacial transition zone, while at higher temperatures the glass loses its shape and the newly formed pores cause also cracks within the inclusions. The relationship between compressive strength and the maximum loading temperature was confirmed.

KEYWORDS

Fine-grained cement-based composites, Quasi-brittle material, X-Ray computed tomography, Instrumented four-point bending test, Crack path

INTRODUCTION

Cement-based composites belong to very often used building materials [1, 2]. Structures utilizing these composites were commonly designed assuming normal service temperatures. However, high temperatures carrying out on cement-based composites cause a wide range of physical and chemical processes, which result in changes in the micro-structure of composites and thus affect its mechanical properties [3]. According to the fracture mechanics theory, cement-based composites show quasi-brittle response. Specimens made from these materials have the ability to

carry the load even after the deviance from a linear part of force–displacement diagram until the maximum load and then the decrease of the load follows until the final failure [4, 5]. One of the reasons for this response could be the existence of the interfacial transition zone (ITZ). This well-known zone around aggregate particles of a few micrometres in size has specific features. These are mainly higher porosity and calcium hydroxide contents compared to the bulk matrix [6, 7, 8].

Characterization of quasi-brittle materials concerning their resistance to crack formation and its propagation is within the scope of interest for a long time [9]. Various testing methods based on different experimental configurations and sample geometries have been introduced, but intensive research is still devoted to assessing parameters affecting the reliability and reproducibility of the obtained results. For a closer understanding of the parameters influencing the process of crack evolution, a method based on monitoring of parameters around the crack tip (fracture process zone, FPZ) was developed [10, 11]. In addition, other experimental techniques based on acoustic emission, holographic and infrared interferometry, and X-ray imaging are used to investigate FPZ characteristics for analytical models and numerical simulations purposes. Recently, studies have been published [12, 13], which are focused on the investigation of FPZ in silicate composites and rocks using radiographic observation of the specimens loaded by three-point bending, both by simple 2D transmission radiography and advanced time-lapse computed tomography (4D-CT) [14, 15].

These studies demonstrate that computed tomography (CT) can be used complementary to the mechanical tests thanks to the obtained information about the shape of the fracture process zone and the spatial distribution of cracks within the internal structure [16]. Concluding these results, the appropriate 4D-CT setup in conjunction with optimized in-situ loading allows acquiring several CT measurements within softening of the loaded specimen caused by the evolution of the material damaging, while the detailed 3D model of developed FPZ and cracks is obtained. However, the methodology is highly demanding, both in terms of the CT scanner and loading device. Besides the difficulties arising from the interconnection between the three-point bending test and the 4D-CT, main problems arise from the mechanical contact between the tested specimen and supports. High rigidity of the loading device is essential since its deformation can cause a sudden collapse of the investigated specimen.

Another obstacle directly influencing the quality of the tomographic reconstruction and its resolution is a typical arrangement of the standard three-point bending device: the specimen is oriented horizontally on two supports, while the vertical movement of the third support induces loading. The rotation axis in a typical tomograph for industrial use is vertical. Thus, when the loading device is mounted on the rotation platform, the sample is oriented orthogonally to the rotation axis and during the rotation, which is indispensable for CT data recording, there is a significant variation in the thickness the X-ray radiation penetrates (transmission length). Variable transmission length affects the quality of the tomographic reconstruction. In addition, the dimensions of the loading chamber together with the available radiation power and the desired image resolution greatly limit the possible length of the examined specimen. The development of a new four-point bending device has largely eliminated the problems described. A novel device for four-point bending of the specimens is designed in the way that the sample is oriented vertically, i.e., its longitudinal axis is parallel (ideally identical) to the rotation axis. Hence, the loading force is applied in the horizontal direction. The transmission length variation is significantly lower compared to the specimen oriented orthogonally to the rotation axis.

The paper presents the use of such a four-point bending device for obtaining 4D-CT during loading, extracting information at various stage of the load and studying of the intrinsic structure and fracture properties of a specially designed, fine-grained cement-based composite exposed to thermal stress. This material was chosen with respect to minimization of variable parameters for subsequent numerical simulations. X-ray computed tomography provides various information about the material structure, such as the volume fractions and geometry of constituents, and the formation of cracks (in matrix / inclusions / interfacial transition zone) caused by the thermal

loading. On the other hand, the instrumented loading device provides information about the mechanical behavior of the investigated material. A time-lapse series of computed tomography data were recorded during 4-point bending test applied on the notched specimen (stress concentrator) to provide a comparison of differently thermal-loaded material and its behavior during mechanical loading including visualization of the evolution of the spatial structural changes during loading.

Each investigated specimen was subjected to different loading temperature before the flexural test to investigate its influence on the mechanical properties and cracks evolution. Specimens were manufactured from a special mixture containing glass spheres and Portland cement. This material can be taken as a binary material in terms of present phases and their topology. The possibility to accurately geometrically describe the spheres makes it an ideal material for numerical simulations (not subject of this paper) concerning fracture mechanics parameters. Glass spheres with a diameter of 2 ± 0.2 mm were used as a filler, investigated specimens were subjected to temperature loads up to 100, 200, 400, 600 and 1000 °C.

MATERIALS AND METHODS

X-Ray computed tomography

X-rays, when passing through the material, are attenuated, depending on the elemental composition, density and thickness (transmission length) of the specimen. An intensity image is then observed at the detector. X-ray computed tomography (XCT) employs a set of 2D X-ray images (radiograms, projections) of the object exposed from different directions (angles) around the examined object (typically hundreds to thousands). To obtain a 3D virtual model of the irradiated scene, several methods can be used to process the set of projections, one of the classical being the filtered back projection method. The resultant reconstruction gives us a virtual 3D model of the investigated volume providing the true spatial information about its geometry and internal structure. In the standard industrial cone-beam tomography, the object to be examined is fixed on a rotary stage, which rotates around its axis in a step-wise movement, while the X-ray tube and area imaging detector are static and acquire one projection at each rotation step.

Presented X-ray CT results were obtained by an advanced "on-the-fly" tomography method, where the investigated specimen rotates continuously and one rotation follows the other. This approach makes it possible to obtain a sufficient number of projections in a sufficiently short time without the delays that take place in the step-wise scanning due to the positioning of the precise rotary stage and an appropriate exposition triggering. Furthermore, continuous loading of the specimen eliminates relaxation effects present during intermittent loading, when loading is stopped to perform a revolution of the specimen for one tomographical scan. The relaxation not only presents a problem during the evaluation of the experiment but may also be one of the causes for the sudden formation of macro-crack and failure of the specimen even during initial stages of the experiment. The result is a series of time-dependent tomography datasets. When the rotation time is set carefully with regard to the exposition time, the effect of the movement of the object during the exposition does not cause significant difficulties in the reconstruction.

Tomographic measurements were made using a patented multipurpose modular tomographic device TORATOM (Twinned ORthogonal Adjustable TOMograph) at the Institute of Theoretical and Applied Mechanics of the Czech Academy of Sciences (CAS), Centre Telč, employing the novel device for 4-point bending testing, depicted in Figure 1. TORATOM combines two pairs of imaging lines, each consisting of an X-ray tube and an imaging detector, in an orthogonal arrangement with a shared rotary stage, allowing thus an acceleration of the data acquisition process. The device has fully motorized axes for adjusting the system orthogonality in any position and setting the X-ray tube–specimen–detector distances to set the magnification in a range from about 1.2× to 100× (even more in special cases). The device is designed modularly

and allows the quick exchange of various available types of detectors (flat panels, photon-counting detectors). With respect to the used detector type and its native pixel size, it is possible to change the resolution of the CT reconstruction, i.e. the size of one spatial point of the model (voxel), from about 180 μm to less than 1 μm . Very high and stable resolution is achieved also thanks to an anti-vibration table on which the entire assembly is installed and the use of a high-precision tomographic rotary stage. The TORATOM device is unique in the field of industrial CT even on a global scale, as evidenced by the fact that TORATOM is patented at European level (EP 2835631 B1).

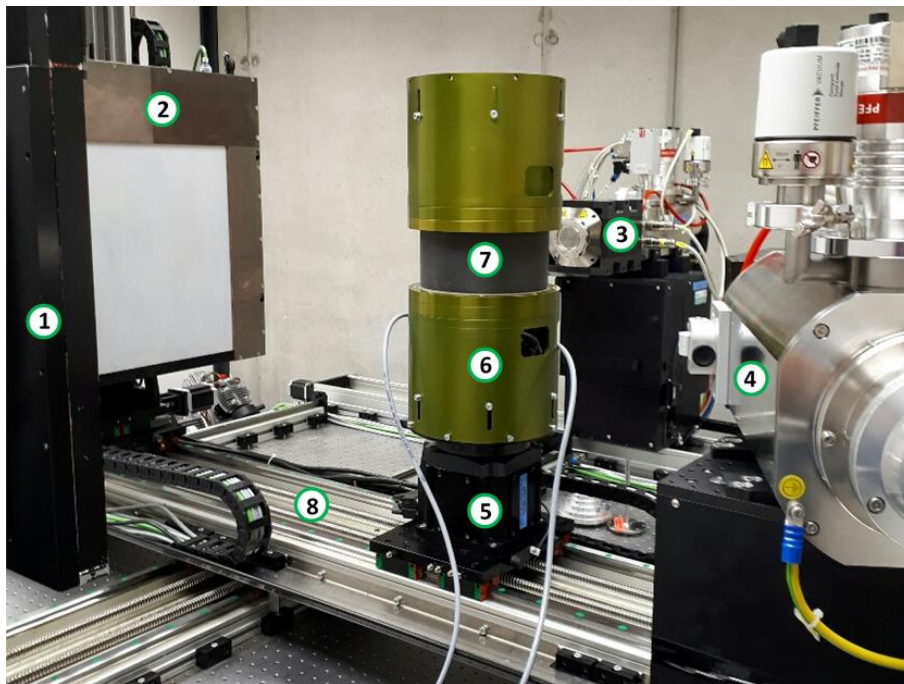


Fig. 1 – TORATOM tomography system employing novel device for 4-point flexural testing: 1) Detector holder, 2) Large area flat panel detector, 3) Nano-focus transmission type X-ray tube, 4) Micro-focus reflective type X-ray tube, 5) High-precision tomographic rotary stage, 6) Device for 4-point flexural testing during CT, 7) Loading chamber accommodating the specimen, 8) Active damped anti-vibration table with high-precision CNC positioning system

Novel device for 4-point flexural testing during 4D computed tomography

Modular device for 4-point flexural testing during 4D computed tomography recently developed at the Institute of Theoretical and Applied Mechanics of the CAS consists of three main components: a pair of motorized loading units with integrated external supports of the four-point bending configuration, a pair of static inner supports of the four-point bending configuration, and a cylindrical supporting frame. During the test, the internal supports are in a fixed position, while the outer movable supports attached to the closed-loop high-precision positioning system perform the loading. The synchronized driving units are equipped with linear encoders and load-cells for measuring the force on both external supports. The frame of the loading chamber accommodating the specimen is made of a 1.95 mm thick carbon-fiber composite that has sufficient stiffness and low X-ray attenuation. Simplified scheme of the device solution in partial section and its orientation in tomographic assembly is shown in Figure 2.

Such design brings advantages against the standard horizontal orientation of the three-point bending arrangement. The specimen length can be extended without the need for increasing the diameter of the loading device, which would necessarily result in a lower achievable resolution

of the obtained radiograms. As a result, it is possible to investigate a wide range of materials, because specimens having representative volume elements can be used. Furthermore, during rotation of a vertically oriented sample, low variability of the X-ray attenuation is achieved leading to an increase in quality of reconstruction. The relative position of internal and external supports can be adjusted independently, which allows the selection of the optimal setup geometry depending on the specimen characteristics (i.e. overall dimensions, the shape of the cross-section, notch geometry, etc.) and material. Input and output wiring is equipped with a pair of slip rings that enable an unlimited number of revolutions of the whole device on the rotational stage of the tomographic scanner. The maximum loading capacity of the device is 1500 N per support, position accuracy and repeatability is better than 10 μm with a minimum increment lower than 1 μm . The device is closed-loop controlled by the proprietary Linux CNC software running on the real-time kernel [16]. As shown in Figure 1 and Figure 2, during the tomographically observed loading, the longitudinal axis of the investigated sample is parallel (nearly identical) to the axis of rotation of the device and the rotational stage.

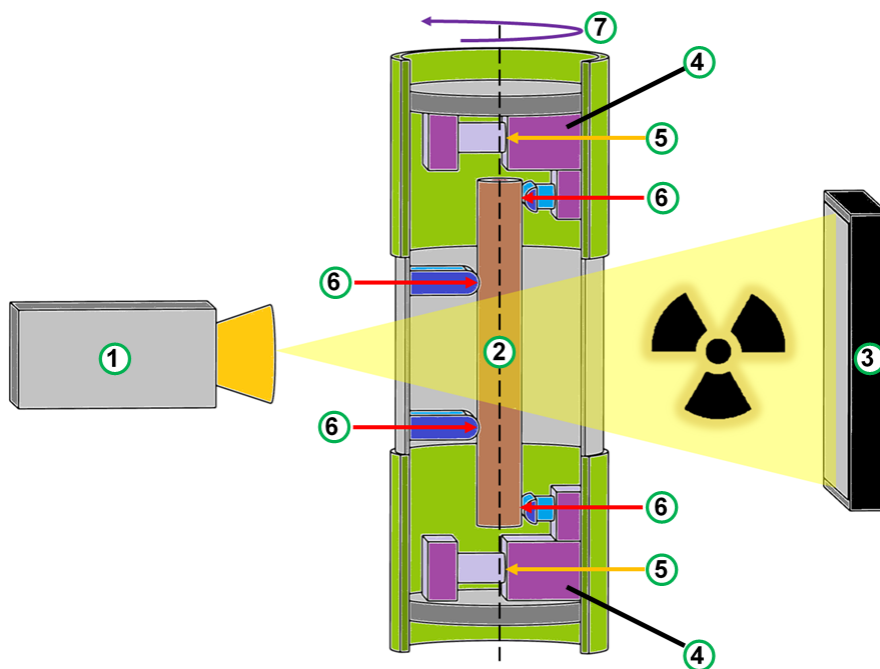


Fig. 2 – Novel device for 4-point flexural testing during 4D computed tomography: 1) X-ray tube, 2) Specimen with the highlighted field of view, 3) Imaging detector, 4) Precise linear drive, 5) Outer supports displacement, 6) Applied force, 7) Rotation of the device during CT

Test specimens and procedure

In total 6 sets, each of 4 test specimens with dimensions of 20 mm \times 40 mm \times 200 mm were prepared from a specially designed, fine-grained cement-based composite. The fresh mixture was made using sodium-potassium glass spheres with a diameter of 2 ± 0.2 mm, Portland cement CEM I 42.5 R (cement factory Mokra, Czech Republic) and water at the weight ratio of 3:1:0.35. After pouring into the prepared silicone molds and compacting, the specimens were left covered with PE foil for one day and then kept in water for 28 days.

Mature samples were dried at the temperature of 100 $^{\circ}\text{C}$ and further kept in ambient temperature and constant humidity in a desiccator. One set of specimens was kept as reference samples (100 $^{\circ}\text{C}$), while the rest sets were exposed to the pre-set temperatures of 200 $^{\circ}\text{C}$, 400 $^{\circ}\text{C}$, 600 $^{\circ}\text{C}$, 800 $^{\circ}\text{C}$, and 1000 $^{\circ}\text{C}$. The range was chosen to capture the process of thermal

degradation with respect to the maximum temperature load provided by the furnace used. For each set, the thermal loading began at 20 °C with an increment of 5 °C / min until the pre-set maximum was reached, which was then maintained for an additional 60 minutes. Temperature loading was delivered using laboratory furnace Clasic 5013 with heating coils on 3 sides. After the specimens were left to cool down to room temperature, they were equipped with an initial notch as a stress concentrator and kept at a constant temperature of 20 °C.

From each set, one specimen was investigated using the X-ray CT with the procedure and results covered in this paper. Other three specimens of each set were used for another investigation [17], which is not described in this paper; however, their compressive strength was measured and used. First X-ray scanning was performed on one specimen from each set after drying and before the temperature load, giving thus 6 CTs. Second X-ray scanning was obtained on each investigated sample after the temperature load, giving thus 6 CTs (even the reference (100 °C) was measured again to observe the potential microstructure changes caused by maturing). The details of the scanning procedure can be found below. The samples subjected to temperatures higher than 200 °C were thermally damaged to the extent that the intended four-point bending experiments were not possible. Thus, only the reference (100 °C) and 200 °C specimens could be subjected to the in situ 4-point bending test in the course of the time-lapse CT, giving thus two sets of 4D CTs. The procedure is in detail described below.

X-ray CT scanning procedure before and after temperature loading

For a qualitative assessment of the damage at the microstructural level of the investigated material caused by the high-temperature loading, standard X-ray tomography measurements were performed with the intact and thermally loaded specimens, i.e. for each specimen a CT was performed before and after the thermal loading procedure. A microfocus X-ray tube (XWT-TCHR-240, X-ray WorX, Germany) operating at 160 kV and the target power of 45 W was used together with the flat panel detector (Dexela 1512NDT, Perkin Elmer, USA) with the active area size of 145.4 × 114.9 mm, a pixel matrix of 1944 × 1536 and a native resolution of 74.8 μm per pixel. The geometry parameters of the tomographic assembly were set to obtain the best possible resolution with respect to the field-of-interest size and the detector area. The *X-ray tube – imaging detector* distance was set to 600 mm and the *X-ray tube – specimen* distance was set to 200 mm providing the geometrical magnification of 3×, which leads to the edge length of the spatial point (voxel) of approx. 25 μm in the resulting 3D reconstruction.

4D CT during the four-point bending measurement

Selected specimens were subjected to four-point bending as a displacement-driven experiment. The distance between the outer supports of the loading device was set to 178.8 mm, the inner supports distance was set to 75 mm. Before the testing procedure, the specimens were pre-loaded by 3 N initial force and the proper geometrical position was checked radiographically. The tests were performed with 0.25 μm/s loading rate up to a displacement value of 1000 μm and 1500 μm in the 100 °C and 200 °C sample, respectively. This loading rate allows on-the-fly imaging mode of the experiment. The ultimate forces of approximately 30 N and 15 N were obtained for 100 °C and 200 °C samples, respectively. Force and displacement data were recorded at the sampling rate of 100 Hz.

For imaging, the same detector and X-ray tube as in the previous case were used. However, the X-ray tube was operated at the accelerating voltage of 180 kV and the target power of 40 W. The geometrical parameters of the tomographic assembly were set to obtain the best possible resolution. The *X-ray tube – imaging detector* distance was set to 480 mm and the *X-ray tube – specimen* distance was set to 200 mm providing the geometrical magnification of 2.4× which leads to the edge length of the spatial point (voxel) of approx. 31.25 μm in the resulting 3D

reconstruction. During the loading under continuous rotation of the loading device on the rotary stage, 17 tomographic datasets of 600 projections were taken. The acquisition time for each projection was 400 ms, giving the time of one rotation 240 s.

Compressive strength value measurement

The remaining parts of the specimens subjected to four-point bending were used for measurement of the compressive strength values. An auxiliary loading mechanism equipped with two square steel plates (top, bottom) was installed in a hydraulic test machine. The specimens were placed between the plates so that the load was applied perpendicularly to the direction of compaction. The specimens were loaded continuously until the failure. The test was carried out in accordance with the principles of standards ČSN EN 196-1 [18] and BS 1881: Part 119 [19]. The compressive strength value was calculated taking the nominal cross-section area of $40 \times 20 \text{ mm}^2$. See selected photo in Figure 3 for illustration.



Fig. 3 – The compression test of specimens: The auxiliary loading device with two auxiliary platens was placed in the hydraulic testing machine with selected specimens prepared for the test

RESULTS

One of the important results is the evidence of the microstructural changes observed with the CT and its correlation with the compressive strength in the temperature loaded samples. X-ray CT proved to be a suitable qualitative tool for this kind of investigations. Some particular samples were placed into the 4-point bending device after the temperature loading and successive CT scans were performed during the loading (4D-CT). The procedure allowed to control and monitor force and displacement over time, giving the possibility of a direct match of the microstructure observed in the individual reconstructed 3D models with the corresponding loading parameters.

From the results of tomographic measurements of specimens before and after the thermal loading, the development of damage caused by the effects of high temperatures is apparent. While the specimen remains compact at $100 \text{ }^\circ\text{C}$ and $200 \text{ }^\circ\text{C}$, heating at $400 \text{ }^\circ\text{C}$ and $600 \text{ }^\circ\text{C}$ already causes the creation of cracks particularly within the interfacial transition zone (ITZ). Upon heating to higher temperatures, the shape of the glass spheres changes and the constituent cohesion deteriorates as the pore size increases and formation of the system of macrocracks causes their interconnection. Examples of the development of damage are shown in Figure 4.

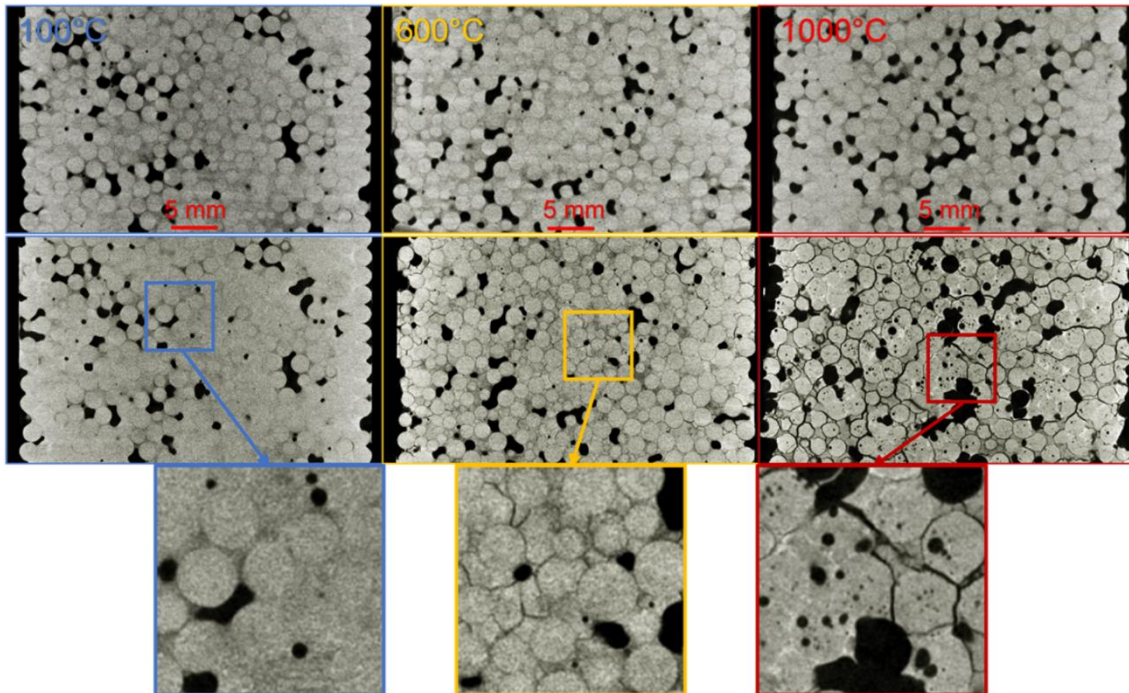


Fig. 4 – Example of visualization of the selected tomographic section for specimens before and after the thermal loading. In the upper part – the selected tomographic sections for specimens in the initial state, in the middle part – identical tomographic sections for specimens after the thermal loading, in the lower part – zoom to microstructure demonstrating progressive damage

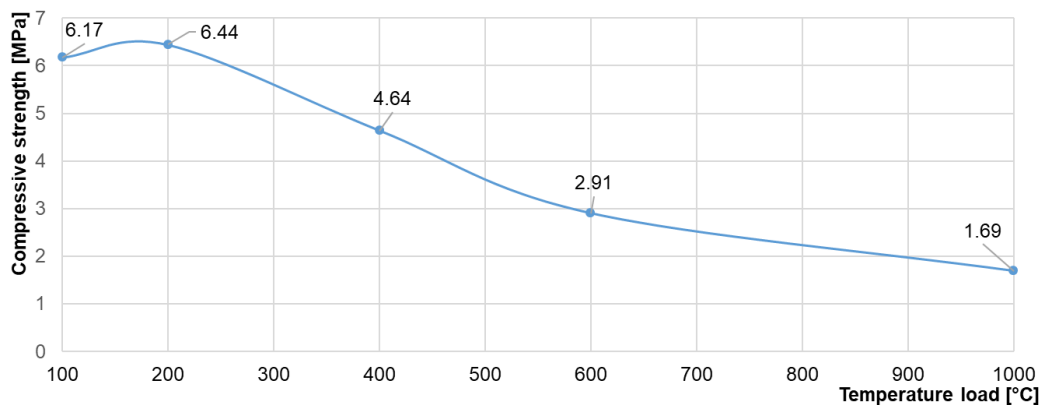


Fig. 5 – The maximum temperature dependence of the mean compressive strength values

Damage observed during tomographic imaging corresponds to the measured compressive strength values shown in Figure 5. The graph depicts the average values of the observed compressive strength measured on all the four manufactured samples in each set (for each temperature), i.e., even for the samples that were not exposed to the CT investigation.

Left part of Figure 6 shows the time dependence of loading force measured during the in-situ four-point bending experiments, while the right part of Figure 6 depicts the force-to-displacement curves. The thin lines in both subfigures show forces measured at individual movable support units. The average values of force are then plotted as the bold lines. The red bold curve shows the average force for the specimen loaded with 100 °C, the green bold curve gives the average force for the specimen loaded with 200 °C. The graph shows, that the resistance of the material to the damaging is decreasing with the temperature increase. The intervals depicted by

blue arrows in the force-time graph define the duration of individual tomographic scans during the loading. From each such tomographic scan, virtual 3D model of the examined specimen was obtained.

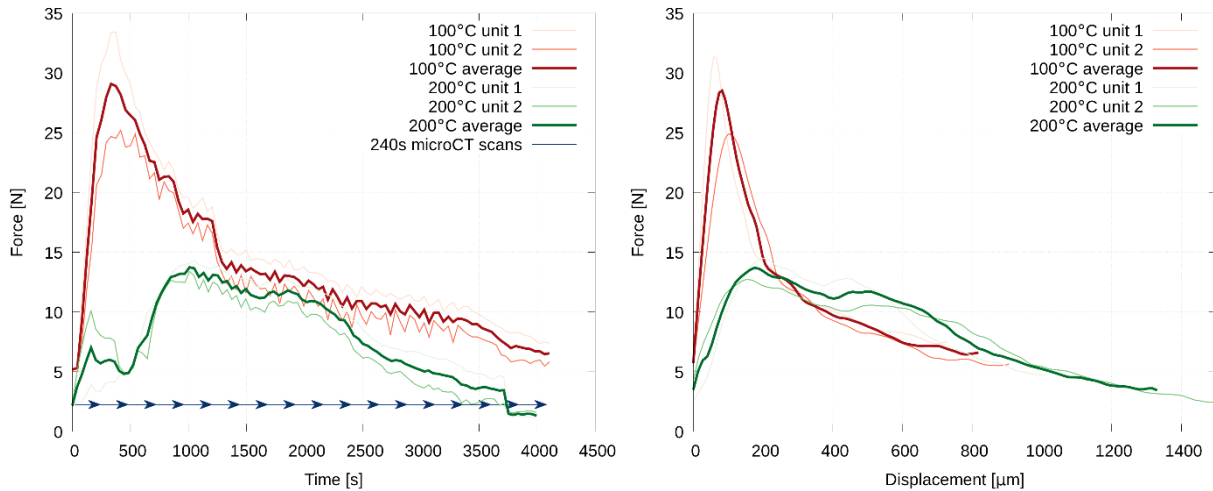


Fig. 6 – Time dependence of the loading forces magnitude obtained by 4-point flexural testing (left), and force-displacement diagram (right)

Based on the resulting 3D images, it is possible to investigate and measure the crack length and opening in individual states within the achieved resolution by the employment of advanced image processing methods including digital image correlation and digital volume correlation. A representative example of the visualization of crack development in 2D (one CT slice) at the beginning of the loading procedure, in the half of the loading procedure and at its end is shown in Figure 7.

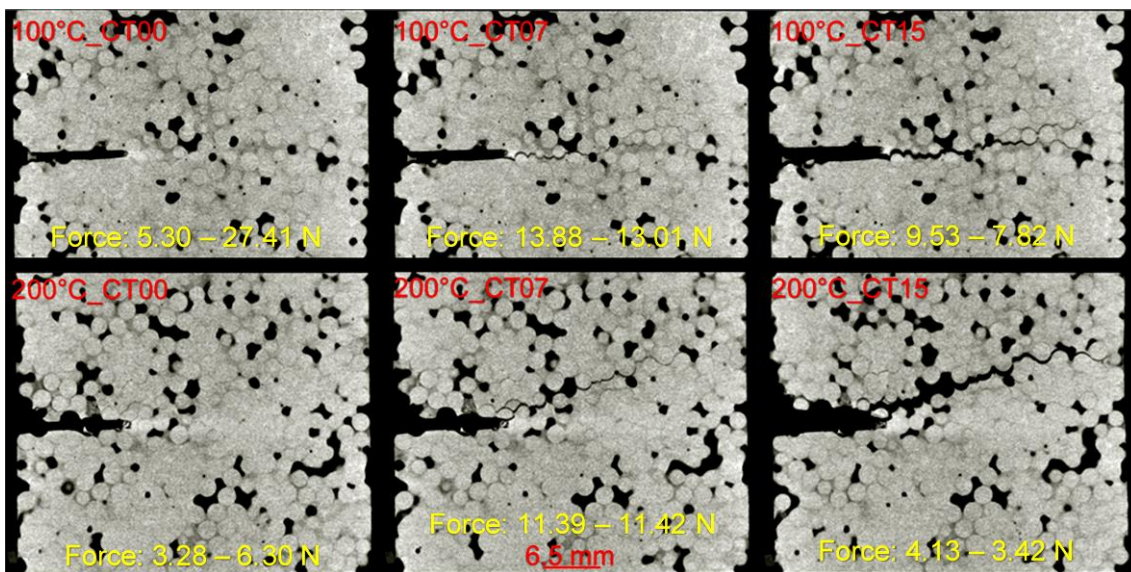


Fig. 7 – Example of visualization of the selected tomographic section showing crack initiation and propagation during loading. In the upper part – the specimen loaded with 100 °C, in the lower part – the specimen loaded with 200 °C

CONCLUSION

The effect of temperature load on the behavior of investigated material in terms of structural changes and the way of crack propagation under load together with its influence to mechanical fracture parameters was studied using a novel method combining four-point bending and time-lapse X-ray computed tomography. It has been proven that the developed method can be used to characterize the internal structural changes in building materials and thus contribute to the understanding of the fracture processes during mechanical loading. The time-dependent alteration in the values of the mechanical parameters together with 3D spatial image information characterizing the damage to the internal structure of the specimens loaded at 100 °C and 200 °C was observed, indicating a decrease in the resistance of the material to the damaging due to exposition to high temperatures.

For specimens loaded with maximum temperatures from 100 °C to 1000 °C, image information provided by standard X-ray computed tomography was evaluated before and after the thermal loading, showing that increasing the temperature leads to formation of cracks within the interfacial transition zone even without action of force. Up to 600°C the glass spheres stay spherical and the crack is propagating through the interfacial transition zone, while at higher temperatures the glass loses its shape and the newly formed pores cause also cracks within the inclusions. The relationship between compressive strength and the maximum loading temperature was confirmed.

ACKNOWLEDGEMENTS

The research was carried out within the framework of the project of the specific university research of the Brno University of Technology No. FAST-J-20-6506 and thanks to the financial support of the Operational Program Research, Development and Education of the Ministry of Education, Youth and Sports within the project No. CZ.02.1.01 / 0.0 / 0.0 / 16_019 / 0000766 (Engineering Applications of Microworld Physics - INAFYM).

Authors express their thanks to Dr. Hana Šimonová, Dr. Patrik Bayer, Ing. Michal Vyhřídál, Ing. Tomáš Majda, and Mr. Miroslav Friedl, Brno University of Technology, Faculty of Civil Engineering, for the support during the preparation of the specimens and prof. Miloš Drdác, Institute of Theoretical and Applied Mechanics of the Czech Academy of Sciences, for valuable comments during loading device development.

REFERENCES

- [1] P. C. Aitcin, S. Mindess, 2011. Sustainability of concrete (Spon Press, New York) 328 pp. ISBN 978-0415571968.
- [2] A. M. Neville, 2011. Properties of Concrete (Pearson Education Limited, Harlow) 872 pp. ISBN 978-0273755807.
- [3] I. Hager, 2013. Behaviour of cement concrete at high temperature. Bulletin of the Polish Academy of Sciences Technical Sciences, vol 61(1), pp. 145-154. DOI: 10.2478/bpasts-2013-0013. ISSN: 2300-1917.
- [4] Karihaloo B. L., 1995. Fracture mechanics and structural concrete (Harlow, United Kingdom: Longman) 346 pp. ISBN 978-0582215825.
- [5] S. Kumar, S. V. Barrai, 2011. Concrete Fracture Models and Applications (Springer, Berlin) 406 pp. ISBN 978-3-642-16764-5.
- [6] RILEM. State-of-the-art Report: TC 108-ICC, J. C. Maso, ed. Interfacial Transition Zone in Concrete. E & FN Spon, London, 1996.
- [7] K. L. Scrivener, A. K. Crumbie, P. Laugesen, 2014. The Interfacial Transition Zone (ITZ) between Cement Paste and Aggregate in Concrete. Interface Science, vol 12, pp. 411-421. DOI: 10.1023/B:INTS.0000042339.92990.4c. ISSN: 09277056

- [8] G. Prokopski, J. Halbiniak, 2004. Interfacial transition zone in cementitious materials. *Cement and Concrete Research*, vol 30(4), pp. 579-583. DOI: 10.1016/S0008-8846(00)00210-6. ISSN: 0008-8846.
- [9] Vesely V., Frantik P., Kersner Z., 2009. Cracked Volume Specified Work of Fracture. In: *Proceedings of the Twelfth International Conference on Civil, Structural and Environmental Engineering Computing*, edited by B. H. V. Topping, L. F. Costa & R. C. Barros (Stirlingshire: Civil-Comp Press), 194. DOI: 10.4203/ccp.91.194. ISBN 978-1-905088-32-4.
- [10] Vesely V., Pail T., Frantik P., Seitl S., 2011. Fracture process zone extent and energy dissipation in silicate composites with different cohesive behaviour. In: *2nd International RILEM Conference on Strain Hardening Cementitious Composites (SHCC2-Rio)*, edited by R. D. Toledo Filho, F. A. Silva, E. A. B. Koenders & E. M. R. Fairbairn (Sarl: RILEM Publications), 259-267. ISBN 978-2-35158-120-9.
- [11] Kumpova I., Fila T., Vavrik D., Kersner Z., 2015. X-ray dynamic observation of the evolution of the fracture process zone in a quasi-brittle specimen. *Journal of Instrumentation*, vol 10(08): C08004 (IOP Publishing Ltd and Sissa Medialab srl). DOI: 10.1088/1748-0221/10/08/C08004. ISSN 1748-0221.
- [12] Kumpova I., Vopalensky M., Fila T., Kytir D., Vavrik D., Pichotka M., Jakubek J., Kersner Z., Klon J. Seitl S., Sobek J., 2018. On-the-Fly Fast X-Ray Tomography Using a CdTe Pixelated Detector – Application in Mechanical Testing. *IEEE Transactions on Nuclear Science*, vol. 65(12): 2870-2876. DOI: 10.1109/TNS.2018.2873830. ISSN 0018-9499.
- [13] Jailin C., Bouterf A. Poncelet M. Roux S, 2017. In situ μ CT-scan Mechanical Tests: Fast 4D Mechanical Identification. *Experimental Mechanics*, vol. 57(8), pp. 1327-1340. DOI: 10.1007/s11340-017-0305-z. ISSN 0014-4851.
- [14] Ogelgesang M., Farago T., Morgeneyer T. F., Helfen L., Dos Santos Rolo T., Myagotin A., Baumbach T., 2016. Real time image-content-based beamline control for smart 4D X-ray imaging: Fast 4D Mechanical Identification. *Journal of Synchrotron Radiation*, vol. 23(5), pp. 1254-1263. DOI: 10.1107/S1600577516010195. ISSN 1600-5775.
- [15] Vicente M.A., Minguez J., Gonzalez D.C., 2019. Computed tomography scanning of the internal microstructure, crack mechanisms, and structural behavior of fiber-reinforced concrete under static and cyclic bending tests. *International Journal of Fatigue*, vol. 121: 9-19. DOI: 10.1016/j.ijfatigue.2018.11.023.
- [16] Rada V., Fila T., Zlamal P., Kytir D., Koudelka P., 2018. Multi-channel control system for in-situ laboratory loading devices, *Acta Polytechnica CTU Proceedings*, vol. 18: 15-19. DOI: 10.14311/APP.2018.18.0015.
- [17] Rozsypalová I., Vyhliđal M., Dvořák R., Majda T., Topolář L., Pazdera L., Šimonová H., Keršner Z., 2018. Characterization of cement-based composite exposed to high temperatures via ultrasonic pulse method. In: *Acta Polytechnica CTU Proceedings*, vol. 15: 99-103. DOI: 10.14311/APP.2018.15.0099.
- [18] ČSN EN 196-1: 2016 Methods of testing cement – Part 1: Determination of strength.
- [19] BS 1881: Part 119: 1983 Testing concrete – Part 119 Method for determination of compressive strength using portions of beams broken in flexure (equivalent cube method).